

https://dspace.org/

Vortices and heat transfer

Makan, Pravin

2022
https://hdl.handle.net/10539/34416

Downloaded from a DSpace repository. https://dspace.org/



UNIVERSITY OF THE
WITWATERSRAND,
JOHANNESBURG

Vortices and Heat Transfer

Student Name: Pravin Makan

(Student Number: 328848)

School of Mechanical, Industrial, and Aeronautical Engineering

University of the Witwatersrand

Johannesburg, South Africa.

Supervisor: Prof. C. Law

A research dissertation submitted to the Faculty of Engineering and the Built Environment, University of the Witwatersrand, in fulfilment of the requirements for the degree of Master of Science in Engineering in Aeronautical Engineering.

Date: 30 May 2022

Declaration

SCHOOL OF MECHANICAL, INDUSTRIAL & AERONAUTICAL ENGINEERING

PLAGIARISM DECLARATION TO BE SIGNED BY ALL HIGHER DEGREE STUDENTS

SENATE PLAGIARISM POLICY: APPENDIX ONE

I Pravin Makan (Student number: 328848) am a student registered for the degree of MSc Engineering in the academic year 2021/22.

I hereby declare the following:

- I am aware that plagiarism (the use of someone else's work without their permission and/or without acknowledging the original source) is wrong.
- I confirm that the work submitted for assessment for the above degree is my own unaided work except where I have explicitly indicated otherwise.
- I have followed the required conventions in referencing the thoughts and ideas of others.
- I understand that the University of the Witwatersrand may take disciplinary action against me if there is a belief that this is not my own unaided work or that I have failed to acknowledge the source of the ideas or words in my writing.

Signature: _____ Date: 30 May 2022

Acknowledgements

This project would not be a possibility without the help from the following people:

Professor Craig Law for his supervision and guidance through the theory and previous work done on vortices and heat transfer.

Maarten Coetzee for providing remote access to the Wits Mechanical, Industrial, and Aeronautical PC Pool.

Dr. Randal Paton and Shunmunga Pilay for providing me access to the CAMS sever, although not used in the project, it was deeply appreciated.

Dr. Burnadette Sunjka, Tebogo Rakhudu, and the administrative staff of the Faculty and School of Mechanical, Industrial, and Aeronautical for their help and administrative assistance for the project.

Lastly I would like to thank my family for being supportive through this journey.

Abstract

The use of vortex methods for heat transfer has picked up considerable attention since the 1970's. Vortices have the ability to enhance heat transfer through bulk fluid mixing. Most of the research on this topic focuses on the heat transfer enhancements the vortices facilitate on heated surfaces. What was not known was the direct influences of fluid properties, of the vortices, on the heat transfer. This research project aims to understand the fluid mechanisms that aid heat transfer in a rectangular flow channel consisting of a single delta winglet vortex generator and a heated bottom surface. The research was done using numerical methods to attain results for vorticity, circulation, shear stress, helicity, and heat transfer. The computational results were validated with past experimental research and was found to be in good agreement. The results showed the formation of two counter-rotating vortices. The main vortex was generated by the vortex generator, while the induced vortex formed because of the motion of the main vortex. Velocity contour plots showed how the boundary layer was augmented by the vortices, and it was found that the downwash of the main vortex contributes most of the heat transfer, while the upwash from the induced vortex lowers heat transfer. Further inspection of Stanton number plots confirmed this. Regions of high shear stress was found under the main vortex, while lower shear stress emanated from the induced vortex. This confirmed that the vortices applied a shear stress on the boundary layer causing energy transfer to the heated surface. It was found that the circulation has an influence on the heat transfer by observing the trends of the plots for circulation and heat transfer. The results for helicity showed that there was energy transfer from the downwash of the main vortex to the heated surface. The +/- sign of the helicity indicated the direction that the main vortex tube was directed in the freestream direction while the induced vortex tube was direct in the opposite. This caused the induced vortex the lower the shear stress on the wall as it was resistant to the freestream flow. Overall, it was concluded that; (a) the circulation of the vortex has the most influence on heat transfer, (b) shear stress is the mechanism for which energy is transferred, (c) helicity gives a good indication of the vortex boundary layer mixing and hence convective heat transfer.

Table of Contents

Declaration i

Acknowledgements ii

Abstract iii

List of Figures vii

List of Tables ix

1. Introduction 1

1.1 Background 1

1.2 Problem Statement 2

1.3 Research Question 2

1.4. Objectives 3

1.5 Structure of Report 3

2. Literature Review 4

2.1 Vorticity and Heat Transfer 4

2.2 Shear Stress, Vortices, and Heat Transfer 7

2.3 Validation Data 8

2.4 Computational Fluid Dynamics 10

2.4.1 Viscous Models 10

2.5 Summary 12

3. Methodology 14

3.1 Domain Model and Meshing 14

3.2 Selection of Turbulence Model 18

3.3 Assumptions, Fluid Parameters, and Boundary Conditions 18

3.3.1 Assumptions 18

3.3.2 Fluid Parameters 19

3.3.3 Boundary Conditions 19

3.4 Wall Treatment 20
3.5 Computational Solution 20
3.6 Data Processing 20
3.6.1 Vorticity 21
3.6.2 Circulation and Vorticity Flux 21
3.6.3 Helicity Density and Helicity Flux 22
3.6.4 Nusselt Number 22
3.6.5 Stanton Number 22
3.6.6 Wall Shear Stress 23
4. Turbulence Model Selection, Mesh Independence, Validation, and Verification 24
4.1 Mesh Independence 24
4.2 Turbulence Model Selection 28
4.3. Validation 29
4.4 Verification 32
4.5 Concluding Remark 32
5. Results and Discussion 34
5.1 Observations 34
5.1.1 Velocity and Vorticity 34
5.1.2 Wall Temperature and Vortex Evolution 37
5.1.3 Heat Transfer: Stanton Number and Nusselt Number 38
5.1.4 Boundary Layer of Flow Past Vortex Generator 40
5.1.5 Wall Shear Stress 41
5.1.6 Summary 45
5.2 Vorticity Flux, Circulation and Heat Transfer 46
5.3 Helicity and Heat Transfer 48
6. Conclusion 53
7. Recommendations 54
References 55

Appendix A1 I
A1.1 Choosing the Right Turbulence Model I
Appendix A2 IV
A2.1 Imaging of Domain IV
A2.2 Imaging of Mesh V
Appendix A3 XI

List of Figures

Figure 1. Longitudinal Vorticity Flux vs Normalized Nusselt Number [12] 4

Figure 2. Schematic of Section Modelled by Song and Wang [6] 5

Figure 3. Streamwise Nusselt Number and Absolute Average Vorticity Flux Variations in the Flow Channel [6] 5

Figure 4. Linear Representation of Nu and J_{abs} with varying Re [6] 6

Figure 5. Wu et al. [10] Velocity Vector Profile of the Flow 7

Figure 6. Velocity Profile for Inflow, Outflow, and Flat Plate Case from Wu et al. [10]. 7

Figure 7. Layout of Experimental Model [8] 9

Figure 8. Velocity and Vorticity Results[8] 9

Figure 9. Spanwise Stanton Number at 0.45m < x < 1.35m [8] 10

Figure 10. Schematic of Domain/Flow Channel 15

Figure 11. Schematic of Vortex Generator 15

Figure 12. Sectioning of Bottom Surface for Meshes A,C, and D (bottom) and Mesh B (top) 17

Figure 13. Spanwise Stanton Number at x = 0.98m 27

Figure 14. Spanwise Stanton Number at x = 1.88 m 28

Figure 15. Comparison of Experimental and Computational Mesh B Circulation 31

Figure 16. Velocity Profile for Mesh A to D 32

Figure 17. Velocity Vector at x = 1.2m 34

Figure 18. Streamwise Velocity Contour Plot at x = 1.2m 35

Figure 19. Contour Plot of the Nondimensional Vorticity at x = 1.2m 35

Figure 20. Streamwise Core Nondimensional Vorticity 36

Figure 21. Streamwise Vorticity Contour and Temperature Distribution Along Flow Channel 37

Figure 22. Spanwise Normalised Stanton Number 38

Figure 23. Contour Plot of the Normalised Nusselt Number 39

Figure 24. Streamwise Maximum Nusselt Number 40

Figure 25. Boundary Layer at x = 1.2m 41

Figure 26. Wall Shear Stress Contour Plot [Pa] 42

Figure 27. Wall Shear Stress at x = 1.2m 42

Figure 28. Contour Plot of τ_{xz} Empty Domain vs Vortex Generator Domain 43

Figure 29. Contour Plot of τ_{yz} Empty Domain vs Vortex Generator Domain 44

Figure 30. Comparison of Main Vortex Circulation (Γ) and Spanwise Averaged Absolute Vorticity Flux (Ω) 46

Figure 31. Nondimensional Helicity at x = 0.6m, 0.9m, 1.2m, and 1.5m 49

Figure 32. Streamwise Helicity Flux for Main Vortex 50

Figure 33. Lamb Vector (nonlinear energy transfer) Contour Plot 51

Figure 34. Fluid Temperature Contour at x = 1.2m 52

Figure 35. Different Turbulence Model Spanwise St at x = 0.98m I

Figure 36. Different Turbulence Model Spanwise St at x = 1.88m I

Figure 37. Steady-state vs Transient State Spanwise St at x = 0.98m II

Figure 38. Steady-state vs Transient State Spanwise St at x = 1.88m II

Figure 39. Vorticity Contours for (a) Realizable k - ε, (b) Transient k - ε, (c) RSM, and (d) SST k - ω III

Figure 40. Front View of Domain Mesh A, B, C, and D IV

Figure 41. Top View of Mesh A, C, and D IV

Figure 42. Top View of Domain Mesh B IV

Figure 43. Top View of Mesh B V

Figure 44. Side View of Mesh B VI

Figure 45. Front View of Mesh B VII

Figure 46. Closeup of Vortex Generator Surface of Mesh B VII

Figure 47. Closeup 2 of Vortex Generator of Mesh B VIII

Figure 48. Bottom View of Grid Mesh D IX

Figure 49. Close Up View of Grid Mesh D X

Figure 50. Nondimensional Vorticity at (a) x = 0.58m and (b) x = 0.75m XI

List of Tables

Table 1. Grid Sizes for Mesh A to D 16

Table 2. Variation of Vortex Generator Configuration 18

Table 3. Fluid Properties [37] 19

Table 4. Vortex Characteristics for Mesh A to D 25

Table 5. Vortex Characteristics for Mesh A to D Continued 26

Table 6. Results for Stanton Number for Mesh A to D 27

Table 7. Comparison of Vorticity Area between Mesh A to D and the Experimental Model 29

Table 8. Deviation of St between Mesh A to D and the Experimental Model at x = 0.98m 30

Table 9. Deviation of St between Mesh A to D and the Experimental Model at x = 1.88m 30

1. Introduction

1.1 Background

Vortices and heat transfer and its application have received considerable attention in the HVAC industry. Vortices are generated in the fins of heat exchangers, using vortex generators or by modifying the shape of the fin surface. This is done to enhance the heat transfer in the fin chambers. Vortices enhance heat transfer by means of bulk fluid mixing. Johnson and Joubert [1] demonstrate the bulk fluid mixing by observing the thinning of the boundary layer on a vertical cylinder, placed in a wind tunnel, fitted with a row of delta winglet vortex generators. Johnson and Joubert [1] attributed the thinning of boundary layer to the presence of high shear stresses and because of the transfer of high momentum fluid into the boundary layer. This was caused by the trailing vortices created by the row of delta winglet vortex generators on the cylinder's surface.

There are three mechanisms, as specified by Fiebig et al. [2], for heat transfer enhancement:

1. Boundary layer thinning
2. Swirling flow or vortex development, and
3. Flow destabilisation

Two types of vortices are generated; longitudinal (streamwise) and transverse (spanwise) vortices. Longitudinal vortices are usually generated by wings or winglets at angle of attack less than 90°. Transverse vortex generators are cross ribbed where the vortex generator sits perpendicular to the main flow direction. Fiebig [3] reports that longitudinal vortices are better suited for heat transfer over transverse vortices. This is because longitudinal vortices exhibit better global heat transfer enhancement along the length of the heated surface, because the vortices extend for long distances downstream of the flow. Longitudinal vortices also provide an additional thermal energy transport. Transverse vortices only enhance heat transfer locally over the width of the heated surface. According to Fiebig et al. [2], transverse vortices produce double the flow losses when compared to longitudinal vortices and therefore should be minimised for heat transfer enhancement applications. Multiple longitudinal vortices can be generated to cover the width of the heated surface if necessary. Fiebig [3] has also stated that for heat transfer enhancement longitudinal vortices adhere to mechanism 1 to 3 while transverse vortices only adhere to mechanism 3 (from above).

Fiebig [4] has shown that delta shaped vortex generators are most effective at enhancing heat transfer, because of the reduced drag and due to fact that they produce longitudinal vortices of higher intensity. More favourable vortex generators used are winglets, because they offer better heat transfer enhancement while covering smaller surface area. Hence multiple winglets or winglet pairs can be placed on the surface of a fin surface. Fiebig et al. [2] also show how aspect ratio and angle of attack can better enhance heat transfer. Increasing aspect ratios and angle of attack can yield higher heat transfer. However, favourable vortex generator angle of attack is limited to 60°.

Vortices do not necessarily have to be generated by vortex generators. Fin surfaces can be modified such that they are corrugated (wavy fin surface) fins, or by including tubes through the fin surface. Tubes introduce longitudinal horseshoe vortices around the tube. Studies on the effects of tubes, running through fin surfaces, can be found in He and Zhang [5], and Song and Wang [6]. Corrugated fins produce transverse vortices along the troughs of the fin. Studies done by Alawadhi and Bourisli [7], and He and Zhang [5] demonstrate how wavy fin surfaces effectively enhance heat transfer over the troughs of the waves and how raising the amplitude of the waves increases this heat transfer. Corrugated fins are usually used for applications where enhanced local heat transfer is required. For this research project, longitudinal vortices generated by vortex generators are of interest, as they are most effective at enhancing heat transfer.

One of the problems with vortices and heat transfer is that the mechanism behind it is not fully understood. While research does exist correlating the fluid mechanics with the heat transfer, there is no detailed description of how the mechanism works. Eibeck and Eaton [8] observed the vorticity and circulation along a heated flat pate, but only observe the spanwise Stanton number at 4 different locations where the vortex is fully developed. They found two spanwise locations there exists a peak heat transfer and a significant drop in heat transfer adjacent to the peak.

Pauley and Eaton [9] further investigate the mechanism using delta winglet pair in the same flow channel. The aim of their experimental work was to determine the effects of varying vortex generator geometry and configuration on vorticity and circulation. They found that the closer the vortex is to the wall, the skin friction will decrease the streamwise circulation along the flow channel and this may decrease heat transfer.

Wu et al. [10] experimentally review the fluid mechanics side of the mechanism, by observing the change in the velocity profile and the vorticity over a delta winglet vortex generator. Heat transfer data were not monitored, but literature was used to correlate heat transfer with the changes in the vortex fluid propertied found at certain locations. Deb et al. [11] computationally observe the vorticity and velocity variations along a rectangular flow channel, with a delta winglet pair of vortex generators, but do not directly correlate the data with heat transfer data.

Lenmenand et al. [12], and Song and Wang [6] have used computational methods to determine the relationship between the spanwise averaged absolute vorticity flux and streamwise heat transfer. The vorticity flux considered all the vortices generated inside the domain and correlate them to the spanwise averaged Nusselt number. This correlation can prove that the vorticity flux has an influence on the heat transfer, however it does not explain the mechanism behind vortex heat transfer enhancement.

1.2 Problem Statement

Most of the published research in the field of heat transfer and vortices report on the effects vortices have on heat transfer parameters and pressure loss or drag. There exist very little research relating the fluid mechanisms of the vortices, itself, to the heat transfer. There are articles that investigate the flow structure of the vortices and relate them to the heat transfer, but this is mostly qualitative. To draw up more accurate conclusions a quantitative study, relating fluid dynamics to heat transfer, needs to be done.

Therefore, it is important for this study to the bridge the gap between the fluid dynamics of the vortex and its influence on heat transfer. Vorticity, circulation, and helicity should be investigated with the heat transfer in this dissertation.

1.3 Research Question

The core research question focuses on understanding the effect of the vortex mechanism like vorticity and circulation on convective heat transfer.

The core research question can therefore be reduced to:

- What are the fluid mechanisms that aid vortices in convective heat transfer enhancement?

1.4. Objectives

The objectives of this research project are to:

1. Investigate how vorticity and circulation effect on heat transfer.
2. Investigate how helicity can be used to predict heat transfer enhancement.
3. Identify the parameters that influence heat transfer enhancement.

1.5 Structure of Report

The report begins with the literature review (section 2.1), where experimental and computational studies are reviewed and scrutinised. Section 2.2 reviews the experimental work done by Eibeck and Eaton [8]. The important findings are shown in figures 8 and 9 from the studies. Section 2.3 reviews the computational turbulence models to use for the research and highlights the appropriate RANS turbulence model to use. Section 3 describes the methodology used to acquire the data. In this section, the computational model is presented along with the assumptions used for the computational simulations. Section 4 presents the turbulence selection, mesh independence, validation, and verification for the computational simulation. In section 4.1, the mesh independence is analysed and reviewed for various grid sizes. Section 4.3 is the validation section where the computational results are compared to the experimental data. 4.4 is the verification section, where the computational data is compared to theoretical data. Section 5 present the computational results and discusses the results with other literature and theory. Section 6 summarises the conclusions made from the results and discussion and is followed by the recommendations in section 7.

2. Literature Review

2.1 Vorticity and Heat Transfer

The earliest research that studied the effect of vorticity and heat transfer has been dated back to the 1980s by Eibeck and Eaton [8]. Eibeck and Eaton's [8] research will be discussed in section 2.3. Research related to vorticity or vortex strength and heat transfer is relatively scarce compared to the thermodynamic research with vortices and heat transfer. This research does not couple the heat transfer data with velocity or vorticity data.

Lenmenand et al. [12] investigated the effect of momentum and heat transfer in a square duct computationally. Hairpin vortices were generated using a trapezoidal vortex generator in a 7.6 x 7.6 x 33.15cm flow channel conveying water. The aim of the research was to investigate the extent of the effects of streamwise vorticity flux on heat transfer enhancement. The vortex generator was placed on the bottom of the flow channel and the size and configuration was kept constant. The bottom surface was made from steel and was heated to 370K. The velocity was kept low to 0.16m/s resulting in a low Reynolds number of 2080. Lenmenand et al. [12] had observed a pair of counter-rotating vortices around the tip of the trapezoidal vortex generator, a pair of counter-rotating vortices at the top corners, and two single vortices at the bottom corners of the duct. Lenmenand et al. [12] represented the secondary flow by using the streamwise vorticity flux along the flow channel. The Nusselt number was determined and compared to the vorticity flux. Figure 1 show a comparison between the normalized Nusselt number and the streamwise vorticity flux. From figure 1 the Nusselt number and the vorticity flux increases exponentially upstream of the vortex generator. Downstream of the vortex generator, the Nusselt number and the vorticity flux decreased exponentially. From the figure the Nusselt number and the vorticity follow the same exponential trend and indicates that the vorticity does influence the heat transfer in the flow channel.

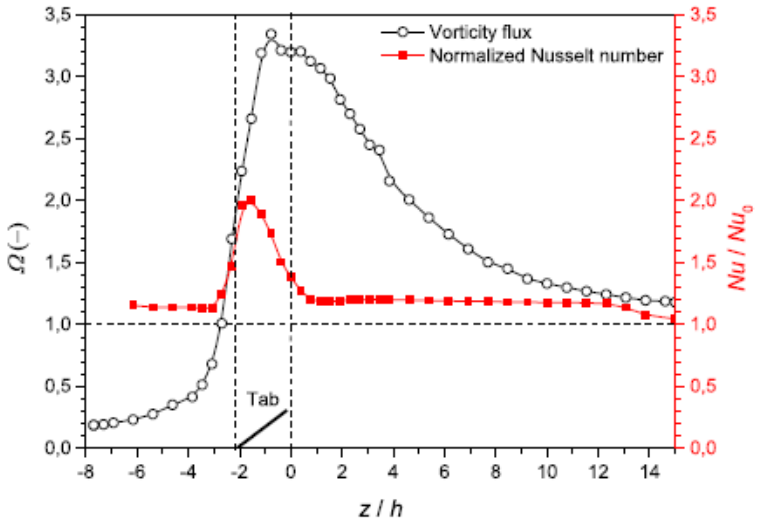

Figure 1. Longitudinal Vorticity Flux vs Normalized Nusselt Number [12]

Song and Wang [6] observed a similar trend when investigating vorticity and heat transfer, numerically, over a bank fin flow channel. The numerical model consisted of two half flat tubes, with two delta winglet vortex generators surrounding each flat tube on the upper and lower surface of the fin. All vortex geometry and configurations were kept constant. The Reynolds number was kept between 0 and 1800 so that the viscous modelling was kept laminar. Figure 2 below shows the sectioning of the bank fin section for computational analysis. Song and Wang [6] observed a strong symmetrical vortex pair with high vorticity flux behind the first vortex generator adjacent to the first

tube. This vortex had propagated to the centre of the flow channel until the vortex interacted with the first vortex generator of the second tube. The secondary flow was re-energized, and this increased the vorticity flux. Figure 3 shows the relationship between absolute averaged vorticity flux (J_{abs}) and Nusselt number (Nu) in the streamwise direction. The chart, in figure 3, shows what was observed by Song and Wang, and it also shows how Nu and J_{abs} follows the same trend. There are two major peaks for both the Nu and J_{abs}. The Nu increased to peaks at the same locations as the vorticity flux's (J_{abs}) peaks. Each major peak was located behind each of the first vortex generators adjacent to each tube. Each major peak was followed by a minor peak (smaller in amplitude). The minor peaks were located behind the second vortex generators adjacent to each flat tube. Song and Wang represent the relationship between vorticity and heat transfer with varying Reynolds number, as shown in figure 4. The chart shows that the straight lined for Nu and J_{abs} both increase with increasing Re at virtually the same gradient.

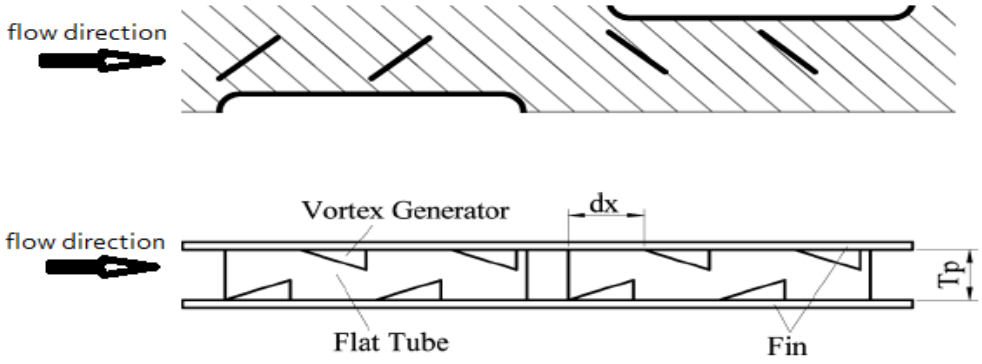

Figure 2. Schematic of Section Modelled by Song and Wang [6]

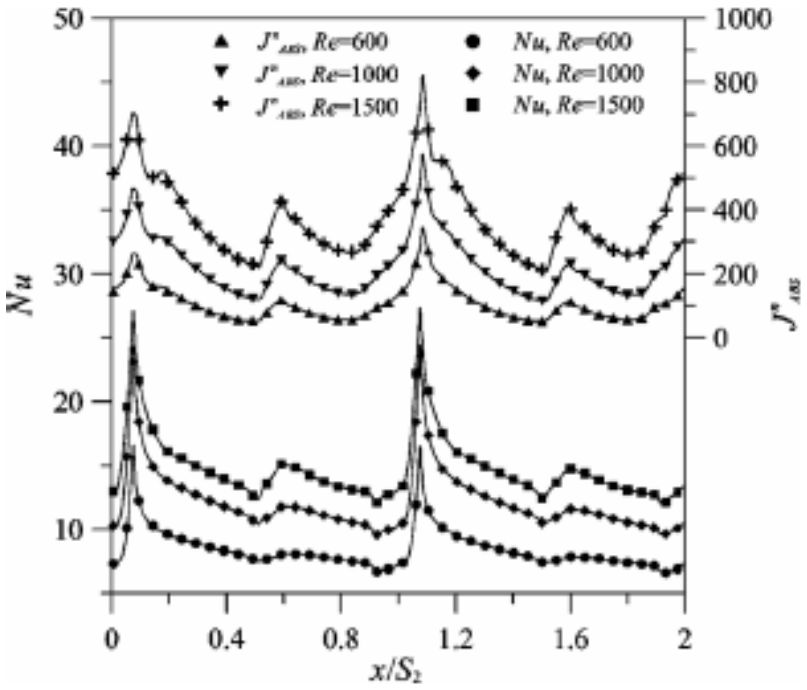

Figure 3. Streamwise Nusselt Number and Absolute Average Vorticity Flux Variations in the Flow Channel [6]

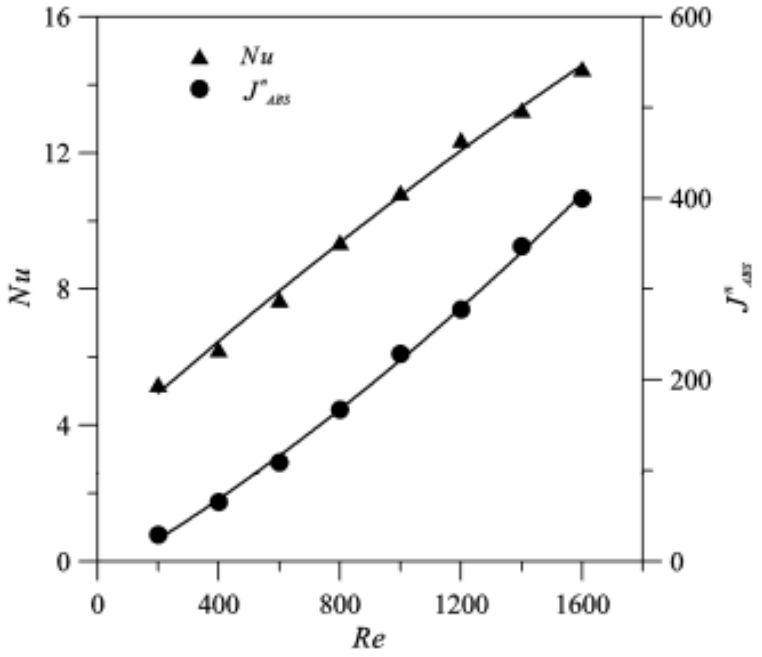

Figure 4. Linear Representation of Nu and J_{abs} with varying Re [6]

Wu et al. [10] have suggested that the turbulence intensity and the turbulence length scale have an influence on the heat transfer rate. Their experiment was setup in a wind tunnel with a test section consisting of a flat aluminium plate with a single delta winglet vortex generator place on the upper part of the surface. Wu et al. [10] observe two regions of flow: a downwash region, and an upwash region. Looking at the velocity in the spanwise direction, the downwash region is such that the velocity vector moves toward the plate, while the velocity vector moves away in the upward direction in the upwash region. The downwash region has higher streamwise velocity near the plate than the upwash region. These regions also have their own vortices; downwash being the main vortex, and the upwash vortex being the induced vortex. Figure 5 shows the velocity vector plot, from Wu et al. [10], and specifies the inflow (downwash region) and the outflow (upwash region). The figure also shows the formation of a main vortex (M) and an induced vortex (I). Both vortices have a core where there is a significant velocity drop (or velocity deficit) and a peak in turbulence intensity. The results from the study suggests that there is possibly a region of heat transfer rise at the downwash region, and a significant drop in heat transfer at the upwash region. Wu et al. [10] speculate that the heat transfer is high at the downwash region and low at the upwash region by observing the difference in the velocity in the boundary layer. Figure 6 shows the velocity profile for the inflow, outflow, and the vortex-less flat plate. This shows how the velocity is higher near the heat transfer surface for the downwash region when compared to the boundary layer for a flat plate. The upwash region has a lower velocity than the flat plate boundary layer. The turbulence length scale peaked at the core of the main vortex but dropped to a minimum value at the core of the induced vortex. These were mechanisms that were discussed to show why the heat transfer was high at downwash region as opposed to the upwash region. Wu et al. [10] do not show any heat transfer data but speculate about what causes the variation in heat transfer by comparing their fluid mechanic findings to the heat transfer data from other research.

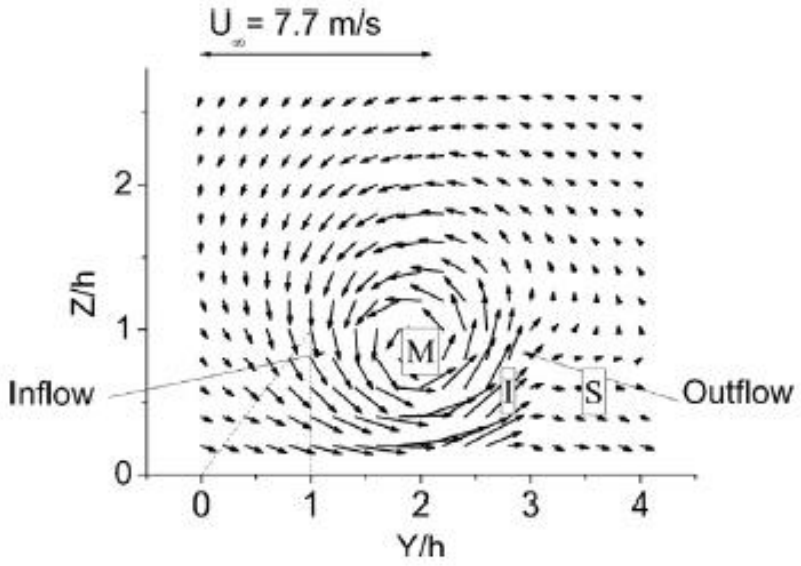

Figure 5. Wu et al. [10] Velocity Vector Profile of the Flow

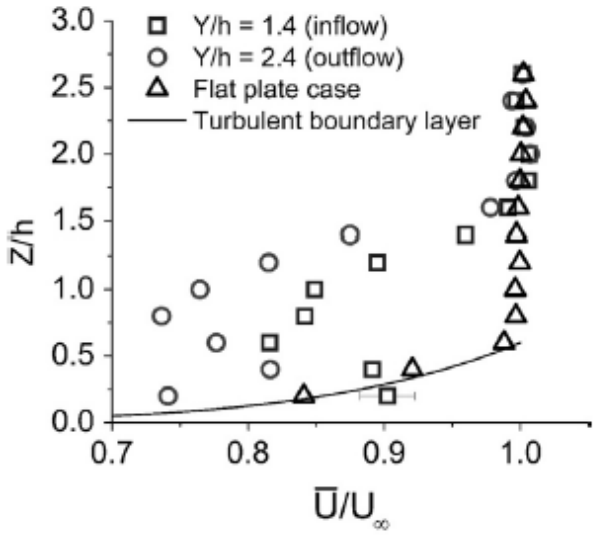

Figure 6. Velocity Profile for Inflow, Outflow, and Flat Plate Case from Wu et al. [10].

2.2 Shear Stress, Vortices, and Heat Transfer

Work done for vortices, shear stress, and heat transfer does exist. However, none of the articles link the shear stress to the circulation or vorticity of the vortex.

There is literature that positively correlate longitudinal vortices to shear stress, such as papers from Ge et al. [13], Wang et al. [14], Choi et al. [15], and Guo and Li [16]. To determine the correlation Ge et al. [13], and Wang et al. [14] use the two-point correlation theory. Ge et al. [13] studied the effect of near-wall streamwise vortices on the streamwise and spanwise shear stress using direct numerical simulations (DNS). Counter-rotating vortices were imposed on a flat plate to study this correlation. Wang et al. [14] used DNS to simulate flow over a wavy surface. Both researchers found the same correlation, but Ge et al.'s [13] is more relatable to this study as it features flow over a flat plate. Ge et al. [13] found that when the streamwise shear stress is negative or very low, then the fluid is moving

away from the wall. Likewise, if the fluid is moving toward the wall then there will be an increase in shear stress. Hence, downwash flow leads to high streamwise shear stress, while upwash flow leads to a drop in streamwise shear stress. Furthermore, they conclude that the spanwise shear stress corresponds to the footprint left behind by the vortex. The stronger the vortex the bigger the footprint. Counter-rotating vortices lead to shear stress of opposite shear stress signs.

On the topic of heat transfer and shear stress, Nirmalkar et al. [17] use drag to investigate shear-thinning. Drag or parasitic drag is a function of shear stress, hence why it was used to determine shear-thinning of the boundary layer in the numerical project. A freestream flow was imposed on a heated sphere in a 2d domain, and the Nusselt number was estimated and compared with the drag behind the sphere. Nirmalkar et al. [17] conclude that the shear-thinning promoted the rate of heat transfer over the sphere. This is caused by the yield zone size being restricted by the shear stress.

As can be seen from above, research related to vortices, heat transfer, and shear stress is rather scant. To the best of the authors knowledge, not much can be deduced from the presented articles about the vortex properties and heat transfer. There is also not much information on spanwise shear stress and heat transfer. Most research deals with drag or skin friction and heat transfer.

2.3 Validation Data

Eibeck and Eaton [8] have experimentally studied the effects of vorticity and heat transfer utilising a single delta winglet vortex generator. The experiment was conducted in an open-circuit, boundary-layer wind tunnel with a flow speed of 16m/s. The test section was a 0.61x0.127x2.11m rectangular flow channel. A turbulence grid was place at the entrance of the test section. This turbulence grid provided a freestream turbulence intensity of 0.3% at the inlet. The heat transfer surface was located 0.76m from the entrance. The heated surface was made from steel foil at 0.076mm thick. The surface was heated to a constant temperature of 45°C and 160 Thermocouples were embedded on the heated surface and used to monitor temperature changes on the heated surface. Mean-velocity data were used to determine the vorticity, velocity, and other vortex properties.

Single delta winglet vortex generators were used to generate vortices in the flow channel. Five different vortex generator variations were used. The variations included changes in angle of attack, and vortex generator height. Each variation had the effect of changing the strength and size of the vortex generated. The setup for the experiment can be seen in figure 7. Note that the location for the origin is 76cm from the entrance, 30.5cm from the sidewalls, and the bottom surface of the flow channel (0cm from the bottom surface).

Eibeck and Eaton's [8] results show the generation of Rankine vortices over the entire length of the flow channel. Vorticity data was shown for two different locations (1. x = 60cm, and 2. x = 120cm). Temperature data were processed to determine the Stanton number along the length of the flow channel. Results for spanwise Stanton were calculated for 4 locations (x = 45cm, 75cm, 105cm, and 135cm). These results are shown in figures 8 and 9. Note that the Stanton number was normalized with the streamwise Stanton number along the flow channel.

Eibeck and Eaton [8] have recorded a boundary layer of 1.3cm just before the leading edge of the vortex generator at 48cm from the entrance of the flow channel. A vortex core was observed from figure 7 for the velocity and the vorticity contour plots. This core consists of a velocity that is 90% of the streamwise velocity in the channel. This is also the region where the vorticity is the highest as can be seen by the contour plot in figure 8.

Overall Eibeck and Eaton [8] have concluded that longitudinal vortices of moderate size and strength have a significant effect on the heat transfer enhancement over the entire heated flow channel. Therefore, heat transfer enhancement is potentially enhanced by high vorticity strengths. Eibeck and

Eaton [8] attributed the effects of longitudinal vortices on heat transfer to the "*distortion of the mean velocity field*", as opposed to the turbulent field.

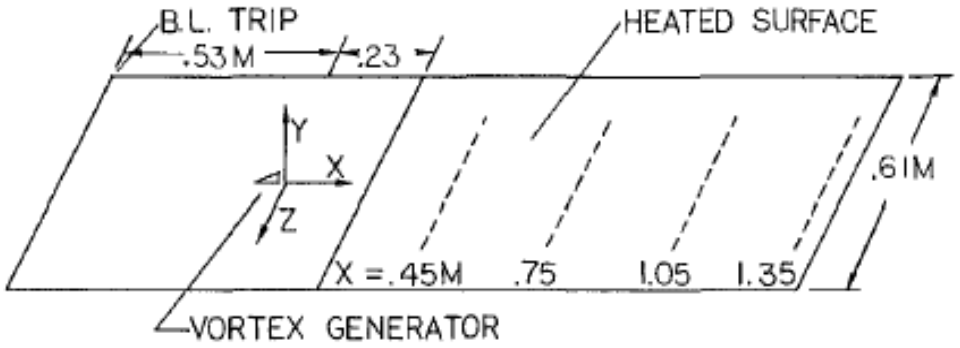

Figure 7. Layout of Experimental Model [8]

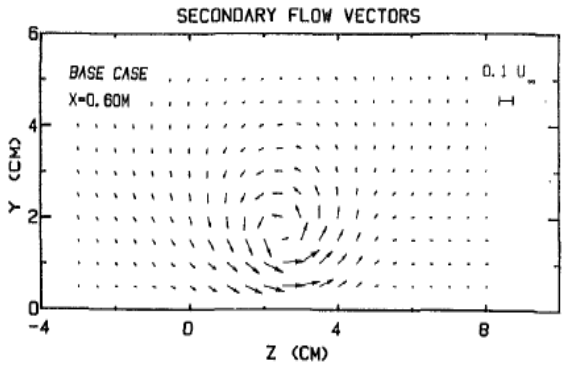

Fig. 4(*a*) Mean-velocity data for the base-case vortex at $x = 60$ cm; secondary flow velocity vectors

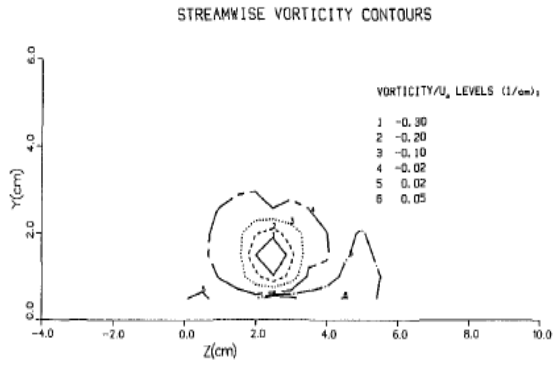

Fig. 4(*b*) Mean-velocity data for the base-case vortex at $x = 60$ cm; axial vorticity = Ω/U_∞

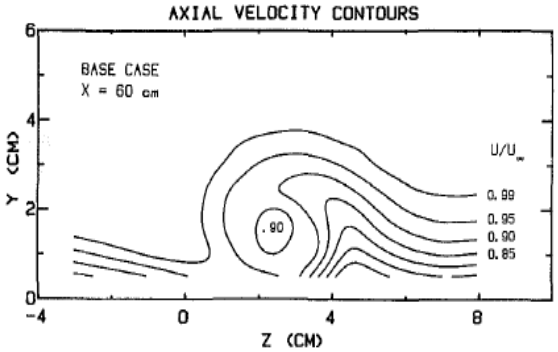

Fig. 4(c) Mean-velocity data for the base-case vortex at $x = 60$ cm; axial velocity = U/U_∞

Figure 8. Velocity and Vorticity Results[8]

Figure 9 shows the normalised Stanton number variation over the span of the heat transfer surface. The Stanton number was normalised with the Stanton number variation for the empty flow channel. The peak was located at the downwash region and the minimum values were located at the upwash region, much like the findings from Wu et al. [10].

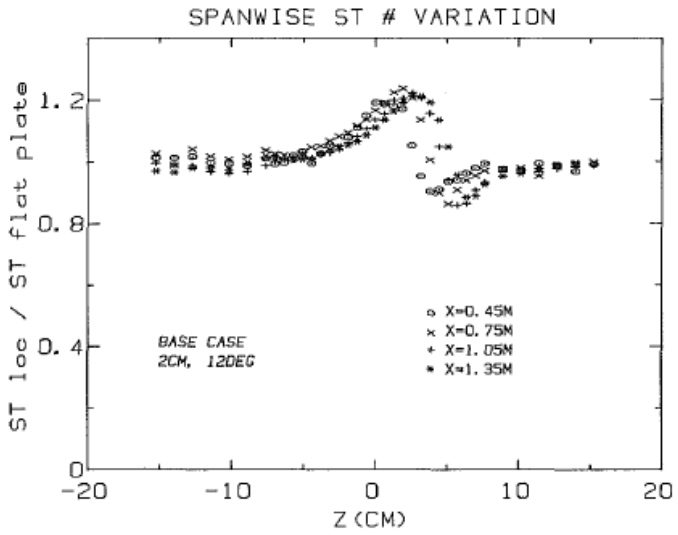

Figure 9. Spanwise Stanton Number at 0.45m < x < 1.35m [8]

2.4 Computational Fluid Dynamics

2.4.1 Viscous Models

Deb et al. [11] have shown that Reynolds Averaged Navier Stokes (RANS) models produce a 6% deviation from experimental data for vortex modelling, which is considered acceptable. To obtain more accurate results for vortices, Large Eddy Simulations (LES) should be chosen. However, LES models require finer meshing for accurate solutions. This however results in longer computation costs and would require high performance computing.

The ANSYS FLUENT computational fluid dynamic (CFD) software was used as it possessed the RANS and LES turbulence models required for the study. Deb et al. [11] had modelled, computationally, vortices in a flow channel with delta winglet vortex generator pairs in a flow channel identical to Eibeck and Eaton [8]. In this case the k - ε model was chosen with a scalable wall function. The results obtained were within reasonable accuracy compared to the validation data used.

This section will focus on the appropriate RANS viscous models that were chosen for the computational fluid dynamics (CFD). RANS models include, but are not limited to, Sparlart Almaras, k - ε, and k - ω. The Reynolds Stress Model add an extra five equations to the ε and ω based RANS model. Three viscous models that are considered for the computational approach; the k - ε, k - ω, and the Reynolds Stress Model (RSM). Reynolds Stress models have been used by Lenmenand et al. [12] and have produced acceptable solutions for their CFD models. Reynolds Stress models are computationally expensive, sensitive to initial conditions, and require high quality meshes. However, the advantage of RSM over the two equation RANS models, is the rejection of the isotropic turbulence assumptions.

One of the downsides of the two equation RANS models are the assumption that the turbulence is isotropic. Especially with the Realizable k - ε and SST k - ω model the turbulence viscosity is assumed to be isotropic. Isotropic turbulence implies that the square of velocity and the derivatives

are independent of direction[18]. Therefore, the turbulence fluctuates uniformly in all directions of the domain. This assumption is too idealistic when modelling turbulence and may lead to errors in the estimation of the vortex flow in the domain.

2.4.1.1 RANS k - ε Model

k - ε is a two equation RANS model that solves the turbulent kinetic energy (k) and the dissipation of the turbulent kinetic energy(ε). This model is favourable because of it offers good convergence for low computational cost. The model is generally used for external flows [19] but can be incorporated in channel flows. This model, however, does have its limitations and should be used with caution. The equations for k and ε are derived with the assumption that the flow is fully turbulent and that the molecular viscosity effects are negligible. Therefore, the model can yield inaccurate results for near wall solutions. This "stresses" the importance for choosing a wall function that must yield accurate results for wall heat transfers and shear stresses, etc. The default wall function for the k - ε model is the standard wall function. The accuracy of this wall function is dependent on the overall Reynolds number of the flow. The standard wall function is adequate for flows with high Reynolds numbers, but deteriorates for flows with low Reynolds numbers. At $y^* \approx 15$ (dimensionless distance from wall) the wall function deteriorates and can produce errors in the solution hence accuracy cannot be maintained. This requires the near wall boundary to be sufficiently covered with enough cells to model the boundary layer, hence $y^+ < 1$.

Other limitations include the adverse pressure gradients, difficulty in solving the rate of dissipation term (ε), isotropic turbulence is assumed, and the end walls must be no-slip boundary conditions [19]. One of the main limitations of the k - ε model, with regards to vortex flow lies with the equation for ε. The ε tries to dissipate the eddy flow much quicker than would be in a real-life situation. Research by Armfield and Fletcher [20] attribute the k - ε model's poor prediction of vortex flow to its overestimation of eddy viscosity, which is much larger that experimental eddy viscosity. They suggest modifying the ε equation to include the Richardson correction factor to reduce the eddy viscosity. Many vortex researchers modify the ε equation to minimise the dissipation rate, or in other cases, try to include an augmented dissipation rate (as found in research by Saqr et al. [21], and Chenoweth et al. [22,23]) to achieve much better vortical flow predictions with the model. Rahman et al. [24] use the realizable k - ε model, amongst standard k - ε and SST k - ω, to investigate 2D vortical flow around a cylinder. They state that the realizable k - ε model was best suited for the visualisation of vortex shedding behind the cylinder, because the model captures separating flow better than the standard model.

FLUENT contains of three variants of k - ε; standard, RNG (Renormalisation-Group), and realizable. These variants are different in the way they calculate the k, ε, and turbulent viscosity (μ_t). In the standard k - ε the k term was derived from an exact equation, while the ε term was derived from the "physical reasoning" [25] and has very little resemblance to its "mathematically exact counterpart" [25]. The realizable k - ε variant came highly recommended since an exact equation was used to derive the ε term. This exact equation came from the "mean-square vorticity fluctuation" [26]. The realizable variant also differs from the standard variant in that it contains an alternative form for the turbulent viscosity parameter. The variant also satisfies constraints on Reynolds stresses, hence why it is realizable k - ε. The variant also improves the wall boundary layer under strong adverse pressure gradients as opposed to standard k - ε models.

2.4.1.2 RANS k– ω Model

k – ω is another two equation RANS model, much like k - ε, however instead of dissipations, the specific rate of dissipation (Ω) is evaluated. The model differs from k - ε because it can model near-wall interactions with higher accuracy [19]. The mesh sizing for the near wall region does not need to be refined to obtain accurate solutions for boundary layer and heat transfer by the wall. This is

because the near wall treatment, in k - ω is automatically controlled based on the mesh near wall cell size.

The wall function for the model is similar to the Menter-Lechner wall function available to the k - ε model, which is a y^+-insensitive near-wall treatment [27]. According to the ANSYS theory guide the ω equation (from k - ω) is integrated into the viscous sublayer [28]. This allows for an y^+-insensitive wall treatment because the equation blends the viscous sub-layer and the logarithmic sub-layer based on the near wall y^+. This means that the wall treatment is automatically adjusted based on the near wall y^+ from the mesh. For better heat transfer predictions, it is recommended that the mesh near wall grid be sized for $y^+ \leq 1$. The boundary layer must be resolved with a minimum resolution of 10-15 cells as stated in the ANSYS FLUENT theory guide[29].

The drawback to this model is that the solutions are difficult to converge (compared to the k - ε model), its sensitivity to initial conditions (more specifically inlet boundary conditions) [30], freestream sensitivity (k and ε values outside the shear layer), and its tendency to over-predict flow separation.

The Shear-Stress Transport variant of the k - ω model was the most recommended turbulence model for the application of flows where vortices or swirling flow is present. This model accounts for the turbulence shear stress in the turbulent viscosity equation. The model also predicts separations and reattachment zones more accurately than the standard k - ω or the k - ε model. However, according to the ANSYS FLUENT manuals [31], for smooth walls, the prediction of flow separation can be over-estimated.

2.4.1.3 Reynolds Stress Model (RSM)

When simulating swirling flows, Reynold stress model (RSM) comes recommended by many researchers. Ridluan et al. [32] states that the model is best suited for "*capturing swirl flow effects in comparison with measurements."* [32]. Ridluan et al. [32] studied the swirling flow in a vortex combustor using the RSM, standard k - ε, RNG k - ε, and SST k - ω turbulence models. The research showed that while all models were in good agreement with experimental data, the RSM model yielded better flow prediction at the top of the vortex combustor. Lenmenand et al. [12] use the RSM model to model corner vortices inside their square flow channel, and it perfectly predicts flow not only at the wake of the vortex generator, but at the corners of the flow channel. According to the ANSYS FLUENT 2021 theory guide [33], the RSM models are accounts for the effects of swirling flow, and rotational flow in a more rigorous manner than the RANS models leading to more accurate predictions for more complex flows. RSM should also provide more accuracy, compared to k - ε and k - ω, because the isotropic assumptions fall away with this model.

The RSM model is a seven-equation turbulence model that calculates individual Reynolds stress terms. It differs from the RANS models in that it solves the transport equations for each individual Reynolds stress. According to the ANSYS FLUENT 2021 theory guide [33] the transport equations are derived by taking the moment of the momentum equation. RSM models accounts for the dissipation rate and pressure-strain using ε, or ω equations found in the k - ε and k - ω models. This can lead to potential inaccuracy issues if dissipation rates are not modelled properly. See Jawarneh and Vatistas [34], and the ANSYS FLUENT theory guide [33] for the RSM transport, pressure-strain, and dissipations equations.

2.5 Summary

From the literature, Lenmenand et al. [12] and Song and Wang [6] show how vorticity strength and Nusselt number (or heat transfer) follow the same trend, with a sharp increase behind the vortex generator and an exponential drop downstream of the vortex generator. Wu et al. [10] experimentally

show the flow past a delta winglet vortex generator in a rectangular flow channel, which is similar to the setup of the domain in this research. They identify two regions: a downwash region, and an upwash region. These regions are further identified as the main vortex (downwash region), and the induced vortex (upwash region). Eibeck and Eaton [8] identify the same flow regions and further analyse the spanwise heat transfer at different locations. Using the spanwise Stanton number, Eibeck and Eaton [8] show that under the downwash region there appears to be a region of high heat transfer, whereas under the upwash region there appears to be a region of minimum heat transfer.

The domain for this research resembles that of Eibeck and Eaton's [8] experimental model. The resulting domain is rectangular with air flowing at 16m/s over a delta winglet vortex generator that is at 12° angle of attack and spans 20mm. It is expected that the research should have vorticity, velocity, and Stanton number results that resemble the results found in Eibeck and Eaton [8]. Therefore, their research is used for validation purposes. Wu et al. [10] provides information on how the swirling flow should appear at the wake of the vortex generator. Therefore, in this study, it is expected to find two vortices that are formed because of downwash motion and upwash motion.

For this research the realizable k - ε, SST k - ω, and Reynolds Stress Model (RSM) were considered for the Computational simulations. Ideally the RSM model should yield better results for vortex flow since it does not dampen out the eddy flow as rapidly or assume isotropic turbulence as the k - ε model, but the model was computationally expensive to simulate. For the k - ε and k - ω models, there should be a higher rate of dissipation of the eddy flows leading to parameters such as vorticity and velocity to be lower than what is expected in the experimental model.

What was not found in the literature search was the link between wall shear stress, caused by vortices, and heat transfer. Since shear stress is a function of the fluid viscosity, and viscosity is linked to the transport of momentum, the parameter can give an indication of vorticity and locations where boundary layer thinning is likely to occur. Research done by Ge et al. [13], and Wang et al. [14] correlate streamwise vorticity to spanwise and streamwise wall shear stress. They both conclude that the streamwise vorticity correlates well with the spanwise shear stress as opposed to the streamwise shear stress. However, Ge et al. [13] identified a region of maximum streamwise shear stress under the downwash region of a horseshoe vortex and a minimum shear stress under the upwash region. This shows that the streamwise and spanwise shear stress are important parameters for the study of vortices and heat transfer.

3. Methodology

The first step of the project was to carry out a literature review of studies that are related to effects of vorticity and circulation on heat transfer. From the literature review, the sizing of the vortex generator and domain was found. A rectangular domain with a single delta winglet vortex generator in the common flow up configuration was used for the study. Eibeck and Eaton's [8] experimental research report was used to validate the computational results obtained. ANSYS v19 software was used for the computational analysis.

A 3D model of the flow channel was modelled in Spaceclaim and the enclosure tool was used to model the fluid domain inside the flow channel. The fluid domain was sectioned so that the mesh could be refined in volumes where the vortex was dominant and surfaces where the heat transfer was applied. Once this was done, Gambit software was used to create an appropriate mesh for the domain. A triangular prism structured mesh was used for the computational analysis. Four different grid sizes were used for the mesh. Each mesh was compared to determine which mesh provided the most accurate results with the lowest computational costs. The mesh that met this standard would be used for the computational simulation.

The FLUENT solver was used to perform the computational process for the domain. The steady-state realizable k-ε turbulence model was chosen for the data acquisition. More details about the computational analysis can be found in sections 3.1 to 3.4 of this report.

Reynolds number, Stanton Number, Nusselt Number, vorticity, velocity, fluid and surface temperature, and helicity were determined from the computational analysis. The results for the Stanton number and vorticity were compared to the results from Eibeck and Eaton [8] for validation purposes. The boundary layer and the drag coefficient were determined in domain and compared to the theoretical drag coefficient and boundary layer for verification. The velocity parameters and vorticity parameters were implemented in the appropriate equations to determine the circulation and the vorticity flux. Details on the equations used to solve the parameters can be found in the data processing section 3.6

3.1 Domain Model and Meshing

For this research, Eibeck and Eaton's [8] experimental model was replicated in ANSYS. Figure 10 and figure 11 show the schematic of the domain and dimension of the vortex generator used in the computational analysis. Note all the dimensions are in m. The domain is 40cm wide, 12,7cm high, and 200cm long. The delta winglet vortex generator was 2cm high, 5,1cm in chord length and positioned such the angle of attack with the flow field was 12°. The location of the (0,0,0) x-y-z coordinate is as shown in figure 10. The 0 coordinate (reference frame) is resting at the bottom surface, at the centre of the domain, at the inlet.

The model of the flow channel was meshed in Gambit. Four different meshes were compared for the best solution vs computation time. To aid with accurate results, for each mesh, the maximum skewness as well as the orthogonality and aspect ratio of the cells were checked. For all meshes, the near wall cell sizes were sized such that $y^+ < 1$. This was done so that the boundary layer at the walls would be accurately represented. The near wall grid size was estimated using the methods from F.M. White's Fluid Mechanics textbook [35]. Inflation was used to model the near wall boundary layer with 15 layer of growth rates between 1.2 and 1.5. This was done so that the cells would gradually adapt to the cells on the logarithmic sublayer of the domain. The orthogonality and the skewness were kept above 0.01, and below 0.9 respectively.

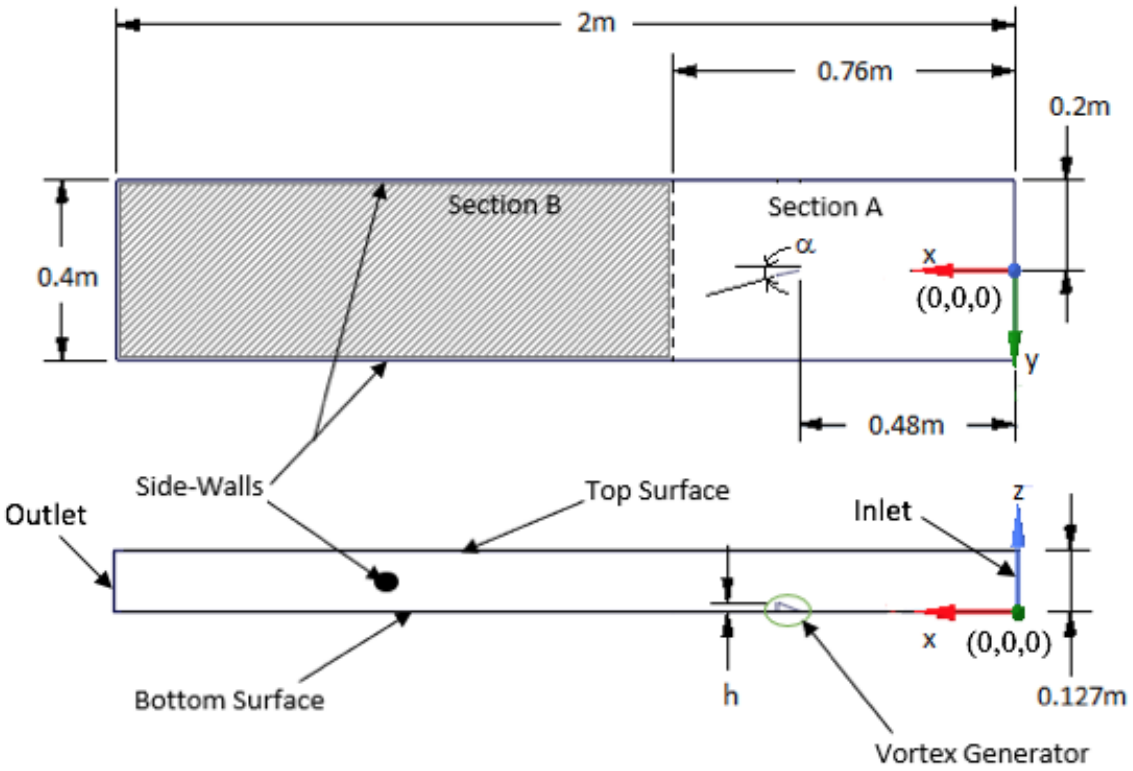

Figure 10. Schematic of Domain/Flow Channel

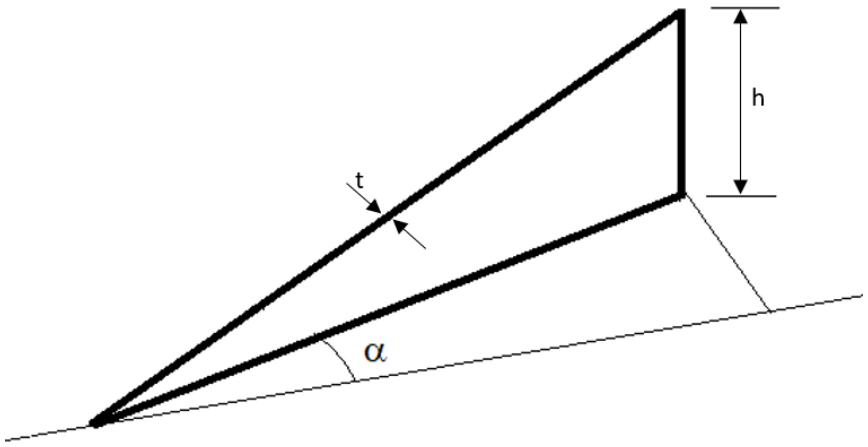

Figure 11. Schematic of Vortex Generator

The side walls, inlet, and outlet were divided into two sections; an upper part, and a lower part. The bottom surface was split into two sections; the entrance (or unheated surface), and the heated surface. Triangular prism shaped cells were used throughout the domain since quad shaped cells would cause high levels of skewness and very low orthogonality within the domain. The mesh was structured near the entrance of the vortex generator and downstream of the vortex generator. The mesh surrounding the vortex generator was kept unstructured, because of the irregular shape of the vortex generator. Results from four different mesh sizes were compared with one another and were also compared to the experimental results from Eibeck and Eaton [8]. This will be discussed in the validation section 4.3. Table 1 below lists the mesh sizing and the resulting mesh statistics.

Table 1. Grid Sizes for Mesh A to D

Mesh	A	B	C	D
Number of Cells	2601937	3795026	4913110	9658044
Element Size (mm)				
Bottom Surface	3	2.5	2.5	2.5
Lower Sidewall	6.5	3.5	2.5	2.5
Upper Sidewall	10	8	6	3.5
Top Surface	12	10	8	5
Vortex Generator	0.5			
First Layer of cell Size ($y^+ < 1$)	1.5×10^{-2}			
Inflation Growth Rate	1.5	1.45	1.45	1.2
Layers	15			

In Mesh A,C, and D the cells adjacent to the inlet was kept unstructured, while the section downstream of the vortex generator was structured using face meshing. The element size at the bottom surface was kept consistent between the two sections so that the cells of the unstructured section can gradually integrate with the structured section. This would prevent the element skewness from exceeding 0.9 in the entire meshed domain.

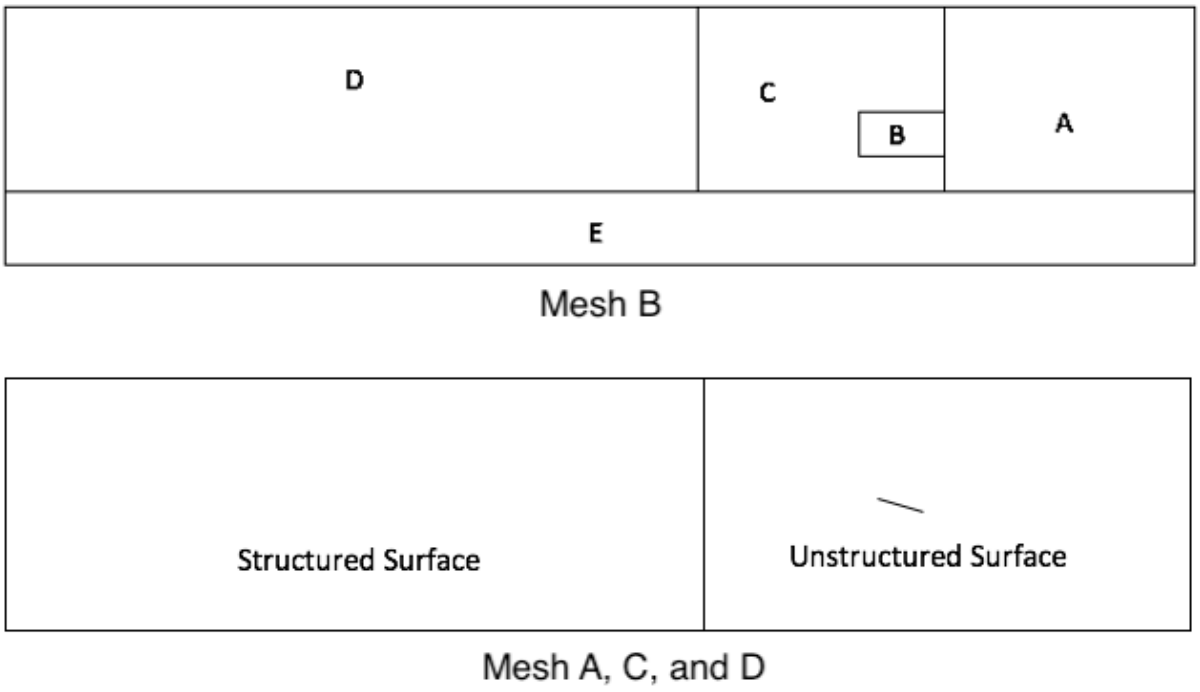

Figure 12. Sectioning of Bottom Surface for Meshes A,C, and D (bottom) and Mesh B (top)

Mesh A, C, and D were computed from the mesh technique discussed above, however for Mesh B the base of the domain was sectioned in 7 parts. The area surrounding the vortex generator was meshed separately from the rest of the domain so that the cells are more refined around this region, and a coarser mesh could be used at the surfaces away from the vortex generator. Referring to figure 12, the element sizes for the bottom surface A, and B adjacent to the inlet were 2.5mm, while the surfaces C, and D, downstream of the vortex generator were 2mm. Surface E was sized at 5mm since at this region the vortex does not interact with the surface. Surface B and C was kept unstructured due to the presence of the vortex generator on surface B. The sharp edges of the vortex generator make it harder to produce a structured mesh around the vortex generator and attempting to do so would yield an overly refined mesh which would be computationally expensive. The goal of Mesh B was to create a mesh that was refined around the areas of interest and coarse around the area unaffected by the vortex generated. Applying inflation at the edges of the vortex generators allows for the separation of the boundary layer to be model over the vortex generator. The cells on surface B gets smaller from surface A, but is still slightly larger than the cells on surface C. This was done to allow the cells to adapt to the cells created by the inflation around the vortex generator.

Solution adaptation was considered for the meshes. PUMA (Polyhedral Unstructured Mesh Adaptation) would need to be used as the mesh may contain polyhedral structures. According to the ANSYS theory guide[36], if the mesh contains non-convex polyhedral cells, then these cells may not be correctly refined, and this would lead to inaccuracies. With PUMA only cells adjacent to the boundary are refined anisotropically, while the rest of the cells are refined isotopically. Isotropic refinement requires mesh elements with bounded aspect ratios, i.e., elements cannot be stretched [36]. This will result in highly refined mesh downstream of the vortex generator and this could lead to high computational expense.

Because vortices are being modelled using the isotropic RANS model, the method could overestimate or over-dampen the vortices due to the damping factor of the k - ε model. The vortices generated in the domain are weak and the damping factor of the turbulence model could result in the vortex disappearing quicker than expected with a highly refined mesh.

Table 2 below summarises the different cases and the alterations made to the domain for each case. From table 2, case 1 refers to the validation case, and case 2 was used for data acquisition. The base case is the domain that excludes the vortex generator Note that the domain parameters and dimensions are kept constant for the simulations.

Table 2. Variation of Vortex Generator Configuration

Case	h [cm]	Angle of Attack [°]	Surface Section A	Surface Section B
Base	0	0	Heated	Heated
1	2	12	Un-Heated	Heated
2	2	12	Heated	Heated

3.2 Selection of Turbulence Model

Simulations were performed to determine which turbulence model was best suited for the data acquisition. It was found that the k - ε model was best for the simulations. The k - ε model produces a more sustainable vortex than the k - ω model, whose vortex dissipated faster than the former. A Reynolds Stress Model (RSM) was also simulated; however, the results were inconclusive, and the computational expense was higher than the k - ε and k - ω models.

A k - ε transient flow run was also used to check whether the steady-state produces the same vortex and heat transfer results as the transient solution. The results of this simulation proved that the transient solution and the steady-state solution were similar, and the steady-state solution should provide adequate results for the research. The steady-state solution was suited for the simulations since the flow in the experimental model was fully developed, apart from it being computationally inexpensive.

3.3 Assumptions, Fluid Parameters, and Boundary Conditions

3.3.1 Assumptions

Computational analysis incorporates the Navier-Stokes equations to model the flow in the flow channel. The assumptions made was that the flow was:

1. Incompressible, hence density was kept constant, (since flow is not super-sonic),
2. in steady-state (flow is fully developed),
3. gravitation force was negligible, and
4. the flow was viscous.
5. In RANS k - ε and k - ω model, turbulence was assumed isotropic.

Assumption 1 holds true because the flow is sub-sonic (since airspeed is 16m/s) implying that the air density is virtually constant. Assumption 2 is appropriate since the study is looking at the vortex flow

after the flow is fully developed in the domain. Assumption 5 is a result of using the two equation RANS model when modelling turbulence.

3.3.2 Fluid Parameters

The governing equations for the laminar and turbulence regions are used from the ANSYS v2019 FLUENT software. As stated earlier, the realizable k - ε turbulence model was used to solve the fluid and heat transfer solutions for the domain. Table 3 summarises the domain fluid properties which were taken as constant since the bottom surface was heated at a relatively low temperature of 45°C. The fluid properties were taken at a reference temperature and pressure of 298.15K and 1 atm respectively[37].

Table 3. Fluid Properties [37]

Domain Working Fluid	Air
Density [kg/m^3]	1.225
Viscosity (μ) [kg/m s]	1.84 x 10^{-5}
Prandtl Number	0.73
Specific Heat (C_P) [J/kg K]	1007
Thermal Conductivity [W/m K]	0.02551

3.3.3 Boundary Conditions

Figure 10 shows the boundary conditions as displayed on the isometric view of the computational model. The boundary conditions for the flow channel are as follows:

A. Inlet

A velocity inlet was chosen for the inlet region. The freestream velocity was chosen based on the freestream velocity developed in the wind tunnel used in the experimental data [8]. In this case the freestream velocity (U_∞) was 16m/s while the *y* and *z* component for velocity was kept at a constant 0m/s. The turbulence parameters used for the inlet were chosen based on the parameters from Eibeck and Eaton's [8] which was 0.3% for intensity and 10 for viscosity ratio. The temperature at the inlet was kept constant at 298.15K or 25°C.

Note that in the experimental case the freestream velocity was assumed to be constant at 16m/s. Eibeck and Eaton [8] have conducted a spanwise survey of the of mean velocities at different heights above the heat transfer surface or wall (as they refer to it). It was found that the freestream deviation was practically uniform, with only a 0.1% deviation from the inlet velocity.

B. Outlet

A pressure outlet was chosen for the outlet boundary condition. The gauge pressure was set to 0Pa. The backflow temperature at the outlet was set to a constant value of 298.15K. The turbulence intensity and the viscosity ratio were kept at default 5% and 10 respectively.

C. Wall

There are four different wall boundary conditions for the computational model. The top and bottom surfaces (Section A and B) were set to no-slip wall boundary conditions. The heated wall (located 76cm from the inlet) was set so that the temperature was constant with no added heat flux to the system. The surrounding walls were treated as adiabatic where no heat is added or lost in the system.

The sidewalls of the flow channel were treated as free-slip walls, which was a wall where the specified shear stresses were set to zero. This means the tangential velocity at the wall is not zero, while the normal velocity was zero.

A constant temperature of 318.15 K was added to heat transfer surface section B for the validation case (case 1). For case 2 to 4, section A and B had a constant temperature of 318.15 K applied for the surface temperature. This was done because no information was given by Eibeck and Eaton [8] about the heat flux applied to the heated surface, only the temperature data was given.

3.4 Wall Treatment

For the implementation of the k - ε model, and RSM ε-based model the scalable wall function was used to model the near wall viscous layer. The scalable wall function mitigates the deterioration of the standard wall function when the refinement is $y^* < 11$. This is because the scalable wall function enforces the use of the log law function in conjunction with the standard wall function (see ANSYS Theory Guide [38] for wall function formula). If the cells are coarser such that $y^* > 11$, then the wall function is identical to the standard wall function. For the current research the scalable wall function was used with a near wall first layer of cells of $y^+ < 1$ thickness. Note all meshes are sized such that $y^+ < 1$ thickness. This was coupled with inflation that would gradually increase the cell thickness using growth rate so that the boundary layer would be adequately modelled with minimal errors.

The k - ω uses an automatic y^+ insensitive wall treatment that was discussed in section 2.4.1.2.

3.5 Computational Solution

Using ANSYS FLUENT, the CFD solution method was set so that pressure and velocity was COUPLED. Second order discretisation's was used to solve the solution for the momentum, turbulent kinetic energy, dissipation rate, and the energy equation.

Drag and heat transfer rates were monitored during the calculation process. The mass flow rate at the inlet and outlet was also monitored to determine if continuity was preserved. The residuals were monitored to check if the results had converged to an appropriate error. The continuity residuals could only converge at best to a value of 5×10^{-4}, while the velocity and energy residuals converged well below 10^{-6}. The residuals for turbulent kinetic energy and dissipation rate could only converge at 10^{-5}. This was reasonable because we are dealing with periodic flows, which has the tendency to oscillations of the residuals during the iteration process.

3.6 Data Processing.

The raw data were evaluated and processed in ANSYS CFD POST, Origin Pro 2019, and Excel. The FLUENT Custom Field Function Calculator was used to determine the Stanton Number. The Custom

Field Function Calculator facilitates the use of existing functions, provide by FLUENT, to create user defined functions that can be estimated during the CFD simulations[39].

3.6.1 Vorticity

The vorticity of the fluid in the domain was estimated using the curl of the velocity vector. The equation for vorticity vector is depicted below.

$$\begin{aligned} \omega &= \nabla \times \boldsymbol{U} \\ &= \left(\frac{\partial}{\partial x}, \frac{\partial}{\partial y}, \frac{\partial}{\partial z}\right) \times (u, v, w) \\ &= \begin{bmatrix} i & j & k \\ \frac{\partial}{\partial x} & \frac{\partial}{\partial y} & \frac{\partial}{\partial z} \\ u & v & w \end{bmatrix} \end{aligned} \tag{1}$$

In this study it was the streamwise vorticity that was calculated from the numerical solution, hence the *i* component of the vorticity. Therefore, the streamwise vorticity is predicted from the equation below:

$$\omega_x = \frac{\partial w}{\partial y} - \frac{\partial v}{\partial z} \tag{2}$$

To compare with experimental results, the vorticity was normalised with the freestream velocity (U_ω) in centimetres per second (cm/s) since Eibeck and Eaton [8] used the velocity in this form to normalise their vorticity results. The unit for streamwise vorticity is thus cm^{-1}.

The nondimensional form of the vorticity was used for the resulting vorticity plots in this research. This was done using the following equation:

$$\overline{\omega} = \frac{\omega_x h}{U_\infty} \tag{3}$$

From the above equation *h* is the height of the vortex generator and U_ω is the freestream velocity.

3.6.2 Circulation and Vorticity Flux

The circulation was determined using the double integral of the streamwise vorticity (ω_x), or:

$$\Gamma = \iint \omega_x \, dydx \tag{4}$$

The 2D integrate tool from OriginPro was used to determine the double integral from the contour plot of the streamwise vorticity.

The vorticity flux *J* is also a double integral of the absolute streamwise vorticity, but it considers the vorticity of the cross section of the domain. The equation for the vorticity flux is:

$$J = \frac{\iint |\omega_x| \, dydx}{\iint dydx} \tag{5}$$

The vorticity flux was converted to a dimensionless form called the vorticity density Ω (absolute cross-averaged streamwise vorticity flux). The equation for the vorticity density is as depicted below:

$$\Omega = \frac{JA}{\overline{U}h} \tag{6}$$

Where A is the cross-sectional area of the domain, $\overline{U}$ is the mean velocity at the section, and h is the height of the vortex generator.

For the research present here, the vorticity flux and vorticity density were only considered for the vortices generated by the vortex generators. To filter out any vortices generated by the walls (if any) the cross section was reduced to an area of (0.36m x 0.06m).

3.6.3 Helicity Density and Helicity Flux

The helicity density is the dot product of the velocity vector and the vorticity vector.

$$H = \boldsymbol{u} \cdot \boldsymbol{\omega} \tag{7}$$

It is a pseudo-scalar quantity and is nondimensionalised by the following equation.

$$\overline{H} = \frac{Hh}{U_\infty^2} \tag{8}$$

Where h is the height of the vortex generator, and U_∞ is the freestream velocity.

The helicity flux is the double integral of the helicity density and is evaluated with the equation below:

$$Helicity\ Flux = \iint H\, dydx \tag{9}$$

3.6.4 Nusselt Number

The Nusselt number was estimated from ANSYS CFD Post. The equation used to calculate the Nusselt number is depicted below:

$$Nu_x = \frac{hx}{k} \tag{10}$$

From the equation above, h is the convective heat transfer coefficient, x is the streamwise location along the flow channel, and k is the thermal conductivity of the fluid. The predefined Nusselt number in ANSYS uses the hydraulic diameter D_h instead of the streamwise x location. This Nusselt number was used instead of Nu_x. Therefore, the equation for Nusselt number becomes:

$$Nu = \frac{hD_h}{k} \tag{11}$$

3.6.5 Stanton Number

The Stanton number was solved using FLUENT's Custom Field Function Calculator estimated from the equation below:

$$St = \frac{h}{\rho c_p U_\infty} \tag{12}$$

From the equation above, ρ is the density of the working fluid, and c_p is the specific heat of the fluid. The parameters h and U_∞ are as stated above (section 3.5.4). The Stanton number relates the heat transfer to the heat capacity of the working fluid.

3.6.6 Wall Shear Stress

The wall shear stress on the domain heated surface is primarily due to the transport phenomena of the fluid. This transport phenomenon is related to the transport of momentum since shear stress is equal to the velocity gradient times the viscosity of the fluid.

The wall shear stress was estimated using the product of the time rate of change of strain and the effective viscosity μ_{eff} of the fluid. The equations for shear stress are:

$$\tau_{yz} = \mu_{eff}\left(\frac{\partial w}{\partial y} + \frac{\partial v}{\partial z}\right) \tag{13}$$

$$\tau_{xz} = \mu_{eff}\left(\frac{\partial u}{\partial z} + \frac{\partial w}{\partial x}\right) \tag{14}$$

For this research τ_{xy} is ignored as the shear stress varies along the axial direction and thus has no effect on the heat transfer. The effective viscosity was estimated using the equation below:

$$\mu_{eff} = \mu + \varepsilon$$

From the equation above, μ is the dynamic viscosity, and ε is the turbulent viscosity. Eddy viscosity was estimated using the FLUENT solver. The resulting wall shear stress is calculated from the equation below:

$$\tau_{wall} = \sqrt{\tau_{xz}^2 + \tau_{yz}^2} \tag{15}$$

The relation between shear stress and vorticity can be linked to the time rate of change of strain since they are parameters that are dependent on velocity gradients. The streamwise vorticity (ω_x) can be linked to shear stress τ_{yz}, while the shear stress τ_{xz} is linked to the streamwise velocity. By substituting equation 2 into equation 13 we get equation 16 below:

$$\tau_{yz} = \mu_{eff}\left(\omega_x + 2\frac{\partial v}{\partial z}\right) \tag{16}$$

4. Turbulence Model Selection, Mesh Independence, Validation, and Verification

The reference frame starts at the centre of the bottom surface at the inlet as depicted in figure 10.

4.1 Mesh Independence

In this section, meshes A to D are compared with one another, to determine how well they correlate. The vortex parameters and Stanton number are used to compare the various meshes to the experimental data. The mesh is considered independent when further refinement does not yield significantly divergent results from the less refined meshes. The grid formation of the mesh can be found in figure 43 to 49 in Appendix A2.

Table 4 and 5 lists the results for the velocity and vorticity at 1.13m and 1.73m (near the outlet of the domain) downstream of the trailing edge of the vortex generator. The vorticity and velocity were normalised by dividing the values by the freestream velocity (U_ω), so that the data could be compared with the experimental data.

From the data in table 4, we see how the vortex core varies from one grid size to the next. The focus for validation process was the size of the vortex generated, and the heat transfer data on the heated surface of the domain. The vortex generated was a Rankine vortex much like the vortex generated by the vortex generator of Eibeck and Eaton [8], and Wu et al. [10].

From table 4 and 5 we see that the vorticity starts to dissipate slightly as the mesh becomes more refined, however the lowest grid size mesh has a lower vorticity near the core. Of note, the vorticity at the core of mesh B was slightly stronger than the more refined meshes and was closest to the experimental solution. The centre of the core of the vortex is similar for all mesh sizes and the experimental solution at x = 1.13m, with only Mesh A having a 16.7% deviation from the experimental model. There is a 0.75cm deviation for the y coordinate of the core between the experimental model and the computational model, but this was because of the positioning of the vortex generator in the computational model. In the experimental solution the vortex generator was positioned such that the middle of vortex generator was on the centreline of the domain. In the computational model the leading edge of the vortex generator was placed on the centreline of the domain. Therefore, taking this into consideration, the y-position of the core is the same as the experimental solution. The sizes for the normalised vorticity at 0.1, and 0.02 were measured at x = 1.13m; and 0.02, and 0.05 at x = 1.73m. The results from the measurements showed that the vortex was shrinking as the mesh was refined.

Comparing the results for the different mesh sizes, we see that the size of the vortex gets smaller as the mesh becomes refined. This is commonly expected with k - ε and k - ω turbulence models. The turbulence dissipation equations will try to dampen out the vortices as quickly as possible. From the results, Mesh B and C have almost exact vortex sizes, with the deviation between results being at most 0.5% (at area A_2). The vortex sizes for Mesh A are not consistent with the rest of the mesh sizes and has a higher deviation of between 5% to 11% when comparing mesh A to B. This deviation in results gets larger when comparing mesh A to C and D (6% to 21%). Comparing Mesh B and C with Mesh D, we find that there is a deviation that is somewhat significant. When looking at area A_1 and A_2, the deviation is more apparent for area A_1 than A_2, where the deviation is 9%. Between area B_1 and B_2, the deviation is more significant at B_1 (2.5%). At B_2 the deviation is 3%, but because the experimental result for area B_2 is approximately equal to the computational result for mesh B and C, the deviation favours the coarser meshes (B and C).

Table 4. Vortex Characteristics for Mesh A to D

Vortex Characteristics at x = 1.13m					
Mesh	A	B	C	D	Experimental
Number of Cells	2601937	3795026	4913110	9658044	----------
Core (y,z)[cm]	(3.25 , 1.25)	(3.25 , 1.50)	(3.25 , 1.50)	(3.25 , 1.50)	(2.5 , 1.50)
Core Velocity (u/U_ω)	0.93	0.93	0.93	0.93	0.9
(a,b) length [cm] for ω = 0.02	(4.25 , 3.00)	(3.95 , 2.90)	(3.95 , 2.90)	(3.70 , 2.85)	(3.80 , 2.70)
Area A_1 [cm^2]	10	9	9	8.3	8.05
(a,b) length [cm] for ω = 0.1	(1.90, 1.70)	(1.8 , 1.7)	(1.9 , 1.6)	(1.90 , 1.60)	(1.80 , 1.60)
Area A_2 [cm^2]	2.5	2.4	2.39	2.39	2.28

Table 5. Vortex Characteristics for Mesh A to D Continued

Vortex Characteristics at x = 1.73m					
Mesh	A	B	C	D	Experimental
Number of Cells	2601937	3795026	4913110	9658044	----------
Core (y,z)[cm]	(4.75 , 1.4)	(4.75 , 1.75)	(4.80 , 1.60)	(4.75 , 1.70)	(4.00 , 1.75)
Core Velocity (u/U_ω)	0.93	0.93	0.93	0.93	0.9
(a,b) length [cm] for ω= 0.02	(4.80 , 2.90)	(4.40 , 3.00)	(4.40 , 3.00)	(4.30 , 3.00)	(4.30 , 3.00)
Area B_1 [cm^2]	10.93	10.38	10.38	10.13	10.13
(a,b) length [cm] for ω = 0.05	(2.5 , 2)	(2.5 , 1.8)	(2.49 , 1.8)	(2.43 , 1.8)	(2.5 , 1.79)
Area B_2 [cm^2]	3.93	3.53	3.53	3.43	3.53

Table 6 lists the Stanton number peaks, minimums and flat regions for meshes A to D and experimental data. Figures 13 and 14 shows the heat transfer graph for Stanton number, for x = 0.98m and x = 1.88m. Refer to figure 9 for the peak and minimum Stanton number for the experimental model. The Stanton number was normalised using the same technique as Eibeck and Eaton [8], i.e. dividing the spanwise Stanton number by the streamwise Stanton number of the empty domain. Mesh A to C have approximately the same results with minimal deviation. In figure 14, mesh D has a significantly lower minimum Stanton number at y = 0.04m (St/St_0 = 0.74), whilst in figure 15 the peak for mesh D is significantly higher at y = 0.03m (St/St_0 = 1.26). A reason for the deviation of mesh D could be due to the refinement of the mesh near the wall at the bottom surface. As shown in figure 13, mesh A has Stanton number data that agree with mesh B and C. However, in figure 14 mesh A has a Stanton number that is higher at y < -0.02m and y > 0.09m. This significant difference is due to the larger size (3mm) of the cells at the bottom surface grid.

Table 6. Results for Stanton Number for Mesh A to D

Mesh	A	B	C	D	Experimental
x = 0.98m					
Y < -0.08m	1.04	1.04	1.04	1.03	1
Maximum St/St_0	1.25	1.25	1.24	1.26	1.2
Minimum St/St_0	0.78	0.78	0.78	0.75	0.88
Y > 0.1m	1.01	1.01	1.01	1.01	0.98
x = 1.88m					
Y < -0.1m	1.01	0.99	0.99	0.99	0.95
Maximum St/St_0	1.23	1.23	1.23	1.26	1.21
Minimum St/St_0	0.72	0.72	0.72	0.71	0.9
Y > 0.16	1	0.97	0.97	0.97	1

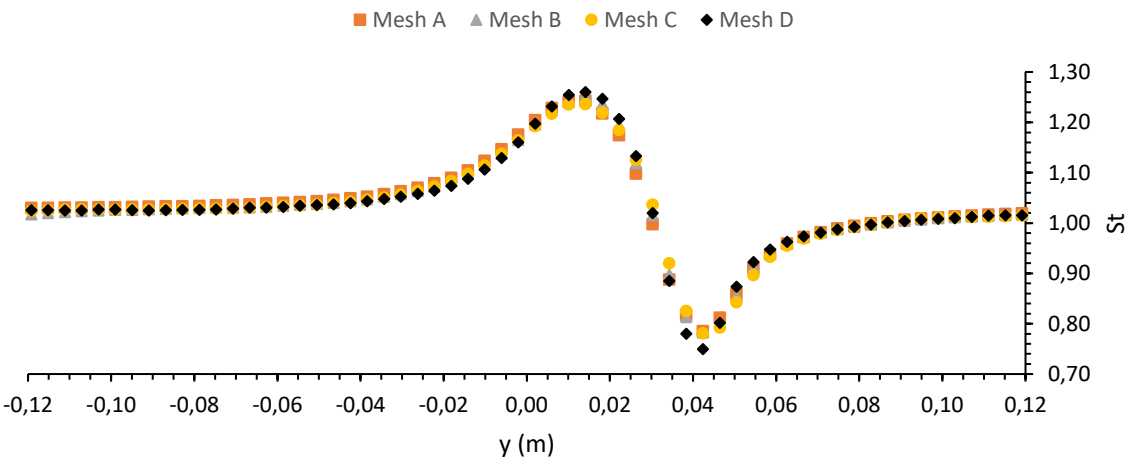

Figure 13. Spanwise Stanton Number at x = 0.98m

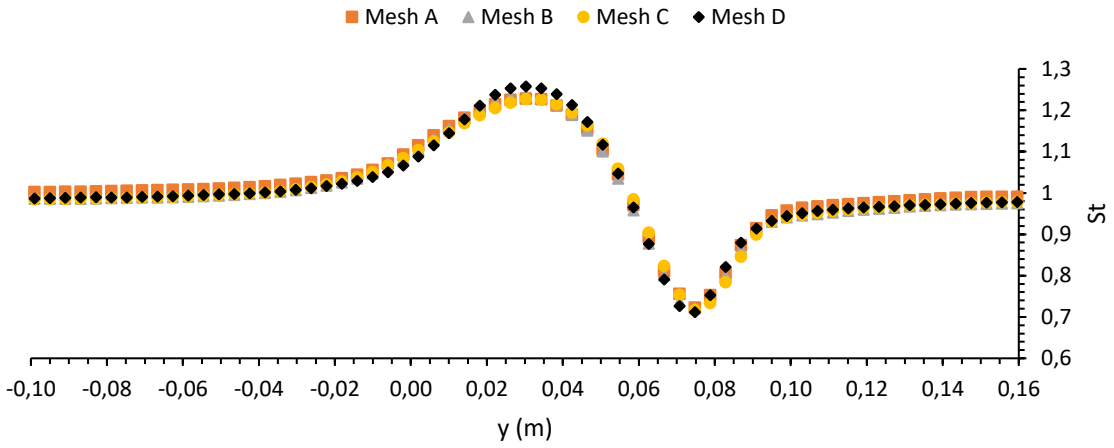

Figure 14. Spanwise Stanton Number at x = 1.88 m

4.2 Turbulence Model Selection

Simulations were performed using the RSM, Realisable k - ε, and the SST k - ω for the domain in this research. Mesh B was used as results obtained for circulation and vorticity were nearest to the experimental data, while simultaneously being computationally less expensive. The RSM was coupled with an ε based, linear pressure-strain model. The SST k-Ω model uses an automated near wall treatment, which is dependent on the near wall cell thickness. This was discussed in section 2.4.1.2. The near wall treatment used for the RSM ε-based model was the scalable wall function. This was done to determine how the RSM model could improve on the k- ε model with the same wall function.

The Realisable k - ε model was found to work best, as it produced a vortex that did not dissipate as fast as the SST k - ω model. This may be due to the k - ω near wall treatment being a blended viscous and logarithmic layer (which cannot be altered in FLUENT when $y^+ < 1$). The k - ω model does not consider the transport of turbulence shear stress which tends to overpredict the eddy-viscosity (as stated in the ANSYS FLUENT Theory Guide[30]) in the domain, leading to a quicker dissipation of the vortex. The SST k - ω model produced acceptable results for the heat transfer, however the Realisable k - ε results had better vorticity data comparable to the experimental data.

The RSM model should have produced better results compared to the k - ε model due to its anisotropic nature, but was inconclusive, mostly due to the resolution of Mesh B, where the cells in front of the vortex generator are less refined than the sides (Refer to section 3.1). As seen in figure 35 and 36 in Appendix A1.1, the Stanton number is more scattered along the spanwise direction (y-direction) when compared to the k - ε and k - ω models. This suggests that the model may have overpredicted the turbulence in the domain and this would be caused by the mesh resolution. The presence of this turbulence was not present in the experimental model.

As a conclusion the results in the main body of this dissertation was taken for a steady state k - ε turbulence model. Results showing the variation in the 3 turbulence models is show in Appendix A1.

4.3. Validation

In this section, the computational model is compared to the experimental model to determine which mesh works best for the data acquisition. As with section 4.1, the vortex parameters, Stanton number and boundary layer will be used to show which mesh works best, while being computationally inexpensive. In table 4 and 5, all meshes present a deviation of 3.33% when looking at the core velocity (u/U_∞). However, at areas A_1, A_2, B_1, and B_2 the deviations differ.

Table 7 lists the percentage deviations of mesh A to D to the experimental model. The sign convention is based on how much larger (+) or smaller (-) the area is. Areas A_1 to B_2 correspond to the area under the specified contours (A_1 corresponds to $\omega = 0.02$ at $x = 1.13$m; A_2 corresponds to $\omega = 0.1$ at $x = 1.13$m; B_1 corresponds to $\omega = 0.02$ at $x = 1.73$m; and B_2 corresponds to $\omega = 0.05$ at $x = 1.73$m). Mesh A deviates significantly more compared to the experimental model, which implies that the circulation is stronger than the experimental model. This could result in the heat transfer being over-estimated compared to the experimental case. Mesh B and C both have a significantly larger area (hence circulation) at $x = 1.13$m, but this is significantly dropped at $x = 1.73$m. The deviation from the experimental is lowest with Mesh D which would make it ideal to use, however the large negative deviation (-10%) at area B_2 suggests that the vortex is dissipating quicker with the more refined mesh, making it undesirable for this simulation. Mesh B and C are almost identical (apart from the slight deviation at A_2) and don't deviate negatively from the experimental model near the outlet of the domain, therefore these two meshes are appropriate for the modelling of the vortices.

Table 7. Comparison of Vorticity Area between Mesh A to D and the Experimental Model

Model	Mesh A	Mesh B	Mesh C	Mesh D	Experimental
Deviation A_1	+24.2 %	+11.8%	+11.8%	+3.1%	0
Deviation A_2	+9.65%	+5.26%	+4.82%	4.82%	0
Deviation B_1	+7.90%	+2.47%	+2.47%	0	0
Deviation B_2	+11.33%	0	0	-10%	0

For the Stanton number, the peak of the experimental data is 1.2 (at $x = 0.98$m) and 1.21 (at x = 1.88m). The peak for Mesh B and C is 1.25 (at x = 0.98m) and 1.23 (at $x = 1.88$m). Comparing the experimental Stanton number to the results of Mesh A to D, the biggest deviation of 21.11% appears at $x = 1.88$m where the Stanton number is at a minimum.

Table 8 and 9 lists the deviations from the experimental models for each mesh. The sign convention is positive for higher St and negative for lower St compared to the experimental model. Mesh D deviates the most for maximum and minimum St at $x = 0.98$m and 1.88m. At the region where Y < -0.08m Mesh D performs 1% better than Mesh A to C, but this is not a significant deviation closer to the experimental data. Mesh A deviates at 2% from Mesh B to D at Y < -0.1m (x =1.88m), but overall produces similar St results to Mesh B and C. The deviation for all meshes are highest when the Stanton number is on the minimum point. The significant deviation is highest near the outlet of the domain ($x = 1.88$m).

Table 8. Deviation of St between Mesh A to D and the Experimental Model at x = 0.98m

Mesh	A	B	C	D	Experimental
x = 0.98m					
Y < -0.08m	+4.0%	+4.0%	+4.0%	+3.0%	0
Maximum St/St_0	+4.2%	+4.2%	+3.3%	+5.0%	0
Minimum St/St_0	-11.4%	-11.4%	-11.4%	-14.8%	0
Y > 0.1m	+3.1%	+3.1%	+3.1%	+3.1%	0

Table 9. Deviation of St between Mesh A to D and the Experimental Model at x = 1.88m

x = 1.88m					
Y < -0.1m	+6.3%	+4.2%	+4.2%	+4.2%	0
Maximum St/St_0	+1.65%	+1.65%	+1.65%	+4.13%	0
Minimum St/St_0	-20%	-20%	-20%	-21.1%	0
Y > 0.16	0	-3.0%	-3.0%	-3.0%	0

The reasoning for the deviation could also be attributed to the resolution of the apparatus used to calculate the velocity and the heat transfer data. 37 thermocouples were used to acquire temperature data from the experiment of which the uncertainty was stated to be ±0.2°C [8]. The computation result uses 100 data points on the surface of heated surface, which should provide highly detailed heat transfer information compared to the experimental results. The mesh resolution, and scalable wall treatment may have also contributed to the deviation since they are dependent on thickness of y^+ at the near wall region. However, because the near wall cell thickness y^+ was less than 1, this should be minimal.

Figure 15 shows the variation of circulation in the streamwise direction between Mesh B and experimental data. It should be noted that Eibeck and Eaton [8] have only listed four data points for circulation (See table 2 of [8]) and have not plotted the data. The circulation is higher for the realizable k - ε computational simulation, but dissipates at a higher rate than the experimental model.

This is due to the artificial dissipation from the turbulence model. Between 30cm and 60cm, the experimental and computational models have almost the same gradient, but with a 10% difference. At 60cm to 90cm the experimental slope is higher than the computational, indicating a faster dissipating vortex. However, at 90cm to 120cm the experimental slope is getting shallower and is showing signs of converging to a constant horizontal line, presumably where the vortex will have constant circulation. The computational slope is almost consistent from 30cm to 120cm, showing no signs of slowing down, indicating the effect of the dissipation rate equation from the k - ε model. Additional experimental data on circulation would have more accurately confirmed the findings.

Figure 16 shows the velocity gradient for Mesh A to D. It shows that mesh A to D have virtually the same velocity curve. The boundary layer thickness is approximately 1.25cm for mesh A to B. This is approximately 3.85% lower than the estimated boundary layer thickness for the experimental model at the same location. This shows that the boundary layer thickness from the computational method was close to the experimental result for the boundary layer thickness at 48cm from the inlet.

Overall meshes B and C are better suited for the computational study. The deviation being mostly present for the minimum Stanton number, but table 8 and 9 shows that the deviations are less at maximum Staton number where the deviation is 4,2% to 1.65%. Referring to table 7 Mesh B and C both have a high percentage deviation 11.8% at x = 1.13m, for Area A1, but this drops to 2.47% at x = 1.73m. Referring back to the discussion of figure 15, both the computational and experimental model have a linearly decreasing circulation trend (with a deviation of 10%), up until x = 1.43m where the dissipation of the experimental vortex lowers compared to the computational model.

Even though the computational data match closely to the experimental data, there are still computational errors that have to be accounted for. Theses computational errors are presumably caused by:

1. the assumption that the turbulence is isotropic,
2. dissipation rate of ε eqaution, and
3. the resolution of the mesh chosen.

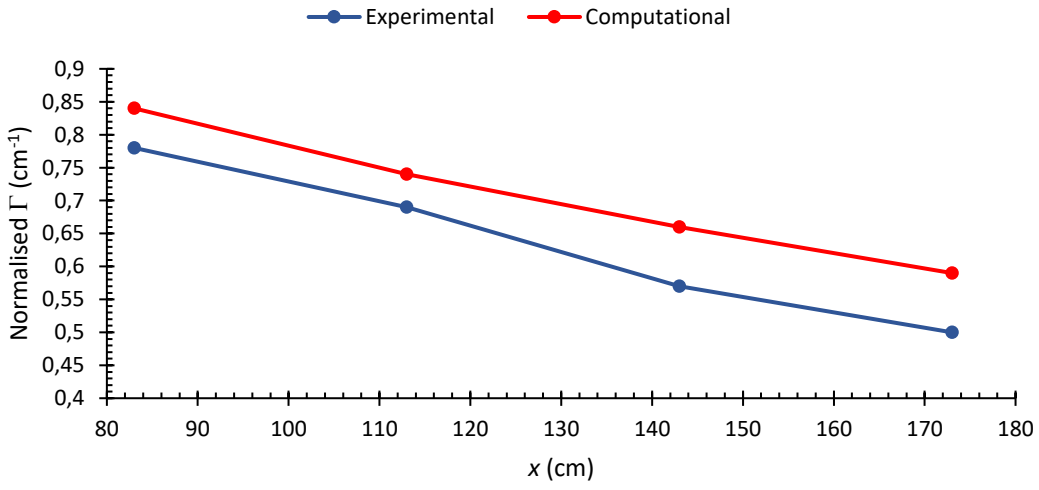

Figure 15. Comparison of Experimental and Computational Mesh B Circulation

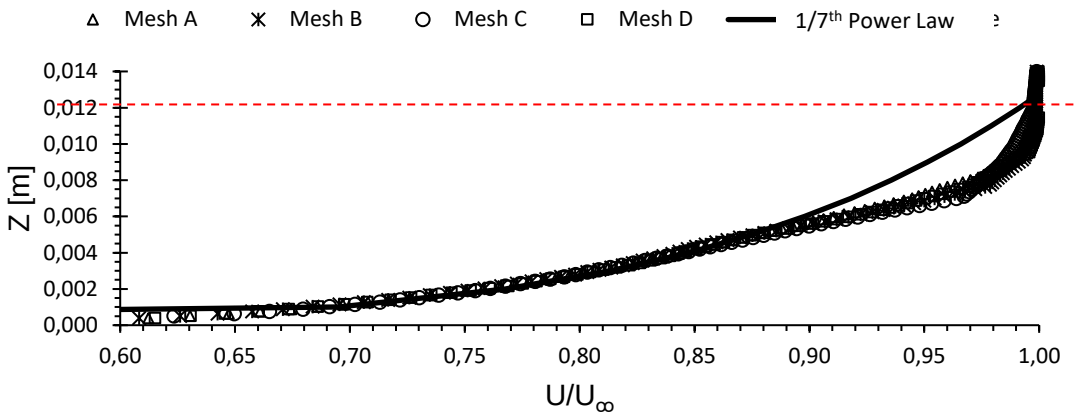

Figure 16. Velocity Profile for Mesh A to D

4.4 Verification

Figure 16 shows the theory-based velocity profile for the 1/7th power turbulence velocity profile described by the equation below. The estimated theoretical boundary layer was estimated at δ = 1.27cm, which is approximately 1.6% more than the simulation boundary layer thickness.

$$\frac{U}{U_\infty} = \left(\frac{z}{\delta}\right)^{\frac{1}{7}}$$

The displacement δ was calculated using the Blasius equation for turbulent flow.

$$\frac{\delta}{x} = \frac{0.37}{Re_x^{\frac{1}{5}}}$$

At region $0.88 < \frac{U}{U_\infty} < 1$ the velocity profile for the theory line is higher than the simulation velocity profile. The reason for this difference may be that the velocity profile was taken at the leading edge of the vortex generator. At this location the boundary layer starts to separate from the leading edge of the vortex generator.

The location at x = 48cm was chosen for the prediction of the boundary layer as this was the location Eibeck and Eaton [8] measured their boundary layer in the experimental model. Hence it was a location of interest, not only for validation, but for verification as well. The thickness was cited in the publication, but not represented in a chart.

4.5 Concluding Remark

From the above discussion it was shown (from table 6 – 8, and figure 13 to 16) that mesh B and C produce acceptable results for vorticity, circulation, and heat transfer, while noting the potential causes for the deviations in the results. Mesh A was too coarse for data processing and would have resulted in erroneous data. Mesh D (consisting of 9,6 million cells) overpredicted the dissipation (discussed in 4.3) of the vortices modelled and this would also result in erroneous data on top of being computationally expensive.

After careful consideration, Mesh B was ultimately chosen since the mesh is less computationally expensive compared to Mesh C. Therefore, for data acquisition mesh B was used for the results and discussion in section 5, on the next page.

5. Results and Discussion

5.1 Observations

5.1.1 Velocity and Vorticity

From the validation process, the boundary conditions for the domain and a grid size of mesh B are appropriate for running simulations for the varying vortex generator configurations.

Figure 17, 18, and 19 shows the velocity vector, velocity contour, vorticity contour plot at 1.2m from the inlet (x = 1.2m) of the domain. Take note that these plots and all subsequent contour plots are taken from the outlet to inlet perspective. Figure 17 shows the downwash region A presented by the vector arrows directed towards the bottom surface, while the upwash region B is presented by the vector arrows moving away from the bottom surface. The downwash region is often referred to as the inflow, while upwash is often referred to as outflow. There are two longitudinal vortices generated by the delta winglet; one formed by the downwash and stronger upward moving flow (see A from figure 17), and another formed in the upwash region. These vortices are often referred (Biswas et al. [40] and Wu et al. [10]) to as the main vortex(A), and the induced vortex (B). The main vortex is believed to be responsible for most of the heat transfer on the surface, while the induced vortex is the region where the heat transfer drops to a minimum. Wu et al. [10] states that the main vortex (A) brings cold air onto the heated surface and reduces the boundary layer in that region, while the induced vortex (B) conveys the hot air away from the main vortex into the surrounding.

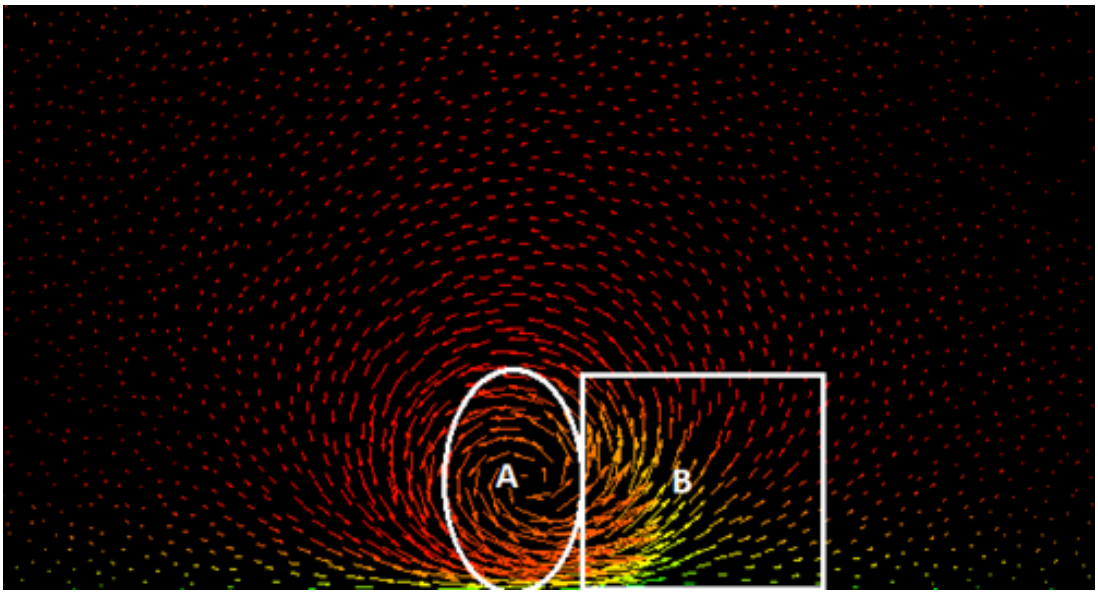

Figure 17. Velocity Vector at x = 1.2m

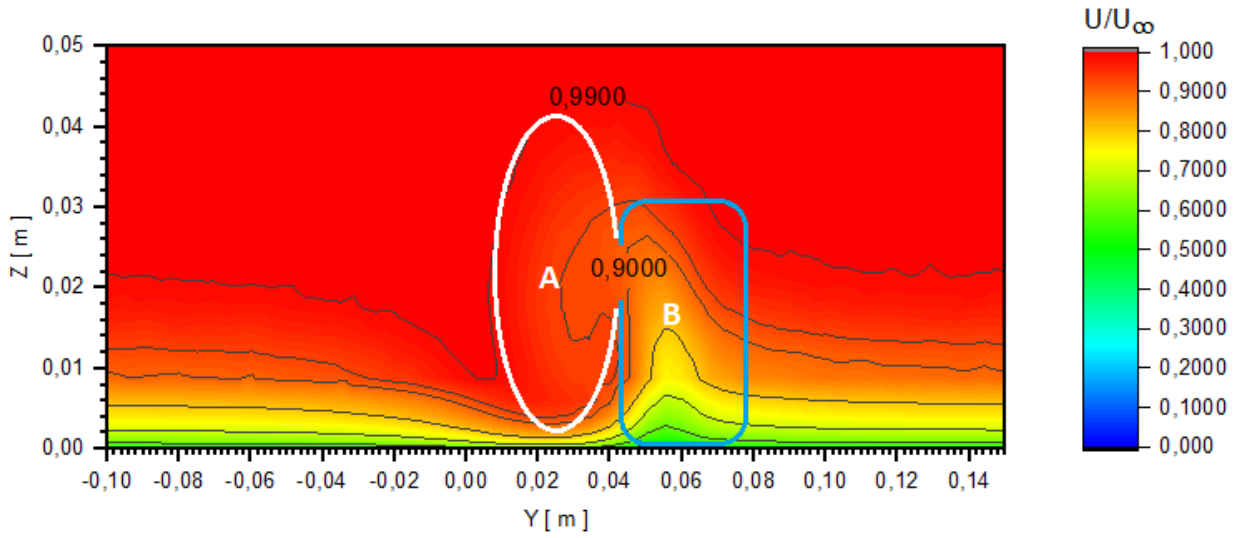

Figure 18. Streamwise Velocity Contour Plot at x = 1.2m

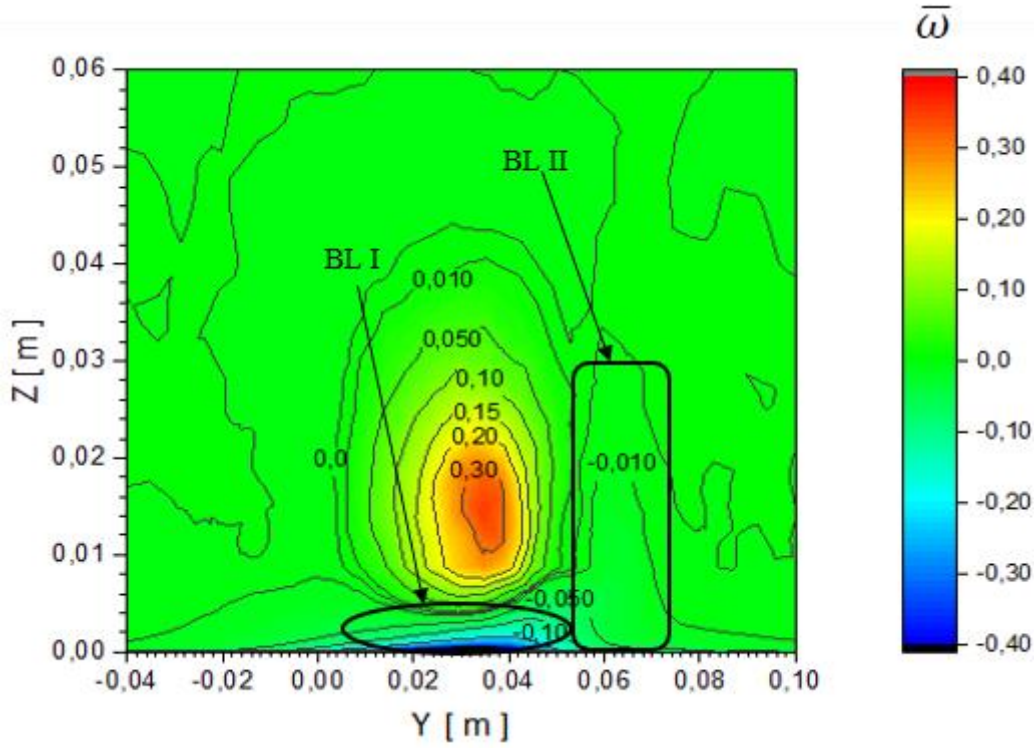

Figure 19. Contour Plot of the Nondimensional Vorticity at x = 1.2m

From figure 18, the boundary layer to the left of the main vortex (y < 0.01) reduces in thickness, while the boundary layer around region B increases because of the boundary layer mixing. In region B the upward moving fluid is carrying hot air at lesser speed than region A, as can be seen in figure 18. Wu et al. [10] argue that the decrease in the heat transfer, at the upwash region, could be caused by the velocity decrease at the region. They argue that when the flow from the inflow region moves to the outflow region, it is being heated and this lowers the heat transfer at the outflow region. The inflow and outflow region refers to the downwash and upwash region respectively. The movement of fluid

from the inflow region to the outflow region increases the thickness of the boundary layer. This potentially results in the drop in heat transfer, as can be seen in temperature plot in figure 21 under region B. Because there is higher temperature at this region, we can assume that this region is a region of minimum heat transfer.

From figure 19, we see main vortex in its fullest size, with a well-defined core, of vorticity $\bar{\omega} = 0.3$ and outer radius of vorticity $\bar{\omega} = 0.01$. Take note that this vorticity is nondimensional. BL I shows how the main vortex thins out the boundary layer underneath it. It appears that the main vortex is rotating counterclockwise and is applying a shear stress on the boundary layer. The shear stress is the mechanism by which heat is being transferred from the main vortex into the boundary layer. Area BL II is the region where the induced vortex appears. The vortex is moving clockwise and is forcing the boundary layer upward causing a thickening of the boundary layer. At this region shear stress is expected to be lower than the shear stress under the main vortex, hence there should be less heat transfer under the induced vortex. Shear stress will be discussed in more detail in section 4.5.5.

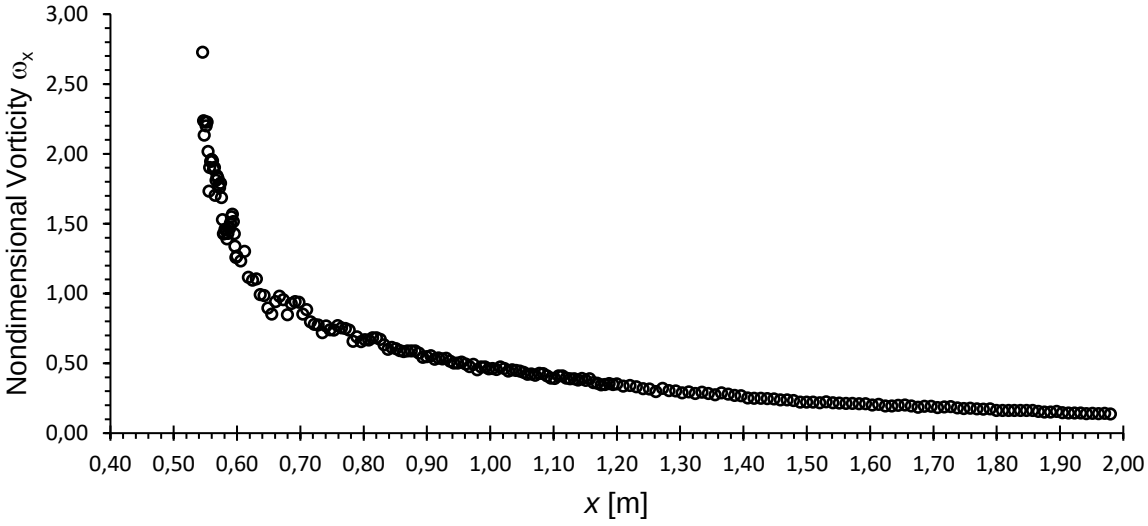

Figure 20. Streamwise Core Nondimensional Vorticity

The streamwise vorticity curve in figure 20 was taken by mapping a curve along the core of the longitudinal main vortex. This was done by tracing a line through the centroid of each vortex core at 16 locations along the streamwise *x* direction of the domain. From the chart we see that the core vorticity decreases exponentially along the streamwise direction.

The scatter of the data at 0.53m < *x* < 0.9m (figure 20) is caused by the accuracy of the mapped curve on the core of the vortex. This is because a series of straight lines were used to draw the curve in the centroid of the vortex core. The plotting of the straight lines in the domain assumes that the centre of the vortex core moves linearly from the start of each line to the end of each line. This is not always true in the case where 0.53m < *x* < 0.9m. However, at this location the vortex moves along the *z* axis, of the domain, more rapidly as the vortex leaves the trailing edge of the vortex generator. This is expected of the vorticity, however the rate at which the vorticity is dropping could be exaggerated by the dissipation rate equation (ε) within the k - ε turbulence model. This is why the core vorticity is lower than the core vorticity of the experimental data. The curve for the vorticity does not tell us much about the heat transfer enhancement, but it does highlight the problems that arise from using a k - ε model to model swirling flow. However, as shown in the validation section 4.3, the computational data are in good agreement with the data from the experimental work.

5.1.2 Wall Temperature and Vortex Evolution

Figure 21 shows the total temperature on the heat transfer surface, and the evolution of the vortex (seen by the contour lines on the y-z plane) along the streamwise direction of the domain. The figure shows the temperature drop under the main vortex and comparably higher temperature on the region under the induced vortex. Furthermore, we see that between location 0.6m < x < 1.2m, the temperature is lowest at the region that corresponds to BL I from figure 19. This shows that higher transfer corresponds to boundary layer thinning caused by the vortex. The higher temperature band appears under the outer contour of the induced vortex. This is where the boundary layer is rising and carrying hot air from the downwash region to the upwash region, hence why there is a higher temperature at this region. The temperature does drop to the temperature of the surroundings, while under the remainder of the induced vortex and is due to the hot air cooling down by the streamwise velocity in the domain and possibly the weak circulation of the induced vortex. From figure 21 the vortex grows larger in size; however, the vorticity decreases as the vortex continues downstream. Even though the vortex grows, we can see that the temperature gradually rises under the main vortex as the flow moves downstream. This is due to the decrease in the vorticity which inevitably leads to lower circulation which leads to a weak main vortex. The induced vortex is irregular in shape and hence conclusions cannot be made about the influence of the induced vortex's size or strength on heat transfer. This too is a problem that is caused by the ε equation in the turbulence model. An RSM or LES turbulence would lead to a more accurately depicted induced vortex.

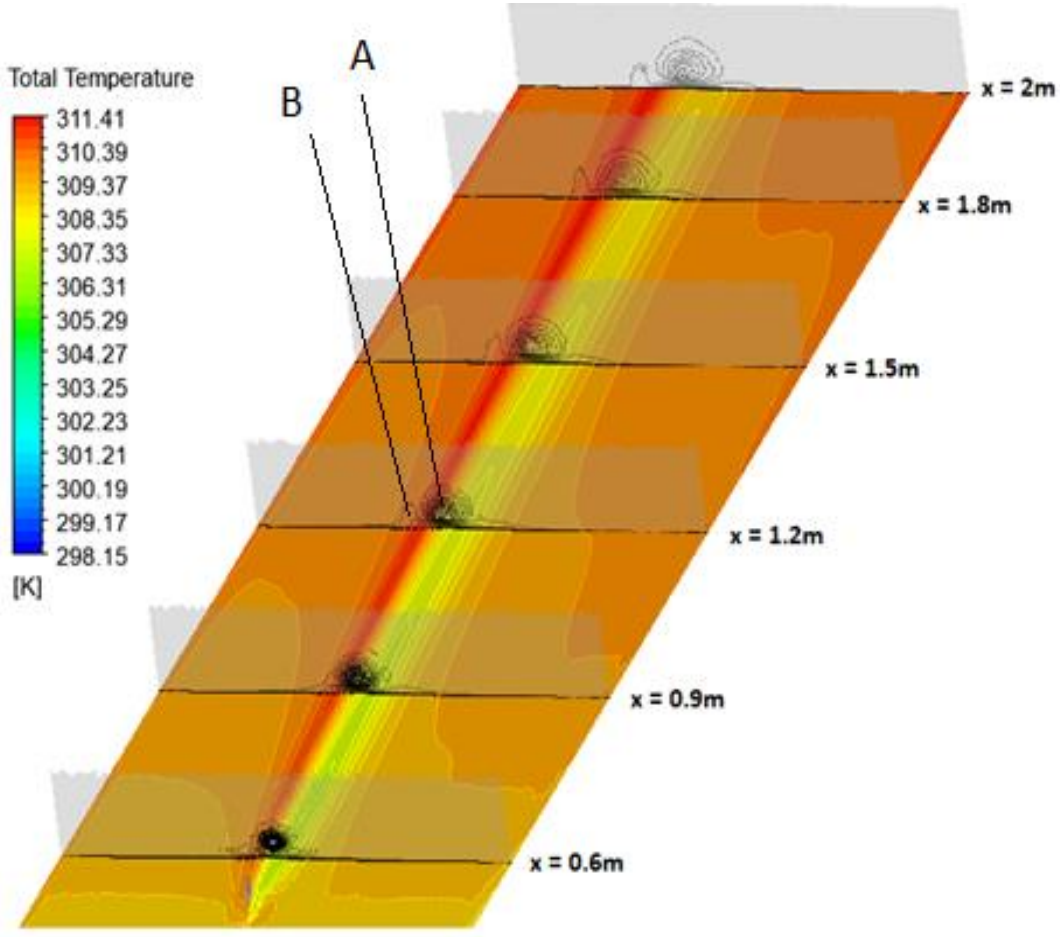

Figure 21. Streamwise Vorticity Contour and Temperature Distribution Along Flow Channel

5.1.3 Heat Transfer: Stanton Number and Nusselt Number

Figure 22 shows the variation of spanwise Stanton number from x = 0.6m to 1.5m. The Stanton number (St) was normalised with the streamwise Stanton number for the empty domain. The spanwise plot for St appears almost wave like, where the peak is at the inflow region (downwash) and the trough is at the outflow region (upwash). The width for both the inflow and outflow waves increases at increasing x locations. However, both amplitudes do drop as the vortex moves downstream from x = 1.2m. The plot shows a lower peak St at x = 0.6m, which increased at x = 0.9m (St ≈ 1.4). The St peak then drops from x = 0.9m to x=1.8m at $St \approx 1.35$. The amplitude for the trough is at its lowest at x = 0.6m, but then it rises at x = 1.2m ($St \approx 0.67$). Downstream of this location the trough drops in amplitude to roughly $St \approx 0.75$.

Looking at the Stanton number curve (figure 22), at x = 1.2m the St peaks at $y \approx 0.025$m, while the minimum St is located at y = 0.055m. The peak for the Stanton number lies within region A (see figure 17,18,19), or BL I (see figure 19) where the outer contour of the main vortex, i.e., the zero-vorticity contour, interacts with the boundary (rotating with negative vorticity) under the contour. The minimum value of the Stanton number lies near the side of the zero-vorticity contour between the main vortex and the induced vortex. At this region the boundary layer is raised, carrying hot air from the heated surface through the upwash.

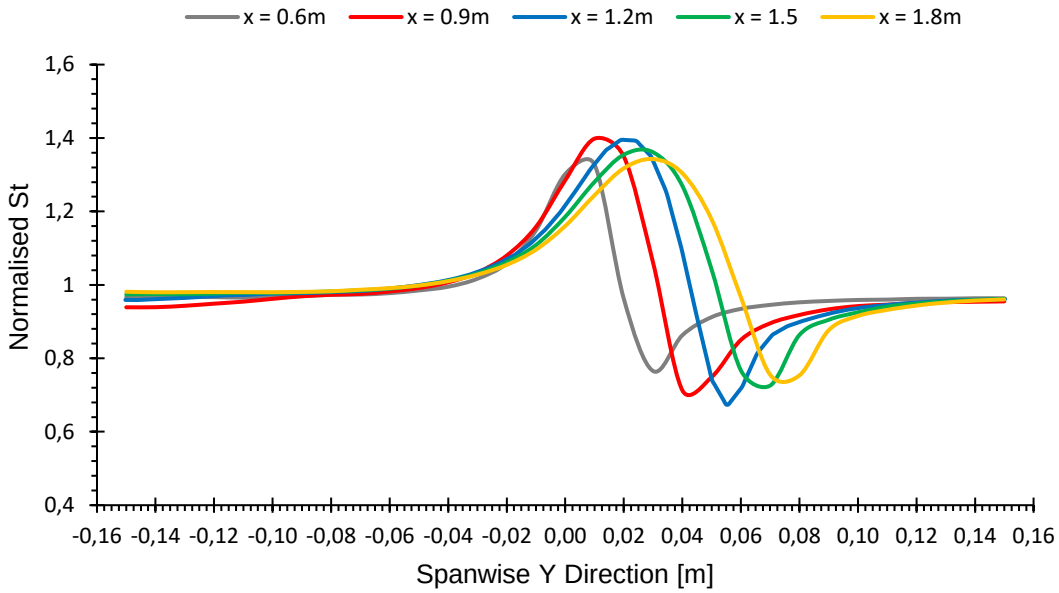

Figure 22. Spanwise Normalised Stanton Number

Figure 23 shows the variation of the surface Nusselt number (Nu) over the bottom surface of the flow channel. The contour plot shows 3 areas of interest; region I, formed under around the vortex generator, region II, formed under the inflow region, and region III, formed under the outflow region. The Nusselt number is highest at region I where the vortex is being generated due to relatively high shear stresses caused by the interaction between the upstream fluid boundary layer and the vortex generator. The sudden rise in the Nusselt number is most likely due to the presence of high shear stress at the region. Region II presents with higher heat transfer as opposed to region III where the heat transfer is less that the empty domain case. This confirms the arguments made by Wu et al. [10], Eibeck and Eaton [8], and Deb et al. [11] that heat transfer enhancement is mainly present in the downwash (inflow) region.

Figure 24 shows the plot for the maximum normalised Nusselt number along the length of the flow channel. The Nusselt number was determined by taking the maximum data points for the Nusselt number and was normalised with the Nusselt number of the empty domain. From the chart the highest peak is in region I (at x= 0.5m, where $Nu \approx 1.8Nu_0$). The Nusselt number abruptly drops to a minimum at $x = 0.58m$ ($Nu \approx 1.4Nu_0$) after which it rises gradually to a peak at $x = 0.75m$ ($Nu \approx 1.5Nu_0$). At the region $0.75m < x < 0.9m$ there is a slight drop in the heat transfer, but there is recovery at $x = 0.9m$, after which the Nusselt number drops exponentially. The Nusselt appears to decrease linearly, because the vortices are weak, however from literature (see figure 3) this is not the case. What is expected is an exponential decrease in the streamwise direction.

At the region I ($0.58m < x < 0.75m$) the vortex leaving the trailing edge of the vortex generator is small compared to the main vortex at x = 0.75m. The core vorticity is higher at $x = 0.58m$ ($\omega = 1.6$) when comparing it to the main vortex core vorticity at $x = 0.75m$ ($\omega = 0.8$). The vortex area at $\omega = 0.1$ is approximately 2.8 cm^2 and 5.06 cm^2 for the main vortices at $x = 0.58m$ and 0.75m respectively. The position of the vortex at $x = 0.58m$ sits higher ($z \approx 1.58cm$) than the vortex at $x = 0.75m$ ($z \approx 1.4m$). The result of the vortex size being smaller and that the core lies higher than the vortex at $x = 0.75m$ results in a thicker boundary layer at this point which results in a lower heat transfer. Refer to figure 50 in Appendix A3, to observe the change in vortex size and position. The heat transfer also decreases exponentially from its peak of $Nu/Nu_0 = 1.37$ ($x = 0.75m$) to 1.17 near the outlet (x =1.98m). The vorticity (figure 20) does not follow the same trend as the heat transfer at region $0.53m < x < 0.9m$. The vorticity may not be directly correlated to the heat transfer, but the vorticity has an influence when considering the size and strength of the vortex. The location of the vortex may play a role in inhibiting the heat transfer, but this is also influenced by the strength of the vortex.

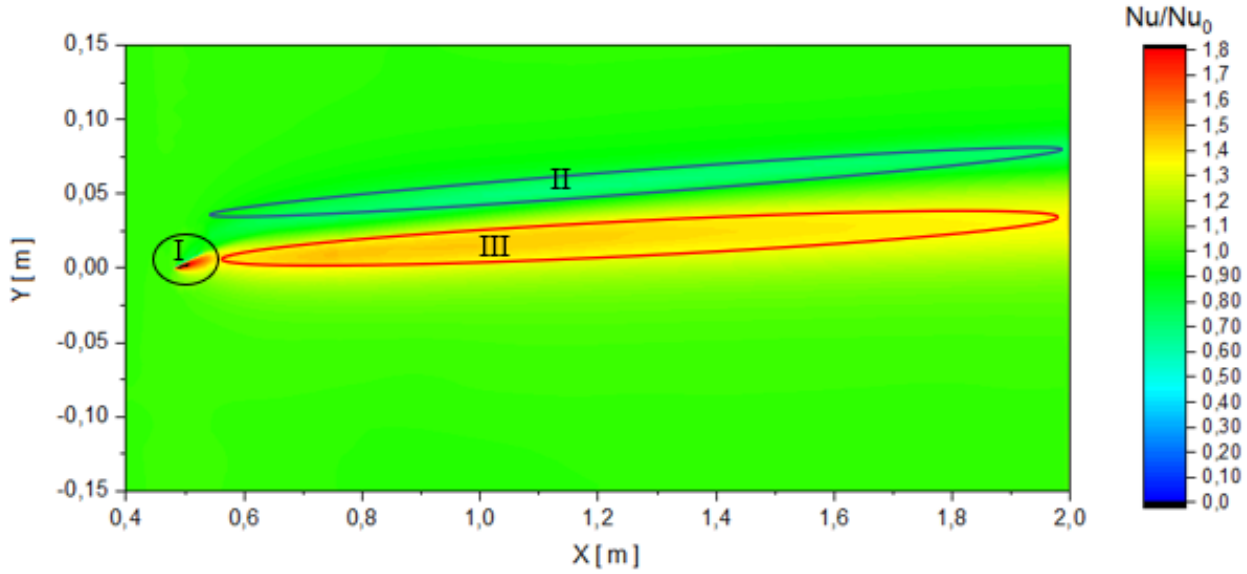

Figure 23. Contour Plot of the Normalised Nusselt Number

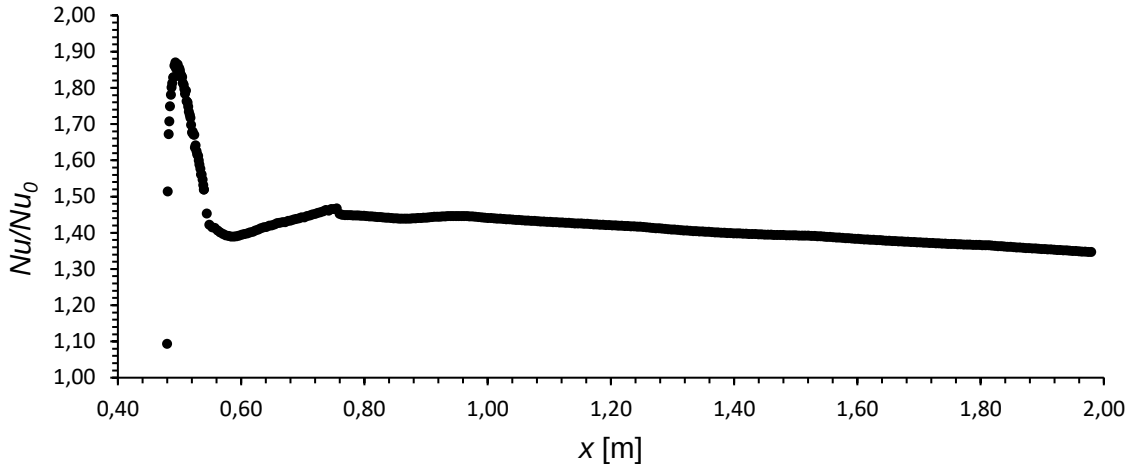

Figure 24. Streamwise Maximum Nusselt Number

The movement of the main vortex from the trailing edge of the vortex generator is such that it moves downward and outward at 0.58m < *x* < 0.75m but moves gradually upwards and outwards as the vortex moves further downstream. This was the same observations found in experimental data by Wu et al. [10], and Cutler and Bradshaw [41]. Wu et al. [10] attributes the outward movement of the vortex as being caused by the near-surface vorticity and the upward movement is caused by vortex rebound.

5.1.4 Boundary Layer of Flow Past Vortex Generator

Figure 25 shows the deformation of the boundary layer at the inflow (at *y* = 2.5cm) and outflow region (at *y* = 5.5cm) at *x* = 1.2m. The inflow region corresponds to the region of maximum Stanton number, while the outflow region corresponds to the region of minimum Stanton number. The velocity profile shows that the boundary layer thickness for both the inflow and outflow region are similar. The boundary layer is 3.5% thicker for the inflow region compared to the outflow boundary layer. Both inflow and outflow boundary layers are thicker at $0.99U_\infty$ when compared to the empty flow channel boundary layer at the same location. There is a 46% increase in the boundary layer, for the inflow and outflow region, at the location after the vortex generator is introduced. However, this is due to the secondary flow created by the vortex generator.

The boundary layer for both inflow and outflow appears to have a kink in the chart. This kink appears at *z* = 6mm (inflow) and *z* = 9mm(outflow). This is the thinned-out boundary layer referred to when referring to boundary layer thinning, which is one of the mechanisms for heat transfer enhancement. This can be seen at around *z* = 6mm, where the velocity is $0.97U_\infty$. At this thickness the velocity, for the inflow boundary layer, is higher than the empty domain ($U = 0.81U_\infty$) and the outflow region ($U = 0.7U_\infty$).

Wu et al. [10] observes the same trend for the velocity profile and argues that this is the reason why there is high heat transfer at the inflow region and low heat transfer at the outflow region. This could possibly be due to the shear stress applied to the wall that is increased due to the increase in the velocity gradient near the heat transfer surface (see figure 25 at region 0 < Z < 0.01). Near the surface of the flow channel the outflow velocity gradient is shallower than the empty domain velocity gradient, while the inflow velocity gradient appears steeper. A steeper velocity gradient implies that

the velocity gradient is of a higher value and this implies an increase in the shear stress at the surface. This is because wall shear stress is directly proportional to the velocity gradient (since $\tau = \mu \frac{du}{dz}$).

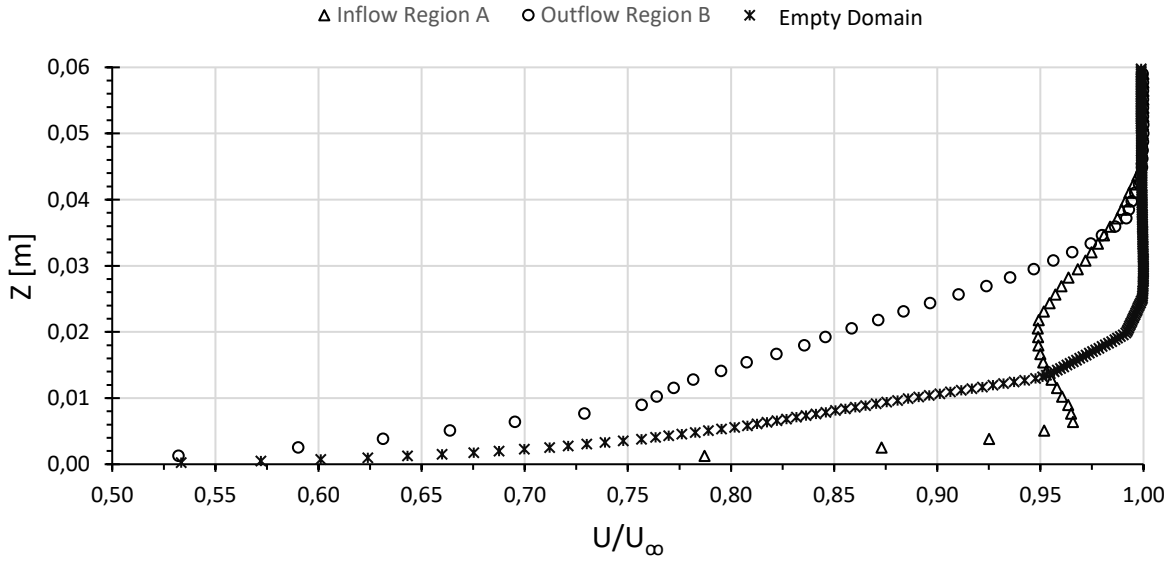

Figure 25. Boundary Layer at x = 1.2m

5.1.5 Wall Shear Stress

Figure 26 shows the variation of the wall shear stress along the heated surface between the trailing edge of the vortex generator (x = 0.53m) and the outlet of the domain (*x* = 2m). The wall shear stress was calculated from the Fluent software and shows the magnitude of the shear stress at the wall (this includes τ_{xz},τ_{yz}, and τ_{xy}). The shear stress ($\boldsymbol{\tau}$) is not high ($0.2 < \boldsymbol{\tau} < 1.2$ Pa), hence why the x-axis range was used to illustrate the regions of high shear with more clarity. The wall shear contour plot shows that the shear stress is higher at the downwash region (under the main vortex) and lowest at the upwash region (under the induced vortex). The contour plot also shows that at region $0.6\text{m} < x < 0.8\text{m}$, the shear stress is higher than the shear stress leaving the trailing edge of the vortex generator, which is expected to be higher at that region ($0.53\text{m} < x < 0.6\text{m}$). Figure 27 shows the spanwise plot of the wall shear stress at *x* = 1.2m. The curve of the shear stress follows the same wave-like trend as the Stanton number curve. The peak and trough are at the same *y* locations (*y* = 2.5cm and *y* = 5.5cm, respectively). Comparing figure 27 to the velocity profile plot (figure 25), it is possible that the near wall velocities raise the velocity gradient which increases the shear stresses at the wall, and this would in turn raise the heat transfer at the region. Splitting the shear stress into its *x* and *y* components, we get the contour plots shown in figure 28 and 29.

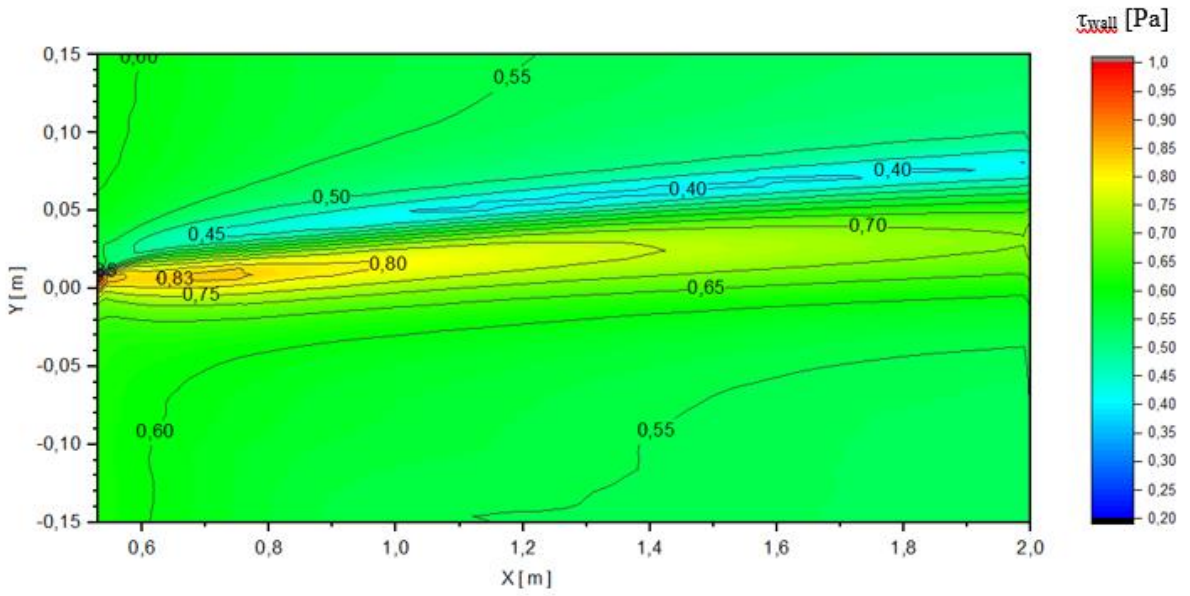

Figure 26. Wall Shear Stress Contour Plot [Pa]

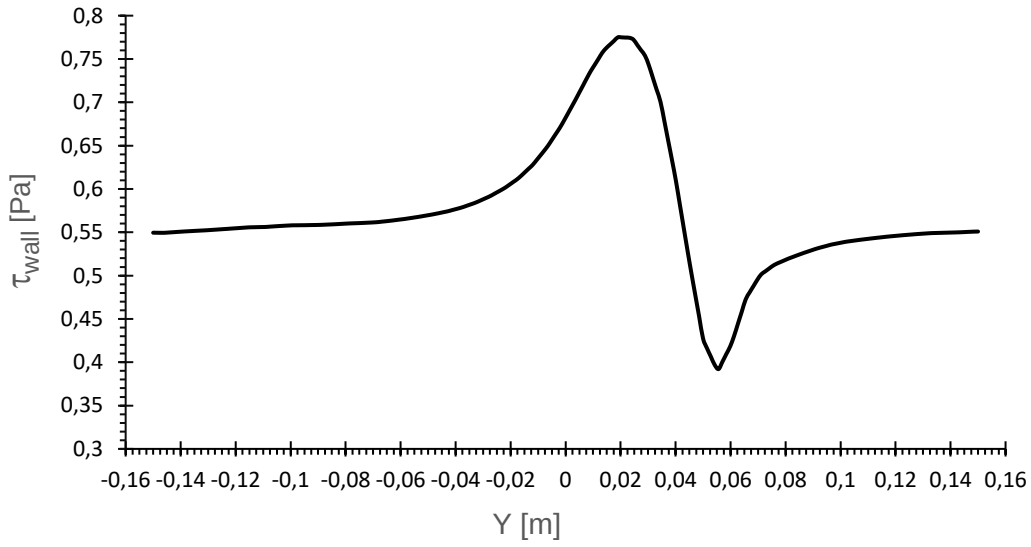

Figure 27. Wall Shear Stress at x = 1.2m

Figure 28 and 29 shows that the introduction of vortex induces a shear stress component in the X (τ_{xz}) and Y (τ_{yz}) direction. In the empty domain, the heat transfer surface only experienced shear stress in the *x* direction (τ_{xz} = 0.6 at 0.35m < *x* < 0.58m), i.e., the τ_{yz} is very small or zero. With the vortex generator present, the shear stress downstream of the vortex generator has a τ_{xz} that was higher at the main vortex region, where the heat transfer is dominant. At the region of the induced vortex, the *x* component of shear stress was the lowest. The *y* component of shear stress, downstream of the vortex generator, was higher at the region of the main vortex. Compared to the empty domain, the shear stress for both τ_{xz} and τ_{yz} increased after the vortex generator was introduced, but only around the region where the vortices are present. This shows that the vortices are increasing the shear stress behind the vortex generator. The higher shear stress under downwash region shows that there is

higher transfer of energy into the wall of the domain. The increase in τ_{xz} was most probably due to the circulation or vorticity strength of the main vortex. τ_{yz} increases around the main longitudinal vortex region, but rapidly decreases downstream of the vortex generator.

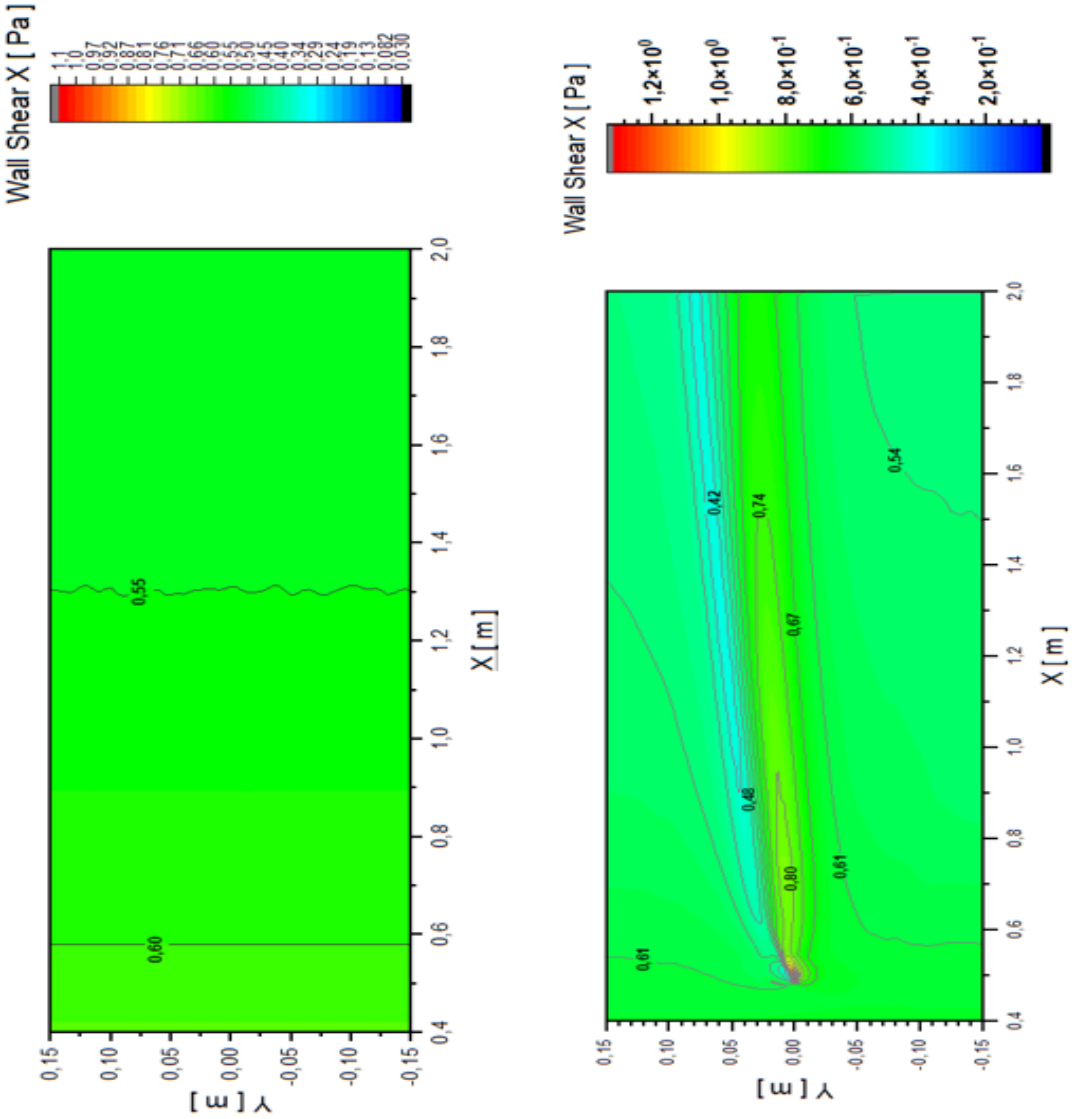

Figure 28. Contour Plot of τ_{xz} Empty Domain vs Vortex Generator Domain

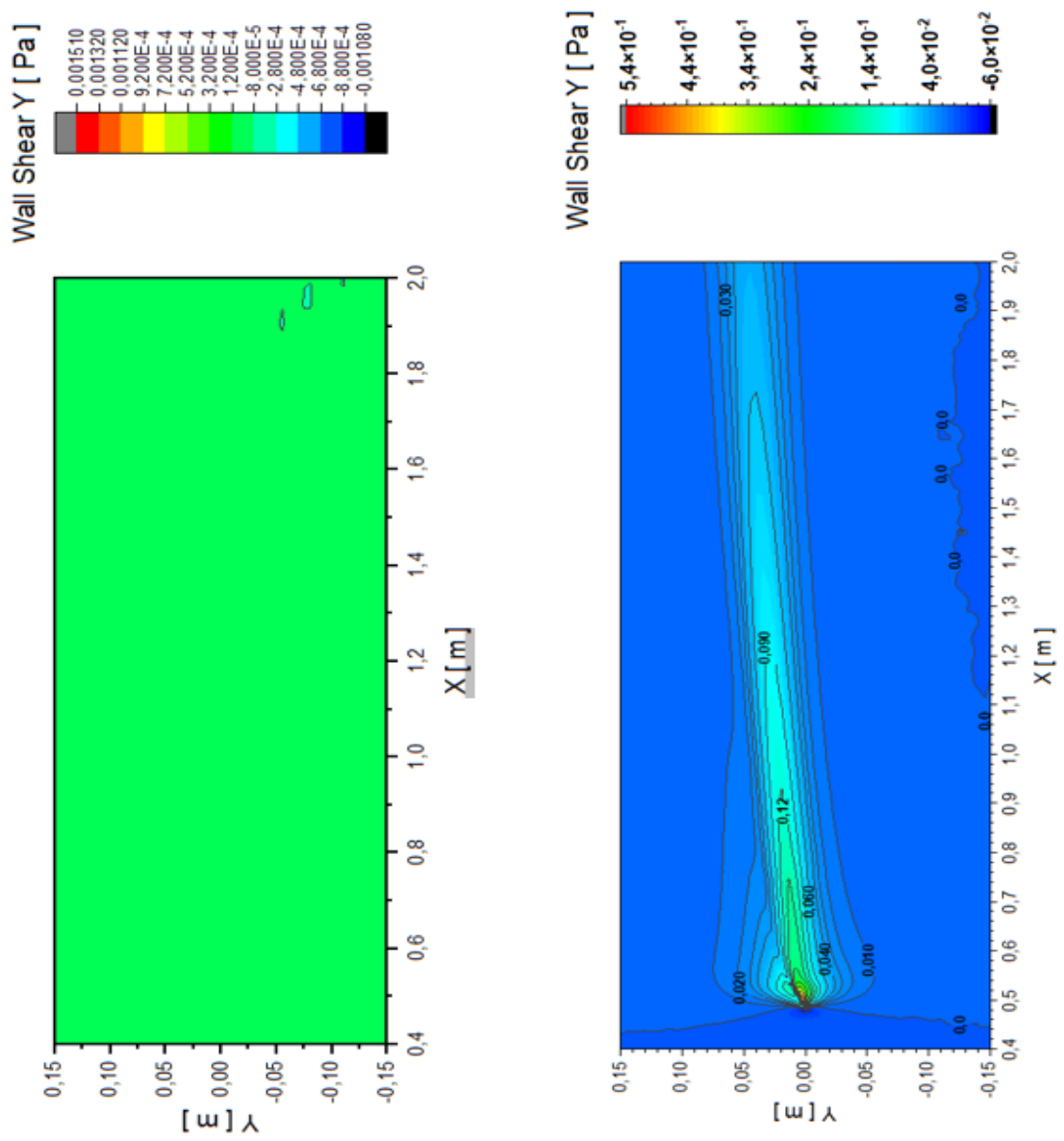

Figure 29. Contour Plot of τ_{yz} Empty Domain vs Vortex Generator Domain

Research by Ge et al. [13], shows that streamwise vortices correlates to high streamwise shear stress (τ_{xz}) at the downwash region, while the lowest τ_{xz} is formed at the upwash region of the vortex. Ge et al. [13] refers to the spanwise shear stress (τ_{yz}) as the footprint of the overhead vortical structures in the spanwise direction. From the τ_{yz} contour plot in figure 29, we can see that the spanwise shear stress(τ_{yz}) forms a footprint of the main vortex on the heat transfer surface. The shear stress contour plots from Ge et al. [13] shows that a vortex rotating counterclockwise imposes a shear stress in the positive spanwise direction. This does tie in with what can be seen in Ge et al. [13], but the focus of this research is the effect of vortices on heat transfer. From the τ_{yz} contour plot, we can see that the τ_{yz} shear stress is in the positive direction while the vorticity is counterclockwise which is what is similarly found in Ge et al.'s [13] research. With Ge et al. [13] the downwash motion of the vortex forms the majority of τ_{yz}. From figure 28 we can see that the main vortex (downwash vortex) contributes to the bulk of the τ_{yz} on the domain wall.

Vorticity and shear stress are related due to their shared proportionality to velocity gradient, although vorticity is the subtraction of two velocity gradients while shear stress is the addition of two velocity gradients. If we look at the streamwise vorticity equation 2, and the shear stress component τ_{yz} equation 13, we see that the equations both a function of $\partial w/\partial y$ and $\partial v/\partial z$. This shows that the streamwise vorticity has an influence on the shear stress τ_{yz}. For example, if $\partial w/\partial y$ increases, vorticity and τ_{yz} both increases. However, if $\partial v/\partial z > \partial w/\partial y$ vorticity changes direction, but the shear stress still increases in the same direction. As $\partial v/\partial z$ gets significantly larger than $\partial w/\partial y$, the vorticity remains in negative rotation, but increases in strength, while the shear stress increases. Looking at the τ_{yz}, we can see that at the region $0.5\text{m} < x < 0.7\text{m}$ the spanwise shear stress under the induced vortex is larger than the vortex absent surroundings. This is due to the condition that $\partial v/\partial z > \partial w/\partial y$.

The streamwise shear stress is dependent on the velocity gradient $\partial u/\partial z$, which is due to the streamwise velocity u. Hence, if the streamwise velocity increases, $\partial u/\partial z$ also increases leading to an increase in shear stress τ_{xz}. Spanwise vorticity and velocity gradient $\partial w/\partial x$ may have influenced the streamwise shear stress, although these quantities are very small in comparison to streamwise vorticity and $\partial u/\partial z$. The converse is true if the velocity is decreased. Referring to figure 18, we see that at region B (the induced vortex or upwash region) the velocity is lower than the region A (main vortex or downwash region of the vortex). From the contour plot of streamwise shear stress τ_{xz}, we see that the region of low shear stress τ_{xz} corresponds to region B where the velocity is decreased. The region of high τ_{xz} corresponds to the region A where the velocity is increased. The introduction of the vortex generator caused the increase of streamwise velocity, which led to the increase in streamwise shear stress τ_{xz}. This is a contrast to the empty domain, where the shear stress was consistent throughout the domain.

Looking at the overall wall shear stress contour plot (figure 28 and 29), we see that the streamwise shear stress is dominant over the spanwise shear stress and this shows that the velocity gradient $\partial u/\partial z$ was the dominating quantity that increases the overall wall shear stress. This is due to that fact that the resulting vortex is not a strong vortex, hence why the spanwise shear stress τ_{yz} was not strong enough.

The streamwise shear stress resembles the Nusselt number contour plot (figure 23) on the heat transfer surface. The region of the minimum heat transfer (region II) corresponds to the minimum shear stress region, which is under the induced vortex (upwash region). The region of maximum heat transfer (region III) corresponds to the maximum shear stress region, which is under the main vortex (downwash region). This shows that the heat transfer is impacted by the shear stress on the wall of the heat transfer surface.

5.1.6 Summary

In this sub-section, the flow feature, the changes in temperature, heat transfer, and shear stresses are discussed. We find that there are two counter-rotating vortices developed by the vortex generator. The main vortex is formed by the downwash flow, while an induced vortex is formed by the slow moving upwash flow left behind by the main vortex. The boundary layer formed by the downwash of the main vortex is thinner than the boundary layer at the upwash region and the boundary layer of the empty domain. This why the heat transfer under the main vortex is higher than the heat transfer under the upwash region. The upwash region also conveys hot air, circulated by the main vortex, and this forms a high temperature zone caused by the mixing of hot air into the boundary layer. This is confirmed by the Stanton number plots and the Nusselt number contour plot in figure 22 and 23.

The boundary layer also raises awareness on the influence of shear stress on heat transfer and how the vortices influence the shear stress. From the wall shear stress plot (figure 27), we see that under the downwash region the shear stress peaks while under the upwash region the shear stress drops to a minimum. The shear stress footprint shown in figure 26 resembles the footprint of the Nusselt number in figure 23. This shows that the shear stress is responsible for the heat transfer on the wall and this

shear stress is caused by the presence of the vortices. The increase in the streamwise shear stress τ_{xz} is due to the increase in the streamwise velocity, while the spanwise shear stress τ_{yz} was influenced by the streamwise vorticity. Another parameter that influences the shear stress is the circulation or vorticity strength as this is a cumulative measure of vorticity.

Looking at the streamwise trends of the vorticity, and heat transfer plots (figure 20 and 24) it can be seen that the vorticity has no influence on the heat transfer on its own. However, it is believed that the circulation or vorticity strength (which are a function of vorticity) may have a direct influence on the heat transfer. This will be discussed in the next section.

Lastly the limitations experienced during data acquisition was caused by the effects of the dissipation rate equation of the k - ε model are highlighted in the visualisation of the induced vortex and the rapid drop in vorticity at 0.53m < x < 0.9m. While the outline of the induced vortex is visible, there are key features that are not shown due to dissipation rate of the turbulence model. It is therefore advisable to do further research on the induced vortex using a more sophisticated turbulence model like RSM or LES.

5.2 Vorticity Flux, Circulation and Heat Transfer

Two parameters are used to describe the vortex strength: the circulation, and the vorticity flux. The circulation describes the strength of the main vortex, while the vorticity flux is used to describe the spanwise strength of both the main vortex and the induced vortex. The parameters are related to the heat transfer within the flow channel to determine how the vorticity flux and the circulation influences the heat transfer. To calculate the vorticity flux and circulation, the double integral was taken at 20 different locations in the domain. The integration was performed with OriginPro 2019 Software, using the 2D Integration Gadget at the 20 locations in the domain. To check that the output of the gadget is accurate, a hand calculation of the integration was performed, and it showed that the result deviated by 6.7%. However, in the hand calculation, the contours were assumed to be perfect ellipses and, in the contour, plot the shape of the main vortex is not a perfect ellipse. Therefore, it was deemed more accurate to calculate the integration around the main vortex using the integration tool. The hand calculation was a validation step to make sure that the integration produces results that are within a reasonable range.

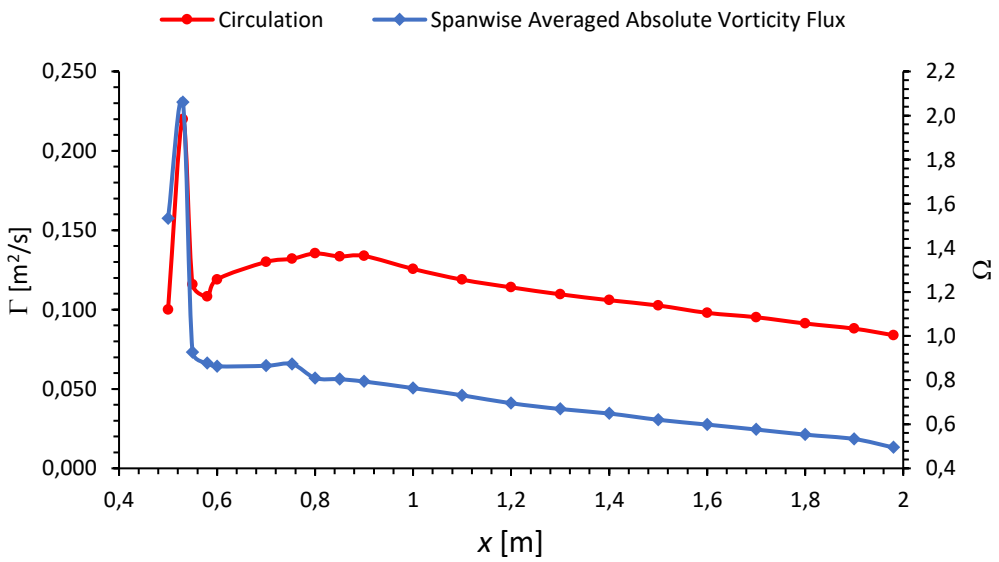

Figure 30. Comparison of Main Vortex Circulation (Γ) and Spanwise Averaged Absolute Vorticity Flux (Ω)

Figure 30 shows the streamwise circulation (Γ_{main}) of the main vortex and spanwise averaged vorticity flux (Ω). From the circulation curve, the circulation peaks at x = 0.53m at 0.22m^2/s, at the trailing edge of the vortex generator where the shape of the vortex is defined. Vorticity is high at this region as expected; however, it is higher between region 0.48m < x < 0.53m where the vortex is still being generated by the vortex generator. The circulation is not high at this region because the vortex is relatively small compared to the vortex at x = 0.53m. The circulation drops to a minimum around region 0.58m at 0.108m^2/s, at the same region where the heat transfer or Nusselt number (see figure 24) drops to a minimum. The next peak is at 0.8m at 0.135 m^2/s, which differs from the Nusselt number at the same region (x = 0.8m), which is trending downward. This difference is caused by the induced vortex becoming stronger at the location. This can be seen by the spanwise averaged absolute vorticity flux at the same location where the Ω curve drops to 0.809, which is follows the same trend as the Nusselt number from figure 24. This shows that the induced vortex has some influence on the heat transfer. Referring to the circulation curve, there is a slight uptrend at x = 0.85m, which is similar to what can be seen in the heat transfer curve (figure 24) at region 0.85m < x < 0.95m.

Further downstream of this region, we see a somewhat shallow downtrend in both the circulation and the vorticity flux, which is what can be seen with the Nusselt number curve at x > 0.95m. Eibeck and Eaton [8] also observed a slight decay in the circulation from x > 0.93m from the entrance of the wind tunnel, which is what can be seen in this study. However, looking at figure 15 in the validation section, we see that the slope of the experimental circulation curve, at 90cm < x < 120cm, is shallower than the computational curve at the location. Technically it is expected of the vortex to reach a point where the circulation remains constant. Eibeck and Eaton [8] do not show their circulation beyond 1.8m, but from figure 15 we can see that there will come a point where the circulation will eventually become constant. For the computational model the circulation continues dropping. This is caused by the dissipation rate (ε) equation of the k - ε model. The ε equation tends to exaggerate the dissipation of eddy flows and can lead to circulation trends as seen above. Even when observing the Ω at 1.9m < x < 2m the slope drops even further and since k - ε models do not particularly model surrounding eddy flow all to perfectly you can expect this kind of circulation dissipation as in figure 30.

From figure 30, the circulation curve shows how the strength of the main vortex has an overall influence on heat transfer enhancement, while the Ω curve shows us how the induced vortex could interfere with the heat transfer enhancement to some extent. From the graph at region 0.53m < x < 0.9m, comparing the Ω curve to the circulation curve, we can see how the induced vortex can affect the overall strength of the main vortex in transferring energy into the boundary layer. Overall, the fact that the trend of the circulation as well as the vorticity flux curve is similar to the trend from the streamwise maximum Nusselt number curve shows that the strength, which incorporates the vorticity and the size of the vortex, has a major influence on the overall heat transfer enhancement.

Lenmenand et al. [12] show a similar trend their computational study in determining the relationship between vorticity density (vorticity flux) and heat transfer. The difference is that a trapezoidal wing is used instead of a delta winglet vortex generator, and the vorticity flux is inclusive of the vortices around the entire domain. Hence, they found that the vorticity flux was highest at 1tab height upstream of the trailing edge of the vortex generator, which was attributed to the horseshoe vortex produced upstream of the vortex generator. In the current study, the vorticity flux only considers the vorticity flux of the main vortex and the induced vortex, avoiding any corner vortices created by the walls of the domain, since the vortices generated by the vortex generator was the main interest for the study. The Nusselt number under the main vortex was considered as opposed to the spanwise averaged Nusselt number, since the vortex generated is generally weak and the heat transfer within the entire domain is not entirely affected by the presence of the vortex. The bulk of the heat transfer is localised under the main vortex, and this is the region of interest for the research.

In summary, the circulation correlates closely to the heat transfer as discussed above, but from the vorticity flux curve it can be seen that the induced vortex also plays some role in influencing the heat transfer. Overall, the circulation is related to the strength of the vortex and this in turn influences the shear stress, because the strong vortices apply higher shear stresses on the boundary layer. Since the shear stress is increased by the circulation, the heat transfer should also increase under the region. Therefore, the circulation of the vortex influences the heat transfer in the domain.

5.3 Helicity and Heat Transfer

Helicity is often linked to the strength of the linkage of the vortex tube. The helicity of the main vortex and the induced vortex drop as the flow moves downstream of the vortex generator. As the helicity drops, its more prone to dissipate and lose kinetic energy. This should result in a drop in the heat transfer, which is what is observed from the study as the vortex continues to move downstream.

Figure 31 shows the contour plots for the nondimensional Helicity density at x = 0.6m to 1.5m. The Helicity density was nondimensionalised by multiplying the helicity by the height of the vortex generator and dividing by the square of the freestream velocity (U_∞).

From the contour plot (Figure 31) for helicity density at x = 1.2m, the helicity at the region of high heat transfer is positive (H > 0). Meanwhile the helicity density at the region of low heat transfer has a negative helicity (H < 0). The main vortex has positive helicity, while the induced vortex consists of negative helicity. The only difference between the vorticity and the helicity contours is that the region under the main vortex where the vorticity is supposed to be negative, the helicity density contour is positive. This means that the boundary layer under main vortex is moving in the same direction and there is exchange of heat energy between the two regions.

Observing the evolution of the helicity at 0.6m< x <1.5m from figure 31, we see that the helicity plot, at x = 0.6m, shows the main vortex above what should be another induced vortex I2(not to be confused with the counter-rotating induced vortex which is referred to as the outflow region). Induced vortex I2 moves with the same positive sign indicating that they move in the same rotational direction. I2 does dissipate completely as the main vortex moves to x = 0.9m. Take note that at the location x = 0.6m the vortex is still under development. At x = 0.9m the helicity of the main vortex extends to the boundary layer almost interacting with the surface. This shows that the main vortex could be conveying heat from the surface into the vortex. At x = 1.2m the helicity of the main vortex's outer contour at the surface gets narrow indicating dissipation of the main vortex. This weakening of the vortex could be artificially caused by the dissipation of the turbulence model, but can explain the downstream drop in the streamwise Nusselt number (see figure 24).

At location x = 0.9m to x = 1.5m, we can see negative helicity contour depicting the induced vortex on the upwash region (0.04m < y < 0.06m). This suggests that the induced vortex is moving in upward direction from the surface. This could explain the presence of the lower shear stress under induced vortex. Due to the opposing direction of the induced vortex creates a τ_{xz} shear stress in the opposite direction of flow causing the overall shear in this region to drop.

Figure 31 shows that the helicity of the main vortex is using it's angular momentum to pull hot air from the heat transfer surface into the main vortex. The helicity also depicts the mechanism of boundary layer mixing usually referred to when considering vortices and heat transfer. The 0.01 contour gets narrower as the vortex moves from x = 0.9m to x = 1.5m, and the main vortex interacts less with the surface. This should result in a weakening of boundary layer mixing mechanism and result in a drop in heat transfer. Figure 31 also shows that the vortex is losing kinetic energy and will eventually lift away from the surface and dissipate, while at the same time the heat transfer drops.

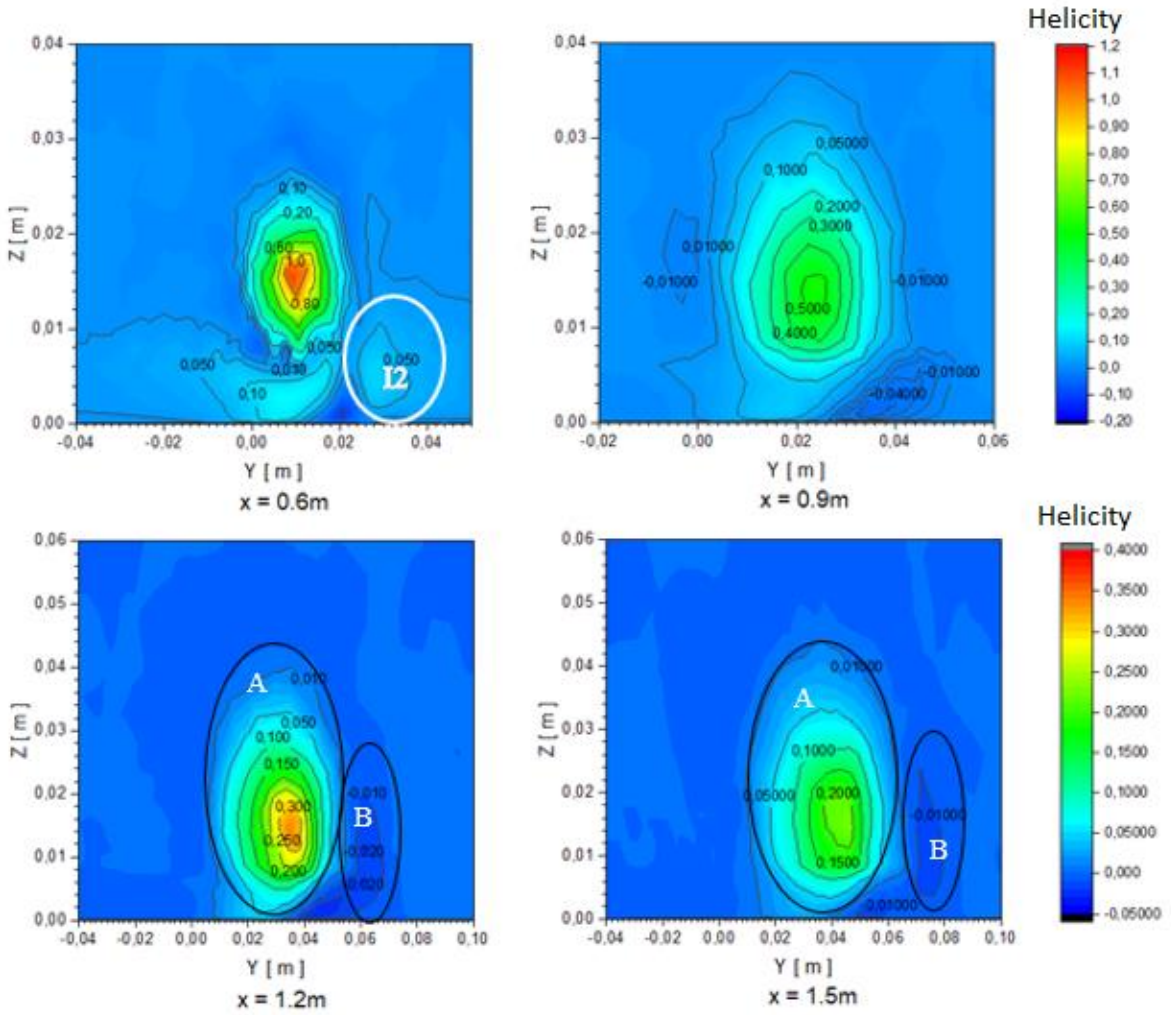

Figure 31. Nondimensional Helicity at x = 0.6m, 0.9m, 1.2m, and 1.5m

Taking a closer look at the estimated area integral under helicity plot or helicity flux, from figure 32, we see a similar trend to the streamwise circulation (see figure 30) along the length of the flow channel. There is a peak at x = 0.53m, with helicity flux at 4.3m^3/s^2, which drops to a minimum of 1.7m^3/s^2 at x = 0.58m. The second peak occurs at around x = 0.8m (2.16m^3/s^2) and the same kink between 0.8m and 0.9m can be seen in the helicity flux, albeit to as smaller size (at x = 0.85m, helicity flux = 2.16; and at x = 0.9m, helicity flux = 2.16). At x > 0.9m the helicity flux decreases in an almost linear trend like the circulation and heat transfer. Expanding on the relationship between circulation and helicity flux, we observe that the trends are the same, this is because the circulation and helicity flux are both functions of vorticity. The only difference is that the helicity flux is amplified by the velocity because of $Helicity = velocity \cdot vorticity$.

Since helicity is a measure of the linkage or knottedness of the vortex lines, we can see that the strength of the linkage of the longitudinal vortex has an influence on the heat transfer. Therefore, the dissipation of the vortex must be reduced to have efficient heat transfer enhancement. Within the results, there is the problem of the ε equation (in the turbulence model) overestimating the dissipation of the vortex. Compared to what may happen in a real scenario, the artificial dissipation rate may have over predicted the drop in helicity flux in the computational model.

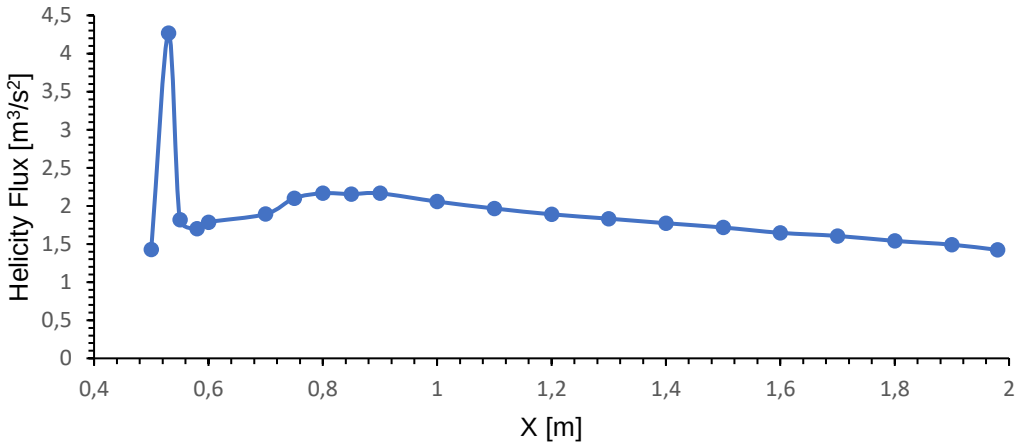

Figure 32. Streamwise Helicity Flux for Main Vortex

Often the helicity will be related with the cascade or non-linear energy. Wu and Lilly [42], Moffatt [43], and Wallace et al. [44], have defined a term called the Lamb vector, which is defined by **ω** x **u**, and has an anticorrelation with the helicity of the vortex. Wu and Lilly [42] have stated that the Lamb vector is the dominant quantity that represents the inertia force in rotation form in fluid flow. The Lamb vector for x = 1.2m is shown in figure 33. From the contour plots the Lamb vector is highest at the region under the main vortex ($-0.03 < y < 0.04$) where there is high heat transfer. This gradually decreases along the path of the upwash region ($0.04 < y < 0.06$), where the heat transfer is lowest. The red zone of the Lamb vector can be seen under the region where the boundary layer is at its thinnest. Along the induced vortex (at $y > 0.06$m) the red band contour is visible, but thin in comparison to the main vortex region. This shows that the heat energy transfer is increasing to a small extent. This could explain why the Stanton curve rises between $0.06\text{m} < y < 0.12\text{m}$ (see figure 22). Along the height (z-axis) of the flow channel, the bulk of the Lamb vector is concentrated around the induced vortex and weak bands can be found around the outer contours of the main vortex (see area M in figure 33). The contours around the induced vortex are relatively stronger when compared to that of the main vortex. This indicates the transfer of hot air from the downwash region to the upwash region. The heat being removed from the region of high heat transfer is transferred to the induced vortex as speculated by Wu et al. [10].

Looking gradual rise of the red contour at region between $-0.05 < y < 0.03$ (figure 33) suggests that there is some form of energy from the main vortex that is facilitating the heat of heat away from the heat transfer surface to the upwash region. This could imply that the kinetic energy of the main vortex is aiding the boundary layer mixing between the main vortex and the viscous boundary layer. Hence the main vortex is responsible for the heat transfer enhancement whereas the induced vortex carries the hot air from the upwash caused by the main vortex.

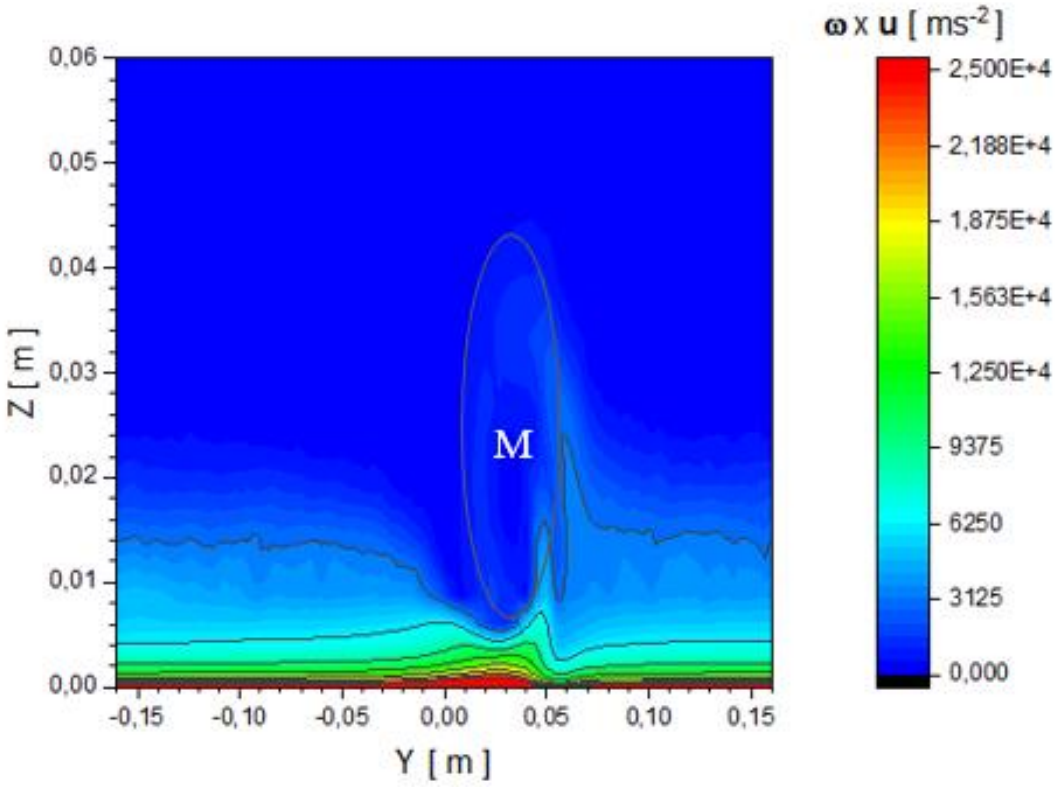

Figure 33. Lamb Vector (nonlinear energy transfer) Contour Plot

From figure 33, at region M the lamb vector is dissipating along the core of the main vortex suggesting convection between the main vortex and the hot air from the heat transfer surface. Figure 34 shows the fluid temperature contour at x = 1.2m. The variation of temperature along the near wall surface at region C, under the induced vortex (0.04m < y < 0.12m), has higher temperature at the surface, and a peak at y = 0.06m can be seen at this region. Observing the movement of the heat from region C, the heat is forced into the region by the rotation of the main vortex. This can be seen in figure 17, in the velocity vector plot. The red arrows, of the vector plot, forces the cold air into the boundary layer resulting in convection. Other observations from the above figure 34 shows that the upwash region is conveying the hot into the core of the main vortex, while in the induced vortex (vortex formed by the upwash region) drops the temperature of the fluid. At the downwash region the fluid temperature is the lowest at this region, which is expected. The heat from the bottom surface is transferred to the fluid and pushed to the upwash region and cools down along the core of the main vortex, as shown in figure 33.

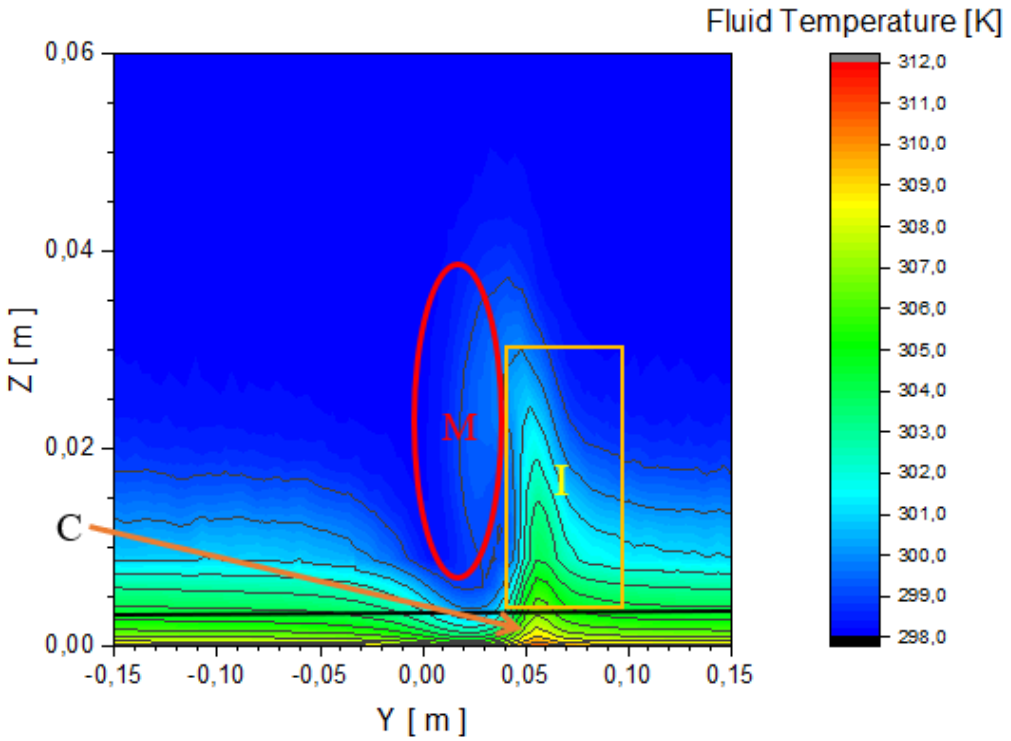

Figure 34. Fluid Temperature Contour at x = 1.2m

In summary the helicity is the linkage strength of the vortex and from observing the evolution of the helicity contours, we can see that this linkage weakening as the vortex moves downstream. Likewise, the heat transfer is also drop at the same rate as the trend in figure 32. This weakening of the linkage strength is also influenced by the dissipate rate equation of the k - ε turbulence model. However, even with all the artificial dissipation we can deduce that the strength of the vortex linkage plays a role in the decrease of the heat transfer by observing the low helicity density of the induced vortex, where the heat transfer is the lowest. The helicity of main vortex is positive, while the helicity of induced vortex is negative. The helicity also indicates the influence of kinetic energy of the main vortex to the boundary layer of the heat transfer surface. From the contour plots in figure 31, we see that the main vortex extends to the heat transfer surface, attaching itself to the boundary layer. This shows that there is boundary mixing between the main vortex and the boundary layer of the heat transfer surface. Hence there is convective heat transfer between the surface and the main vortex. Figure 33 confirms that the main vortex aids the transfer of heat away from the heated surface, while at the same time the upwash surrounding the main vortex conveys the newly hot air into the induced vortex. The dissipation of the lamb vector at the core of the main vortex could suggest that the hot air from the surface is undergoing convection by the cool air in the main vortex. Figure 34 shows the induced vortex carrying the heated air while the main vortex conveys the cool air, which is transferred to the wall surface under the vortex.

6. Conclusion

In this research vortices were generated by a delta winglet vortex generator in a rectangular flow channel. The flow was generated computationally using a steady-state realizable k - ε turbulence model to visualise the vortices in the domain. The freestream velocity and dimensions of the vortex generator were modelled after the Eibeck and Eaton [8] experimental model. Flow parameters like the velocity, vorticity, circulation, and Stanton number were used to validate the computational model with experimental data. The results show that the computational data are within good agreement with the experimental data. The theoretical boundary layer was compared to the computational boundary layer and was found to agree with each-other, with the only maximum deviation found at the Stanton number, which was 20%. Refer to the resulting deviations in table 7 to 9 for more information on the validation of the results. The fact that the circulation follows the same trend (referring to figure 16), also implies that the computational results agreed with the experimental results. There was only a 10% deviation in the case of the circulation (see figure 16). However, the k - ε model vortex dissipates quicker than the experiment vortex. Overall, these deviations are likely caused by the ε (dissipation of turbulence) equation, the resolution of the mesh, or the assumption that turbulence is isotropic.

From the discussion in section 5, two vortices were generated by the delta winglet vortex generator; a main vortex formed by the downwash, and an induced vortex formed by the upwash region. Under the main vortex we see the thinning of the boundary layer and an increase in shear stress, predominantly caused by downwash flow. The increase in the shear stress is caused by the circulation of the vortex. Hence, the stronger the vortex the higher the shear stress on the boundary layer. The rise in the shear stress leads to the increase in heat transfer and drop in temperature. The upward moving side of the induced vortex forms a thick boundary layer, due to the upwash flow. The shear stress in this region is also low, due to the comparatively lower velocity gradient than the downwash region. This leads to drop in heat transfer and rise in temperature under the induced vortex. Thus, the vortices increase heat transfer due to shear force applied to the boundary layer. Spanwise shear stress is related to vorticity, while streamwise shear stress is related to the streamwise velocity. Therefore, Shear stress is a mechanism that facilitates energy transfer from the main vortex to the wall of the heated surface.

From the discussion on circulation (section 5.2), it was found that the parameter exhibits the same trend as the streamwise Nusselt number, hence concluding that the circulation enhances heat transfer. This is because the circulation is a function of the area of the vortex and the vorticity. As such, the circulation is at a minimum at $x = 0.58$m, even though the vorticity is high at the location. The reason for this is because the vortex is small sized at the region. As the vortex moves downstream of the vortex generator ($0.9\text{m} < x < 2\text{m}$), the size of the vortex increases, however the circulation decreases, owing to the low vorticity at the region. The reason why circulation influences heat transfer is because it raises the shear stress at the boundary layer. Since the shear stress is increased by the circulation, the heat transfer should also increase under the region. Therefore, the circulation of the vortex influences the heat transfer in the domain.

The helicity density shows how heat is transferred from the boundary layer of the heat transfer surface to the main vortex. Because the main vortex in the helicity contour plot extends to the heated wall surface, the circulation of the main vortex mixes with the boundary layer of the surface.

By considering the helicity flux, we see that the strength of the linkage of the longitudinal vortex has an influence on the heat transfer. This trend of the Helicity density is similar to the trend of circulation or vorticity flux. Likewise, the trend is also similar to the streamwise Nusselt number trend. Hence, helicity is a parameter that can indicate drop in heat transfer. However, one should note that the dissipation (drop in helicity and circulation) is also caused by the ε equation in the turbulence model. This will be discussed in the recommendations.

The Lamb vector (**ω** x **u**) is often related to the inertial energy transfer and has an inverse correlation to helicity. This parameter describes the inertial energy transfer between the boundary layer and the main vortex, and the dissipation of kinetic energy at the core of the main vortex. Under the main vortex, a high concentration of inertial energy transfer from the heated surface to the wall is present. This suggests convection of heat from the surface to the vortex. Heated air is also transferred to the upwash flow, influenced by the main vortex, into the counter-rotating induced vortex, which weakens the heat transfer enhancement capabilities of the induced vortex.

In summary, we find the following:

1. Circulation is the vortex property that influences heat transfer by applying a shear stress on the boundary layer.
2. Shear stress is the mechanism for which energy is transferred to the heat transfer surface.
3. Helicity indicates convective heat transfer between vortex and heat transfer surface.
4. The helicity indicates the knottidness and dissipation of the vortex tube, and therefore (looking at the streamwise direction), as the helicity drops the heat transfer drops as well.

7. Recommendations

Because of the artificial dissipation term ε, the turbulence model tries to dissipate the vortex quicker than normal. We saw this in the circulation and helicity flux plots. Dissipation also limits perfect visualisation of the induced vortex, making it difficult to measure circulation, and helicity flux of the vortex. However, the results produced were fairly accurate although there may have been some deviation (at most 20%) from the experimental results. It is advised that the domain be simulated with a Reynolds stress model (RSM), or large eddy simulation (LES) model. RSM is especially suited for this type of investigation due to its anisotropic nature and its lower computational expense when compared to the LES model. RSM should also be accompanied by an appropriate mesh or mesh adaptation techniques should be adopted to refine the mesh at area of interest. The LES model does not assume isotropic turbulence, much like the RSM model, and is better suited for vortices. The downside to LES is the computational expense. If the k - ε model were to be revisited for vortex modelling, it is recommended that varying dissipation rates are investigated as well.

It would be advisable to have more experimental data on the effects of circulation, helicity, shear stress, and vorticity on heat transfer as there is scarce experimental research done on the topic. From this more research can be done in this field for varying velocities and Reynolds numbers.

The Lamb vector, while useful, is still a scarcely researched parameter. While it may provide information on inertial energy transfer, it’s still a parameter that need more explanation from a fluid dynamics perspective.

References

1. Johnson, T.R., Joubert, P.N., " *The Influence of Vortex Generators on the Drag and Heat Transfer from a Circular Cylinder Normal to an Airstream*", ASME Journal of Heat Transfer, Melbourne, pp 91 - 99; 1969
2. Fiebig, M., Kallweit, P. , Mitra, N. , Tiggelbeck, S., "*Heat Transfer Enhancement and Drag by Longitudinal Vortex Generators in Channel Flow* ", Experimental Thermal and Fluid Science, New York, pp 103 - 114, 1991
3. Fiebig, M., "*Vortices and Heat Transfer*", ZAMM Journal of Applied Mathematics and Mechanics, pp 1- 17, 1997
4. Fiebig, M., "*Vortices, Generators, and Heat Transfer*", IChemE; vol 76 pp 108 - 123, 1998
5. He. Y. L., Zhang. Y., "*Advances and Outlooks of Heat Transfer Enhancement by Longitudinal Vortex Generators.*", Advance in Heat Transfer Journal vol 44, pp 1 – 46, 2016
6. Song, K. W., Wang L. B., " *Relationship Between Heat Transfer Intensity and Absolute Vorticity Flux Intensity in Flat Tube Bank Fin Channels with Vortex Generators*", Progress in Computational Fluid Dynamics; vol 8, pp 496 - 502; 2008
7. Alawadhi E. M., Bourisli. R. I., "*The Role of Periodic Vortex Shedding in Heat Transfer Enhancement for Transient Pulsatile Flow Inside Wavy Channels.*", World Academy of Science, Engineering and Technology. vol 22, pp 446 – 452, 2008
8. Eibeck, P. A., Eaton, J. K., "*Heat Transfer Effects of a Longitudinal Vortex Embedded in a Turbulent Boundary Layer*", ASME Heat Transfer Journal, pp 16 – 24, 1987
9. Pauley, W. R., Eaton, J. K., "*Experimental Study of the Development of Longitudinal Vortex Pairs Embedded in a Turbulent Boundary Layer*", AIAA Journal, vol 26, no 7, pp 816-822, 1988
10. Wu, H., Ting, D. S-K., Ray, S., "*An experimental study of turbulent flow behind a delta winglet*", Experimental Thermal and Fluid Science 88, pp 46-54, 2017
11. Deb, P., Biswas, G., Mitra, N. K., "*Heat transfer and flow structure in laminar and turbulent flows in a rectangular channel with longitudinal vortices*", Int. J. Heat Mass Transfer, vol 38, No. 13, pp 2427-2444, 1995
12. Lenmenand, T., Habchi, C., Valle, D.D., Peerhossaini, H., "*Vorticity and Convective Heat Transfer Downstream of a Vortex Generator*", International Journal of Thermal Sciences 125, pp 342 – 349, 2018
13. Ge, M-W., Xu, C-X., Cui G-X., "*Detection of near-wall streamwise vortices by measurable information at wall*", Journal of Physics, 318, pp 1-11, 2011
14. Wang, L., Xu, C-X., Zhaoshun, Z., "*Relationship between wall and shear stresses and streamwise vortices*", Journal of Applied Mathematics and Mechanics, 40(3), 2019
15. Choi, H., Moin, P., Kim, J., "*Direct numerical simulation of turbulent flow over riblets.*", Journal of Fluid Mechanics, 255, pp 503-539, 1993
16. Guo, S., Li, W., "*The Effect of Near-Wall Vortices on Wall Shear Stress in Turbulent Boundary Layers*", Science Research Journal 2, pp 190-196, 2010
17. Nirmalkar, N., Chhabra, R. P., Poole, R. J., "*Effect of Shear-Thinning Behaviour on Heat Transfer from a Heated Sphere in Yield-Stress Fluids*", I&EC Research, 52, pp 13490-13504, 2013
18. American Meteorological Society (2012), "*Isotropic Turbulence*", Available at: https://glossary.ametsoc.org/wiki/Isotropic_turbulence [Accessed 10 May 2022]
19. Design Software (2020), "*Choosing the Right Turbulence Model for your CFD Simulation*", Available at: https://www.engineering.com/DesignSoftware/DesignSoftwareArticle…Choosing-the-Right-Turbulence-Model-for-Your-CFD-Simulation.aspx [Accessed 12 March 2020]
20. Armfield S. W., Fletcher, C. A. J., "*Comparison of k - ε and Algebraic Reynolds Stress Models for Swirling Diffuser Flow*", Int. Journal for Numerical Methods in Fluids, vol 9, pp 987-1009, 1989

21. Saqr, M. K., Aly, H. S., Wahid, M. A., Sies, M. M., "*Numerical Simulation of Confined Vortex Flow Using a Modified k - ε Turbulence Model*", CFD Leters, vol 1, pp 87-94, 2009
22. Chenoweth, J. D., York, B., Hosangadi, A., "*Modification of the Standard k - ε for Swirling Flows*", AIAA Journal 2007-5755, pp 1-12, 2007
23. Chenoweth, J. D., York, B., Hosangadi, A., "*Turbulence Model Upgrades for Swirling Flows*", ASME/JSME Fluids Engineering Conference, pp 1-8, 2007
24. Rahman, M., Karim, M., Alim, A., "*Numerical Investigation of Unsteady Flow Past a Circular Cylinder Using 2-D Finite Volume Method*", Journal of Naval Architecture and Marine Engineering 4, pp 27-42, 2007
25. ANSYS Inc., "*Standard k - ε Model*", ANSYS FLUENT Theory Guide v2020 R2, 2020
26. ANSYS Inc., "*Realizable k - ε Model*", ANSYS FLUENT Theory Guide v2020 R2, 2020
27. ANSYS Inc., "*Enhanced wall Treatment ε-Equation (EWT-ε)*", ANSYS FLUENT Theory Guide v2020 R2, 2020
28. ANSYS Inc., "*y^+-insensitive Wall Treatment ω -Equation*", ANSYS FLUENT Theory Guide v2020 R2, 2020
29. ANSYS Inc., "*Spalart Allmaras Model*", ANSYS FLUENT Theory Guide v2020 R2, 2020
30. ANSYS Inc., "*Standard k – ω Model*", ANSYS FLUENT Theory Guide v2020 R2, 2020
31. ANSYS Inc., "*Shear Stress Transport (SST) k - ω Model*", ANSYS FLUENT Theory Guide v2020 R2, 2020
32. Ridluan, A., Eiamsa-ard, S., Promvonge, P., "*Numerical simulation of 3D turbulent isothermal flow in a vortex combustor*", Int Comm in Heat and Mass Transfer 34, pp 860-869, 2007
33. ANSYS Inc., "*Reynold Stress Model*", ANSYS Theory Guide v2021 R2, pp 95-103, 2021
34. Jawarneh, A. M., Vartistas, G. H., "*Reynolds Stress Model in the Prediction of Confined Turbulent Swirling Flows*", Journal of Fluids Engineering, vol 28, pp 1377-1382, 2006
35. White, F. M., "*Fluid Mechanics*", McGraw Hill Int., 6th Edition, pp 468-474, 2008
36. ANSYS Inc., "*Polyhedral Unstructured Mesh Adaption*", ANSYS FLUENT Theory Guide v2021 R2, pp 958-959, 2021
37. Engineers Edge (2022), "*Viscosity of Air, Dynamic and Kinematic*", Available at: https://www.engineersedge.com/physics/viscosity_of_air_dynamic_and_kinematic_14483.htm [Accessed 20 May 2022]
38. ANSYS Inc., "*Scalable Wall Functions*", ANSYS FLUENT Theory Guide v2022 R1, pp139, 2022
39. ANSYS Inc., "*Custom Field Function Calculator Dialog Box*" ANSYS FLUENT Users' Guide v2022 R1, pp 4684- 4686, 2022
40. Biswas, G., Torii, K., Fujii, D., Nishino, K., "*Numerical and experimental determination of flow structure and heat transfer effects of longitudinal vortices in a channel flow*", Int Journal of Heat & Mass Transfer, vol 39, pp 3441-3451, 1996
41. Cutler, A. D., Bradshaw, P., "*Strong vortex/boundary layer interactions. Part II. Vortices Low*", Experiments in Fluids 14, pp 393-401, 1993
42. Wu, W-S., Lilly, D. K., "*Helicity and Thermal Convection with Shear*", Journal of the Atmospheric Sciences, vol 49, pp 1800-1809, 1992
43. Moffatt, K. H., "*Helicity and singular structures in fluid dynamics*", PNAS, vol. 111, pp 3663-3670, 2014
44. Wallace, J. M., Balint, J., Ong, L., "*An experimental study of helicity density in turbulent flows*", Phys. Fluid A 4 (9), pp 2013-2026, 1992

Appendix A1

A1.1 Choosing the Right Turbulence Model

The figures below show the spanwise Stanton number at locations x = 0.98m and x = 1.88m for turbulence model Realizable k - ε, SST k - ω, and Reynolds stress model.

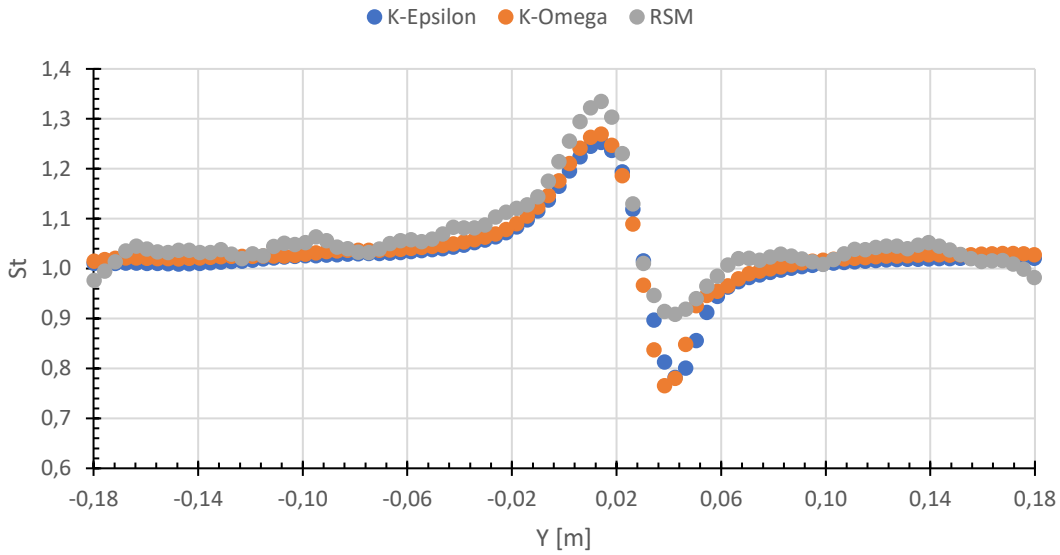

Figure 35. Different Turbulence Model Spanwise St at x = 0.98m

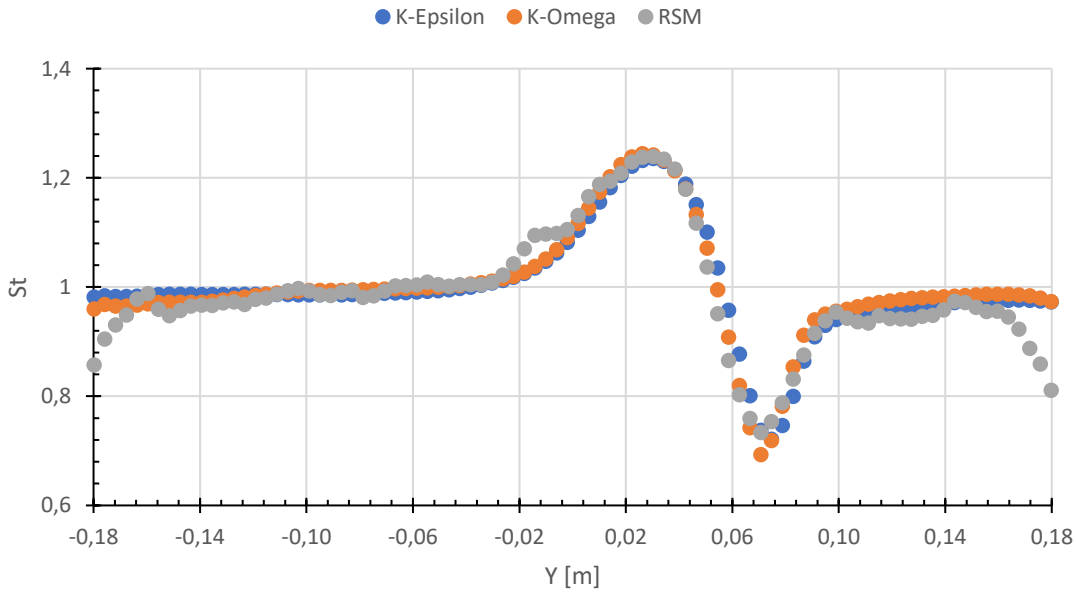

Figure 36. Different Turbulence Model Spanwise St at x = 1.88m

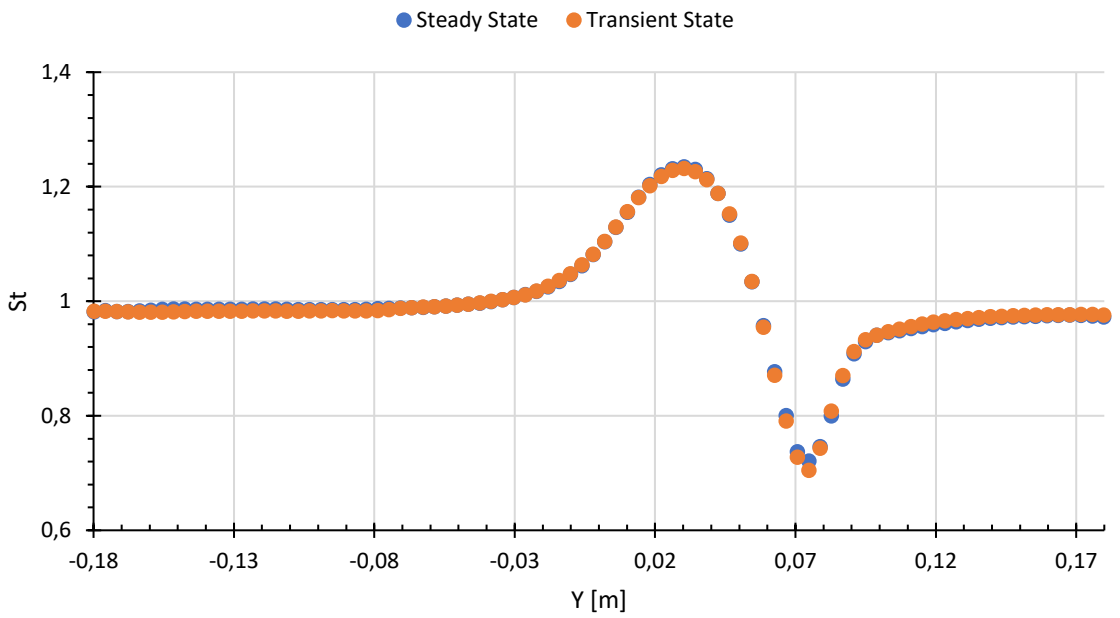

Figure 37. Steady-state vs Transient State Spanwise St at x = 0.98m

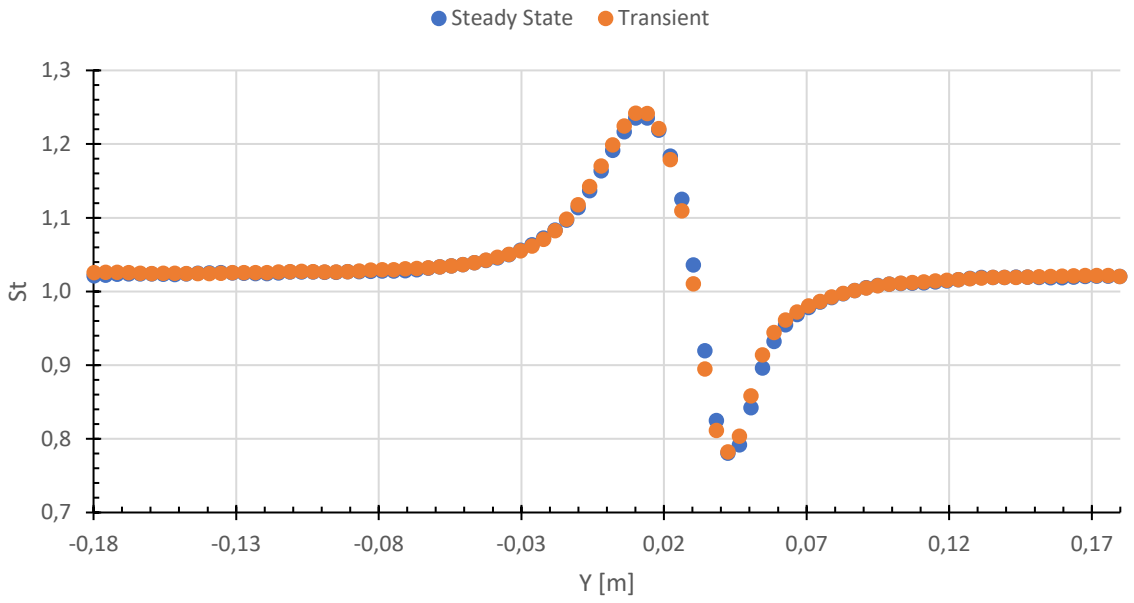

Figure 38. Steady-state vs Transient State Spanwise St at x = 1.88m

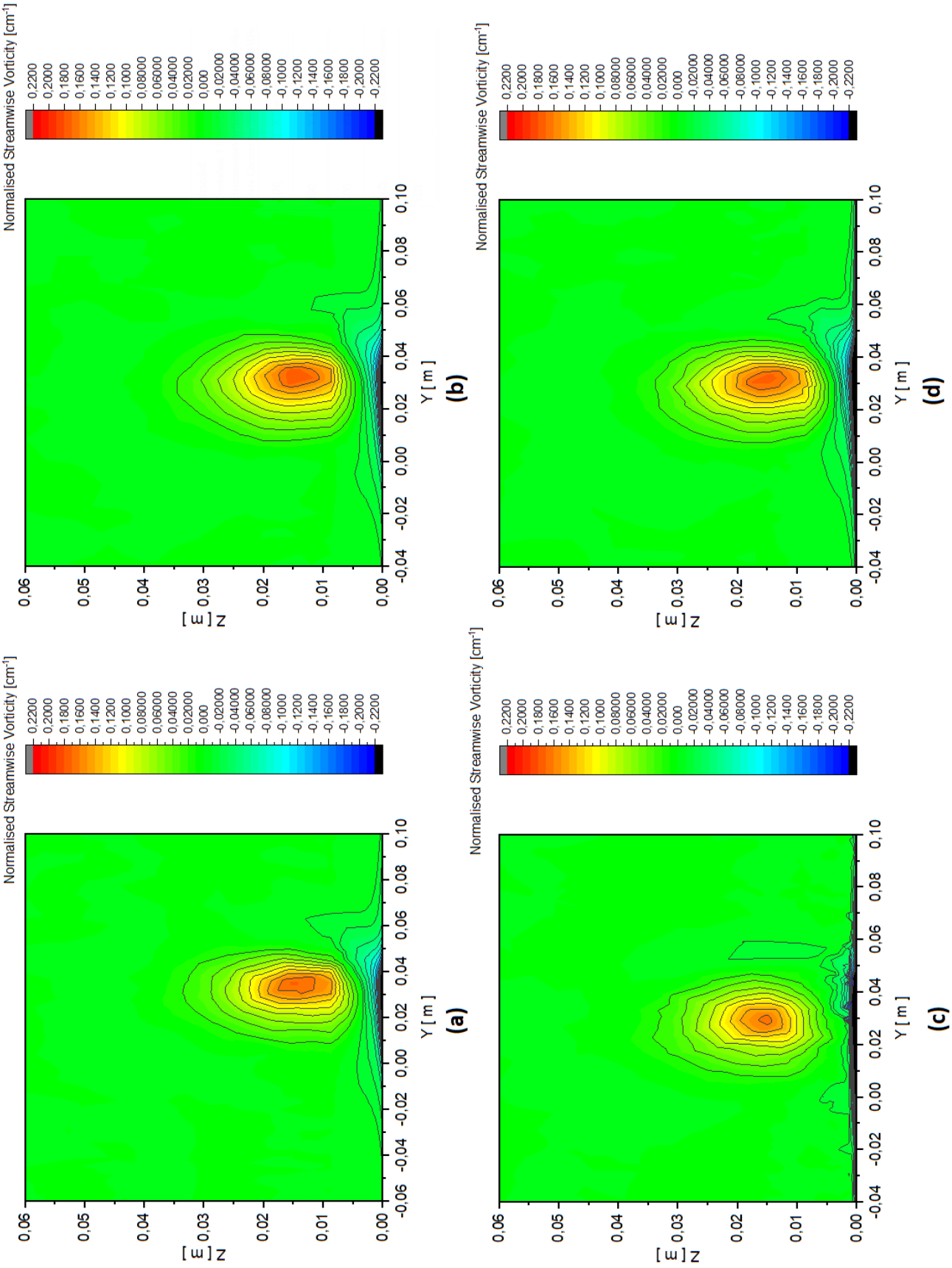

Figure 39. Vorticity Contours for (a) Realizable k - ε, (b) Transient k - ε, (c) RSM, and (d) SST k - ω

Appendix A2

A2.1 Imaging of Domain

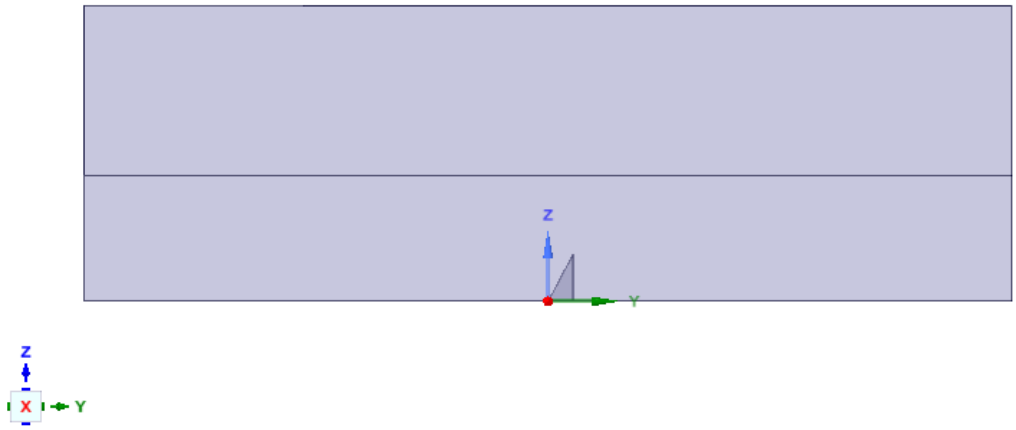

Figure 40. Front View of Domain Mesh A, B, C, and D



Figure 41. Top View of Mesh A, C, and D

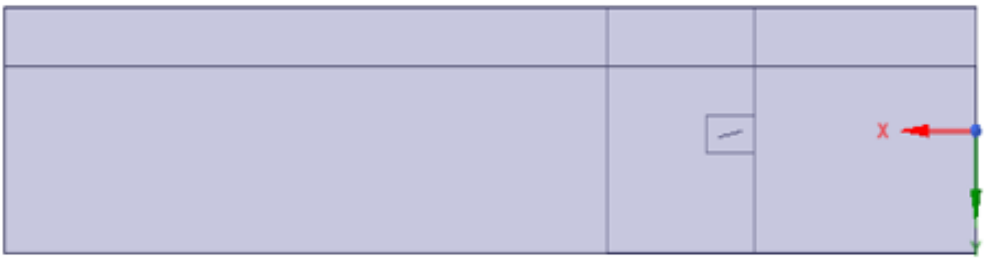

Figure 42. Top View of Domain Mesh B

A2.2 Imaging of Mesh

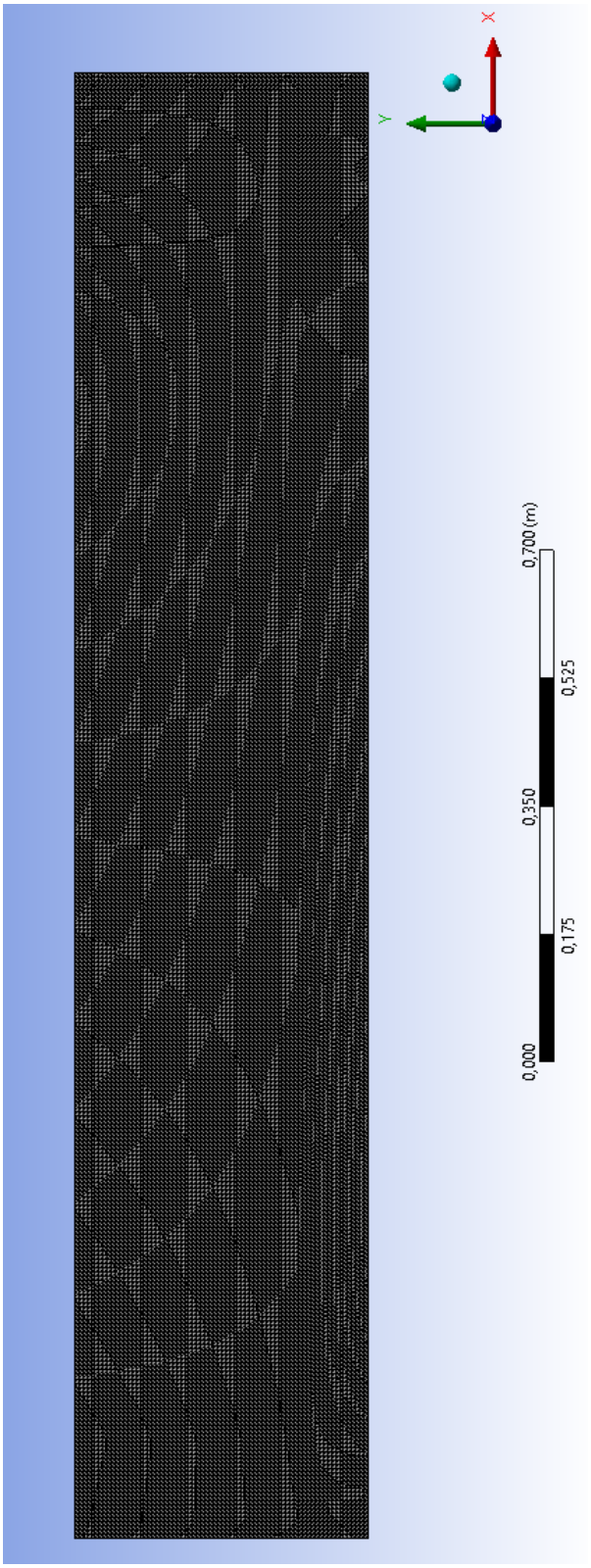

Figure 43. Top View of Mesh B

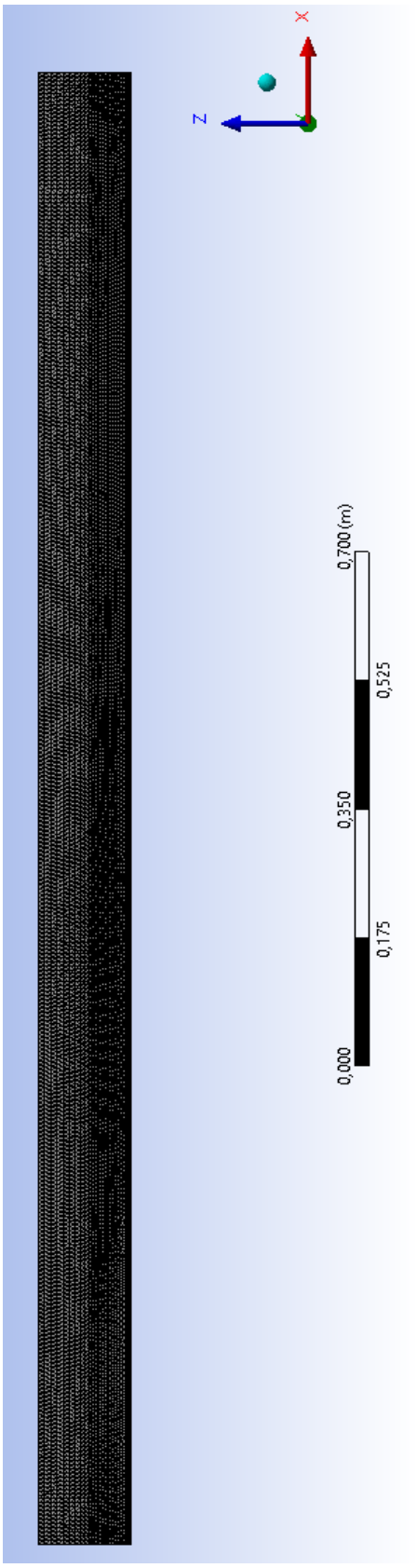

Figure 44. Side View of Mesh B

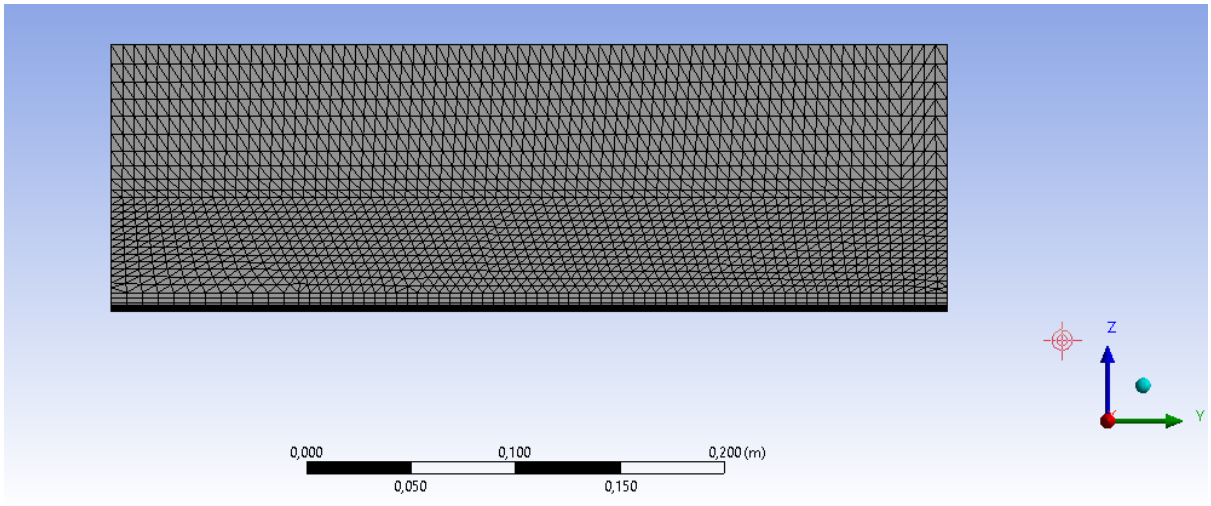

Figure 45. Front View of Mesh B

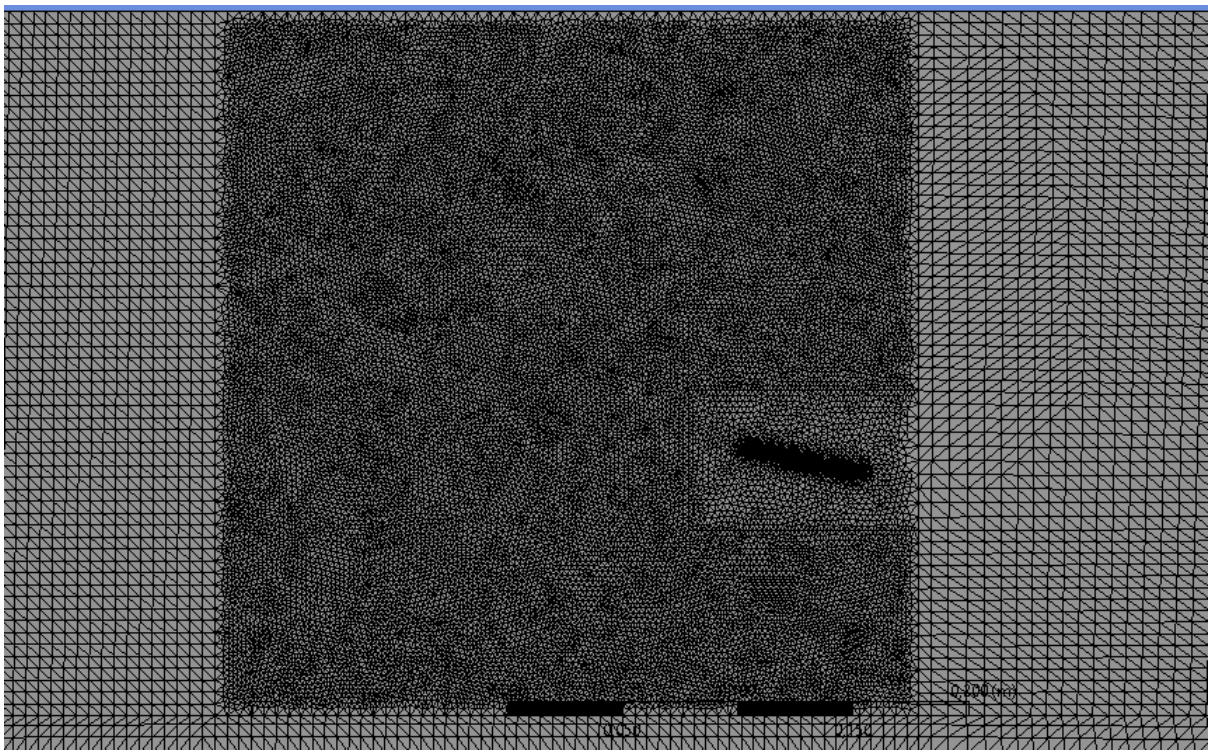

Figure 46. Closeup of Vortex Generator Surface of Mesh B

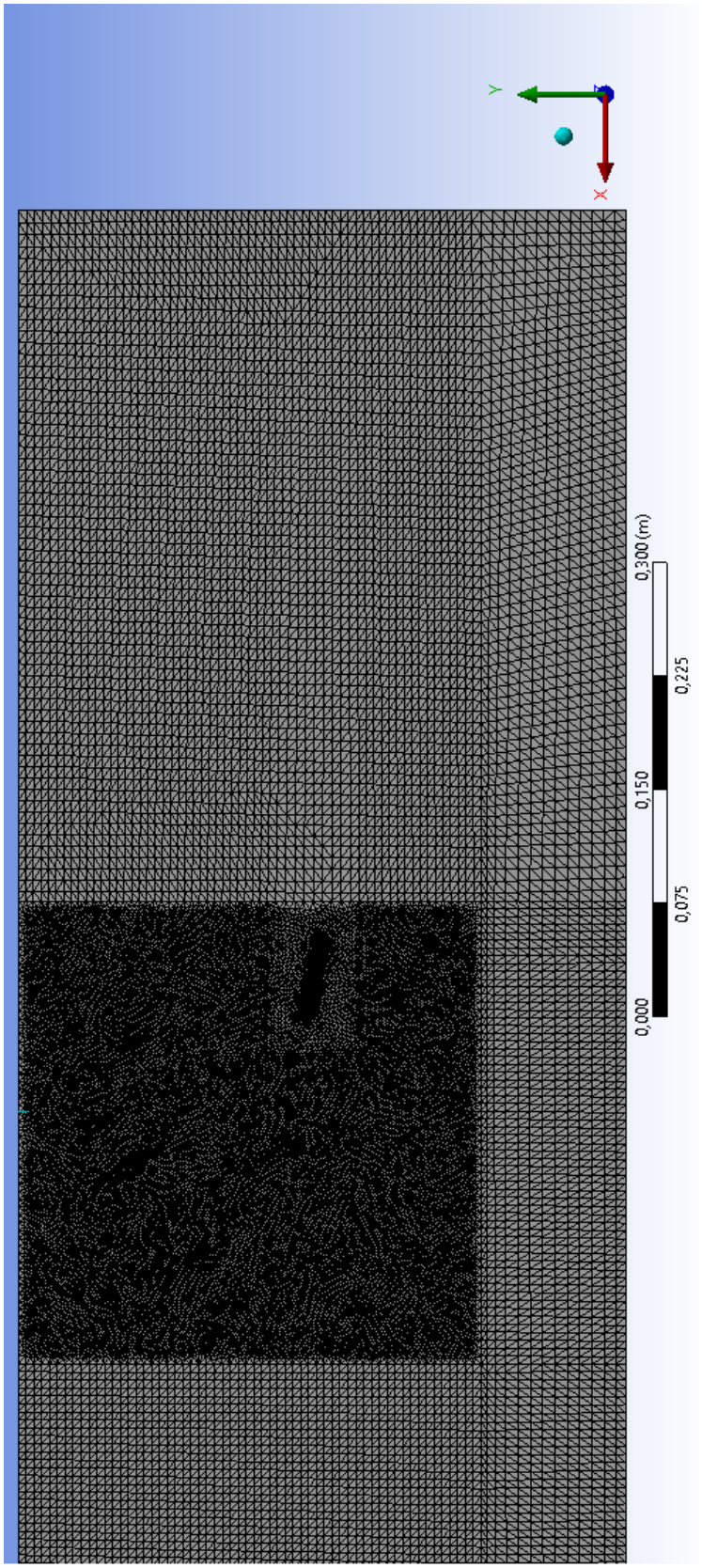

Figure 47. Closeup 2 of Vortex Generator of Mesh B

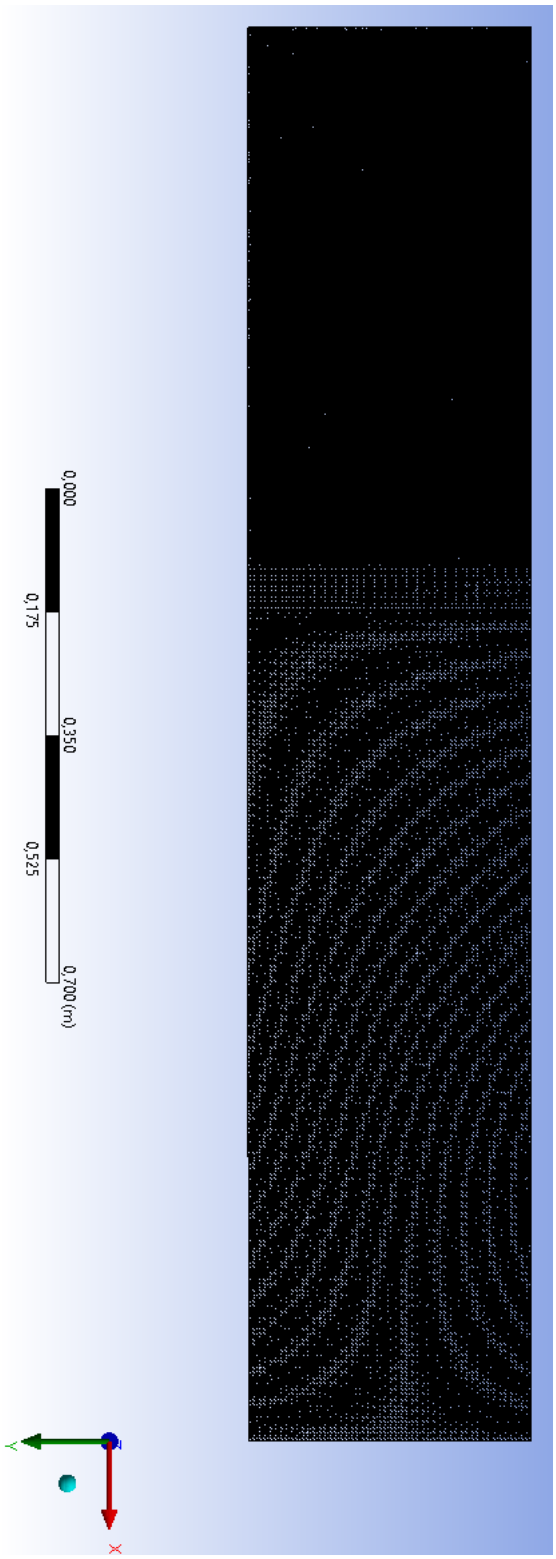

Figure 48. Bottom View of Grid Mesh D

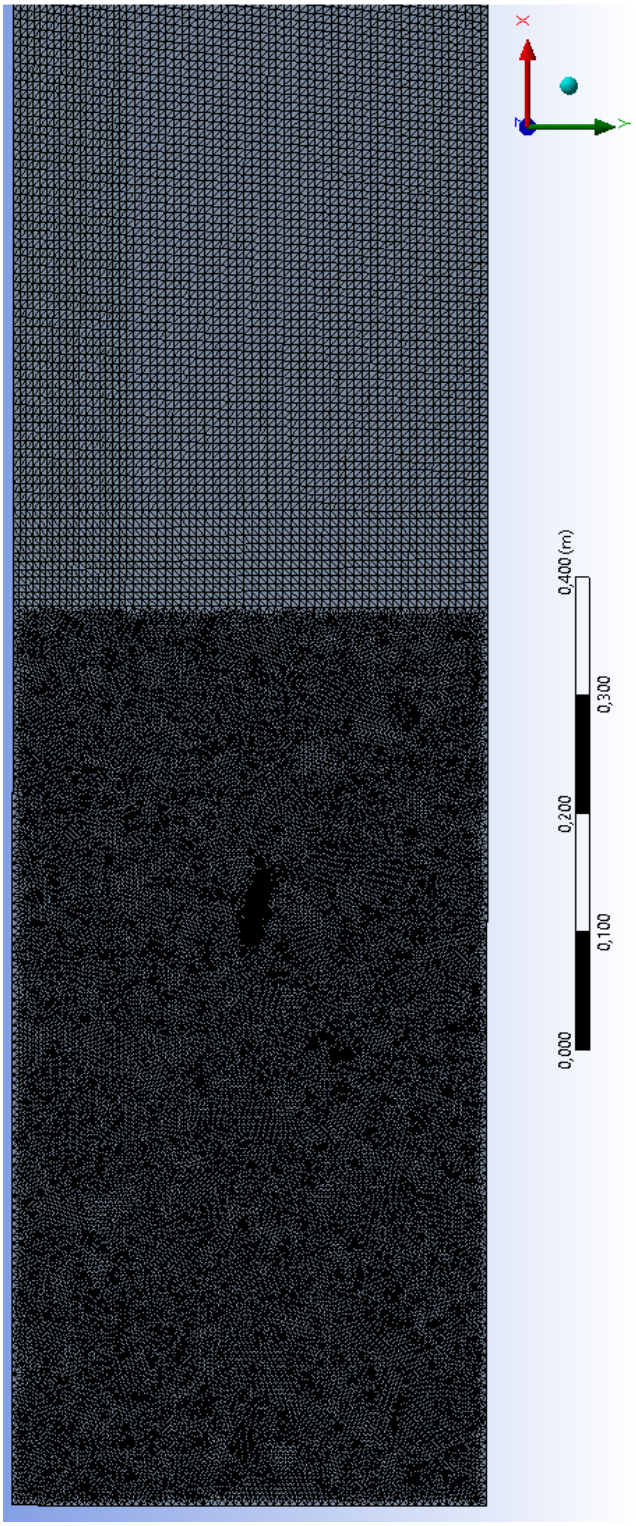

Figure 49. Close Up View of Grid Mesh D

Appendix A3

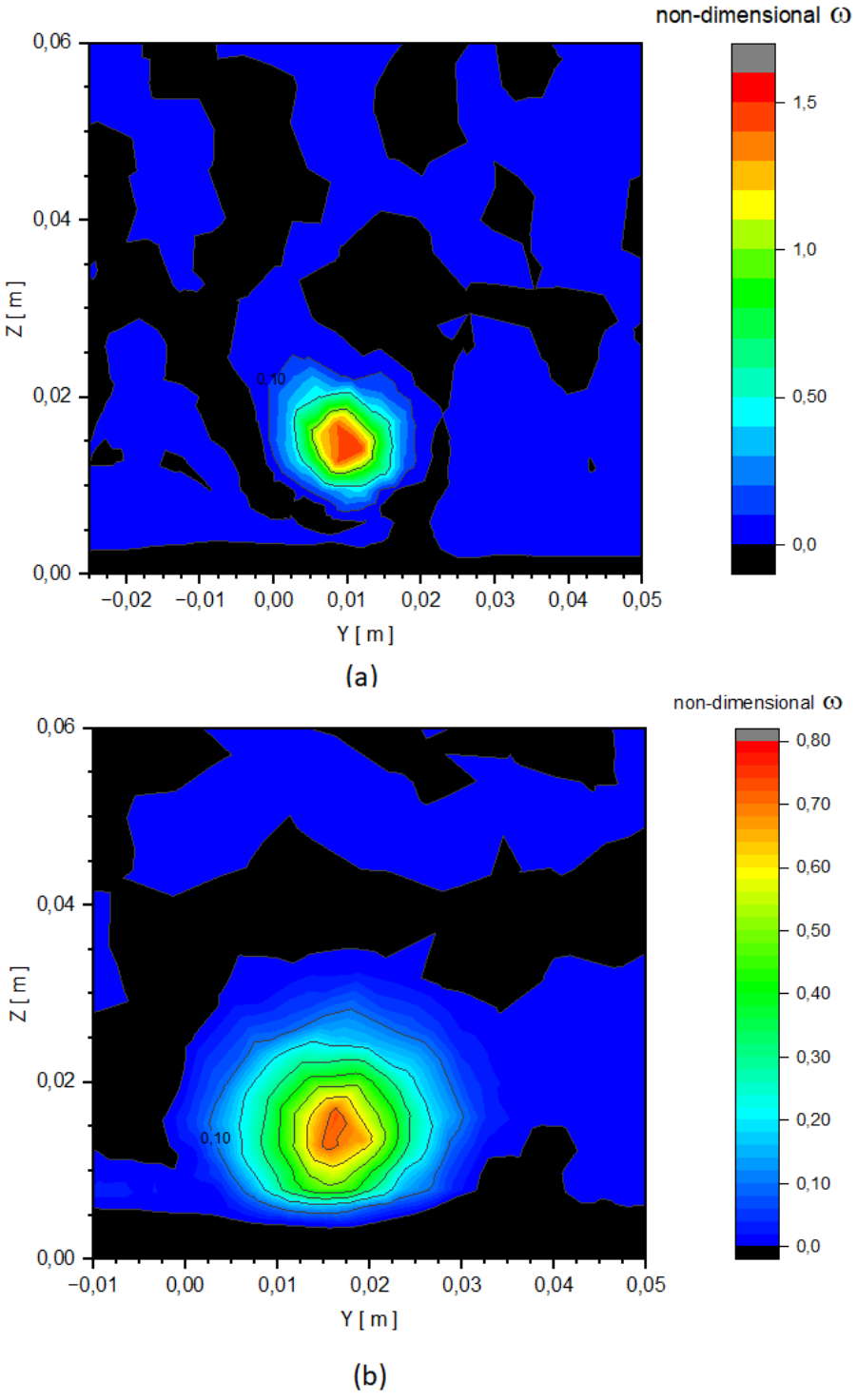

Figure 50. Nondimensional Vorticity at (a) x = 0.58m and (b) x = 0.75m